Implication of Urbanization on Meteorology and Air Quality

By

Jeff Chun-Fung LO

A Thesis Submitted to

The Hong Kong University of Science and Technology

in Partial Fulfillment of the Requirements for

the Degree of Doctor of Philosophy

in Atmospheric Environmental Science

January 2006, Hong Kong

Authorization

I hereby declare that I am the sole author of the thesis.

I authorize the Hong Kong University of Science and Technology to lend this thesis to other institutions or individuals for the purpose of scholarly research.

I further authorize the Hong Kong University of Science and Technology to reproduce the thesis by photocopying or by the other means, in total or in part, at the request of other institutions or individuals for the purpose of scholarly research.

_____

Jeff Chun-Fung LO

Implication of Urbanization on Meteorology and Air Quality

By

Jeff Chun-Fung LO

This is to certify that I have examined the above PhD thesis
and have found that it is complete and satisfactory in all respects,
and that any and all revisions required by
the thesis examination committee have been made.

_____

Prof. Alexis K.H. Lau, Supervisor

_____

Prof. Paul J. Harrison, Program Director

Program in the Atmospheric, Marine and Coastal Environment

The Hong Kong University of Science and Technology

January, 2006

Acknowledgements

I would like to express my deepest gratitude to my supervisor, Professor Alexis K. H. Lau, for his constant support and invaluable advice throughout the study. Discussions with him were fruitful. His broad knowledge and creative thinking was helpful for the generation of ideas. I learned a lot from him on how to do scientific research with quality.

I owe special thanks to Professor Jimmy C. H. Fung for his help, inspiring suggestions and engaging discussions throughout my study.

I would also like to thank Dr. Fei Chen for his supervision, spiritual support and encouragement during my half year research at NCAR in United States. I learned a lot from him on how to publish a scientific paper. His help during these years was important for the thesis completion.

I am sincerely grateful to the AMCE program at HKUST for their generous financial support during these years. I especially value the support of Professor Paul Harrison and Eliza Tang.

I also gratefully acknowledge helpful comments and discussion from all my colleagues, especially Dr. Jianping Huang and Zibing Yuan.

I also wish to thank many of the people who have worked in CCAR, especially, David Yeung and William Wong for their help and support.

Finally, I also thank the other members of my thesis committee Professor S.C. Kot and Professor C.N. Ng.

Table of Contents

Abstract

This dissertation focuses on investigating the feature and mechanism of local and regional scale atmospheric circulations and its associated pollution transport and trapping in the Pearl River Delta (PRD) region, which is a highly urbanized area with complex terrain and coastlines.

The first step of this research was to set up a localized fine-scale (1 km) land-surface/urban modeling system coupled with the mesoscale meteorological model MM5, to provide a more accurate and realistic prediction of meteorological condition over the region. After the model evaluations, a number of numerical experiments have been conducted in order to understand the impact of urbanization and its associated urban heat islands on meteorology over the PRD. The modeling system was then coupled with a particle trajectory model to demonstrate the unique land-sea breeze circulation features and the temporal evolution, and develop a conceptual model for the air pollution trapping phenomenon in the region. Further sensitivity experiments were used to illustrate the impact of urbanization and large-scale flows on the pollution processes.

After that, a new methodology was introduced to identify the contribution of primary and secondary pollutants from the emissions of local/regional area sources and power plants to Hong Kong. Several weighting factors were established to the air mass/pollutant trajectory calculations and used to evaluate the local and regional contribution of primary pollutants to Hong Kong pollution. The relationships between emission inventories, physical paths and chemical transformation rates of the pollutants, and observational measurements were formulated. The local and regional contributions of secondary pollutants were obtained by this conceptual module.

Finally, this study challenges the backward trajectory analysis, which is a well accepted analytical method in air quality research in Hong Kong. The result demonstrates large uncertainties in their behavior when comparing calculations using different resolution of wind fields, indicating that care must be taken on choosing the suitable resolution of wind fields when calculating trajectories for diagnostic studies.

Chapter 1 Introduction

1.1 Features of the Pearl River Delta Region

1.1.1 Social and Economic Features

Geographically, the Pearl River Delta (PRD) is situated in southern China. It is a delta region adjacent to the Pearl River (Zhujiang River) where it flows into the South China Sea. Due to its geographical advantage, PRD is the most economically dynamic region of mainland China since the launch of China's reform in 1979.

The term "Pearl River Delta Economic Zone" was set by Guangdong Province in 1994. This zone was officially defined as covering Guangzhou, Shenzhen, Zhuhai, Foshan, Jiangmen, Dongguan, Zhongshan, parts of Huizhou, and parts of Zhaoqing. The Greater PRD includes the Hong Kong Special Administrative Region (Hong Kong), and the Macau Special Administrative Region (Macau), and the Pearl River Delta Economic Zone. There are 11 cities with land area of 41,698 km^2 and a population over 50 million (Guangdong Statistical Yearbook, 2001). Figure 1-1 illustrates the map of the PRD. The demographics, land areas, and gross domestic product (GPD) of the cities in PRD are listed in Table 1-1.

1.1.2 Meteorological Features

The climate of PRD is sub-tropical, with a prolonged winter and summer, and transitional, short autumn and spring. During winter (November to March), synoptic-scale weather is influenced by Siberian high, the weather is generally cold and dry. Surface winds are generally weak to moderate northeasterly or strong northerly. Spring

(March to May) is a humid season, fog and drizzle can occasionally occur in PRD. The surface winds are predominated by moderate easterly. Heavy rain from Meiyu rainband may affect PRD in spring and early summer. During summer (May to September), the weather is hot and humid and sometimes with showers and thunderstorms. Most of the precipitation occurs in summer. Surface winds are generally moderate southwesterly or southeasterly. September is the month which PRD is most likely to be attacked by tropical cyclones. The duration of fall (September to November) is short with temperate weather, the surface winds become east or northeasterly.

Severe weather phenomena which can affect PRD include typhoon, strong winter cold front, and thunderstorms. Snow and tornadoes are rare in PRD.

In local-scale manner which this study focused, the local atmospheric circulations, such as land-sea breeze circulation (LSBC), mountain valley circulation (MVC) as well as urban heat island circulation (UHIC) can occur in PRD.

1.2 Urban Meteorology

In the past decades, both Hong Kong and the PRD have seen significant economic and population growth, this growth has been causing several environmental impacts in the region such as climate change and substantial air quality deterioration.

Meteorologically, urban and rural environments differ substantially in their micro-climate. These climatic differences are primary caused by the changing of the natural surface with human construction and the release of anthropogenic heat energy into the environment.

In a city, concrete, asphalt, and glass replace natural vegetation, and buildings are added to the natural landscape. These artificial surfaces generally have a lower albedo, greater heat conduction, and more heat storage than the natural surfaces. The geometry of the city buildings causes the absorption of incoming solar radiation and outgoing infrared radiation. In urban areas, large amounts of heat energy are added to the ambient environment through transportation, industrial activity, and the heating of air conditioning. Wind in urban areas is generally calmer than those in rural areas. This reduction in velocity is due to the frictional effects of the buildings. In addition, in rural areas, evaporation and transpiration from plants act to cool the land surface and lower part of the atmosphere. In urban areas, little plants and water is available for evaporative cooling.

These environmental characteristics cause urban areas tend to be warmer than the surrounding countryside. These differences in temperatures are more significant at night under stable atmospheric conditions. This phenomenon is called the urban heat island (UHI). The UHI is strongest at the city center where population densities are highest and industrial activity is at a maximum. The UHI effect has been observed since the 1960s (Woolum, 1964; Bornstein, 1968) and air temperature in a city can be 1-4°C higher than the surrounding countryside (WMO, 1984).

In the past 30 years, a number of climatological and observational studies have recognized that the UHI can have a significant influence on local-scale, mesoscale, and regional weather and climate. Early climatological studies (Khemani and Murty, 1973; Changnon et al., 1976; Braham, 1979) pointed out that UHI can increase cloudiness and precipitation in a city. Observations (Vukovich, 1971; Bornstein, 1975; Sawai, 1978)

also found that in a clam and weak synoptic forcing situation, urban heat island circulation (UHIC) can be generated between a city and surrounding region.

1.3 Climate Change in Hong Kong

According to the technical note from Hong Kong Observatory (HKO), because of the effect of urbanization, the temperature of Hong Kong has been warming up during the past 118 years (Leung et al., 2004). The rural areas of Hong Kong have been warming up at a rate of about 0.2°C per decade, regarding as the global warming trend. At the HKO Headquarters which is in the urban areas of Hong Kong, the corresponding rise was about 0.6°C per decade, demonstrating that not only global warming, but also the local warming by the UHI, is changing the climate in Hong Kong. Figure 1-2 demonstrates the increasing trend of annual mean temperature in Hong Kong. The trend of annual mean daily maximum and minimum temperatures is displayed in Figure 1-3.

The urban development in Hong Kong also related to the reduction of visibility, increase in cloud amount and decrease of solar radiation in Hong Kong. The number of heavy rain days has also increased during the period 1947 to 2002 (Leung et al., 2004)

1.4 Air Quality in Hong Kong and PRD

The environmental impacts accompanied by the significant economic and population growth not only reflected by climate change, but also the deteriorated air quality within the entire PRD region. According to the Hong Kong Environment Protection Department (HKEPD), street-level pollution and smog are the two major pollution problems in Hong Kong. The poor air quality in street level is primarily caused by the high volume of traffics locally. While the regional smog problems, such as the

poor visibility, high levels of respirable suspended particulates (RSP) and ozone (O_3) episodes, are not only caused by the emissions from motor vehicles, but also from the industry and power plants both within Hong Kong and in the PRD (HKEPD, 2003).

Under a series of stringent air quality control implemented by the Hong Kong government, such as cutting sulphur content of industrial fuels and ameliorating motor vehicle fuel quality, emissions from local industry and automobile have been reducing in the recent decade. According to HKEPD, emissions of sulfur dioxide (SO_2), particulate matters (PM), and nitrogen oxide (NO_X) in 2003 dropped by 54%, 50% and 41% respectively compared with their levels in 1993 (see Figure 1-4). However, the ozone level in Hong Kong (see Figure 1-5), as evidenced by the duration of poor visibility and frequency of occurrence of ozone episodes, has been in an increasing trend in the recent years (HKEPD, 2003). The percentage of days with poor visibility (visibility less than 8 km with relative humidity recorded less than 80%) in 2003 (15%), as shown in Figure 1-6, was 2.5 times the 1993 value (6%). The air pollution observational measurements in the PRD region outside Hong Kong are limited. Instead, the duration of poor visibility in Shenzhen and Guangzhou, the other two major cities in PRD, increased 8 times and 3 times in the last decade respectively (CH2M, 2002). Since ozone and smog problem is a regional air pollution issue, the rising trend generally reflects deterioration in air quality on a regional scale over the past decade.

1.5 Land-Sea Breeze Circulation

In coastal regions, one of the most prominent atmospheric phenomena is the land-sea breeze circulation (LSBC) which is induced by the unequal heating of land and sea. The existence of LSBC has been recognized for centuries and its fundamental structure and theory has been studied extensively for past few decades (e.g. Venkatram, 1977; Athens, 1978; Singal et al., 1986; Weil et al., 1988; Gruning and Batchvarova, 1990).

On a sunny day, the sun heats the ground rapidly. The air near the ground is strongly heated and expands. Because the hot air is less dense than the cool air offshore, it weighs less and exerts less pressure. Thus, low pressure is formed over the coast. As the heat capacity of sea is higher than land, the air near the sea surface is not heated up as fast as that over the neighboring land. Pressure remains higher over the sea. Thus, there is a pressure gradient from sea to land and a wind is set in motion causes a sea breeze.

At night, the ground cools more rapidly than the neighboring sea. A cool air layer of higher pressure develops. Now the pressure gradient is from land to sea, setting up a land breeze.

In the past, considerable attention has been devoted to studying the effect of LSBC on air pollution. The structure and characteristics of LSBC have been known to be playing an important role on air pollution dispersion. Keen and Lyons (1978) showed that air pollutants are transported inland along with the sea breeze front in daytime. Ueda et al. (1988) and Lu et al. (1994) also pointed out the passage of sea breeze caused high pollutants concentration on the ground. Martilli (2002) carried out an idealized two-

dimensional numerical simulation to show the presence of cities enhances the sea breeze and strongly modifies the pollutant dispersion.

Many urban areas in the PRD are located near the coastal zone, with a clam or weak synoptic forcing which is favorable for serve air pollution episodes, LSBC as well as urban heat island circulation (UHI) can occur at the PRD. To mitigate the rapidly deteriorating air quality, an understanding of the local and regional circulation, including the complex interactions between the local LSBC and the urban environment in the PRD, is critical. While researchers suspect the LSBC cell has a significant influence on air flow pattern and may affect the air quality in this region, the physical mechanism has never been fully understood or quantified.

1.6 Objectives and Organization of this Research

This research focuses on investigating the characteristics of local atmospheric circulations, and their influence on the pollutant transport in PRD. The objectives of this research were:

I. To improve the performance of the present numerical meteorological model MM5 in order to provide more realistic meteorological conditions in the PRD.

II. To investigate the impact of rapid urbanization on the local scale meteorological conditions.

III. To explore the mechanism of pollutant trapping and the accumulation problem in the urban and coastal areas.

IV. To investigate the effect of urbanization on the pollutant transport and accumulation.

V. To introduce a better method for identification of source regions of air pollutants

In Chapter 2 and Chapter 3, the numerical meteorological model, and the land surface model used in this study are briefly described. Chapters 4 to 7 provide a detailed account of the results obtained. Each chapter could be regarded as an individual paper. Chapter 4 focuses on the meteorological model enhancement and model evaluation. The impacts of urbanization on meteorological conditions were also discussed. Chapter 5 investigates the features of land-sea breeze circulation over the PRD. The pollutant transport characteristics and the urbanization impact are explored. Chapter 6 introduces a new method for identification of source regions of air pollutants. Chapter 7 challenges a well accepted analytical method in air quality research in Hong Kong.

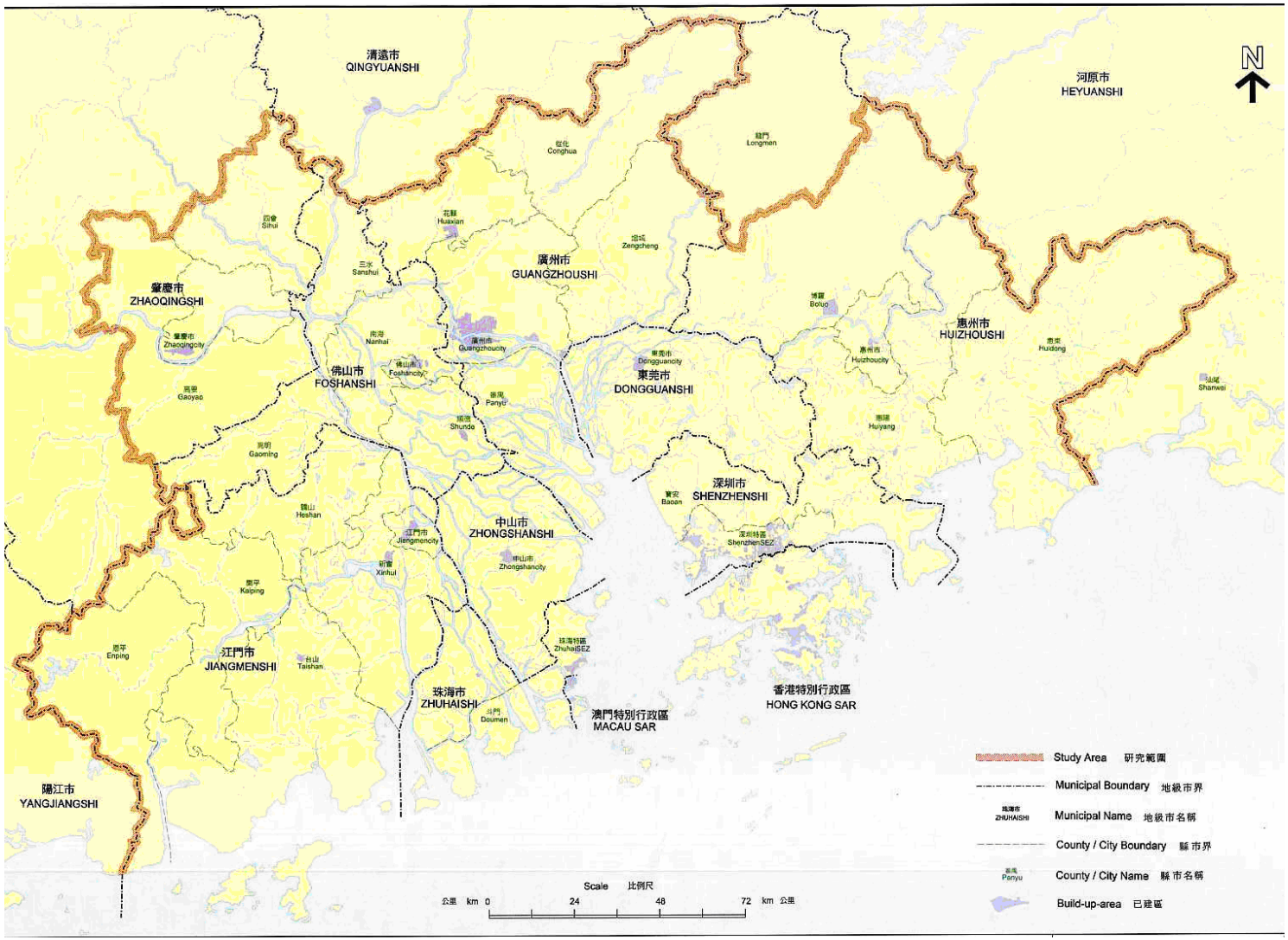

Source: HKPD, 2003

Figure 1-1: Map of the Pearl River Delta region.

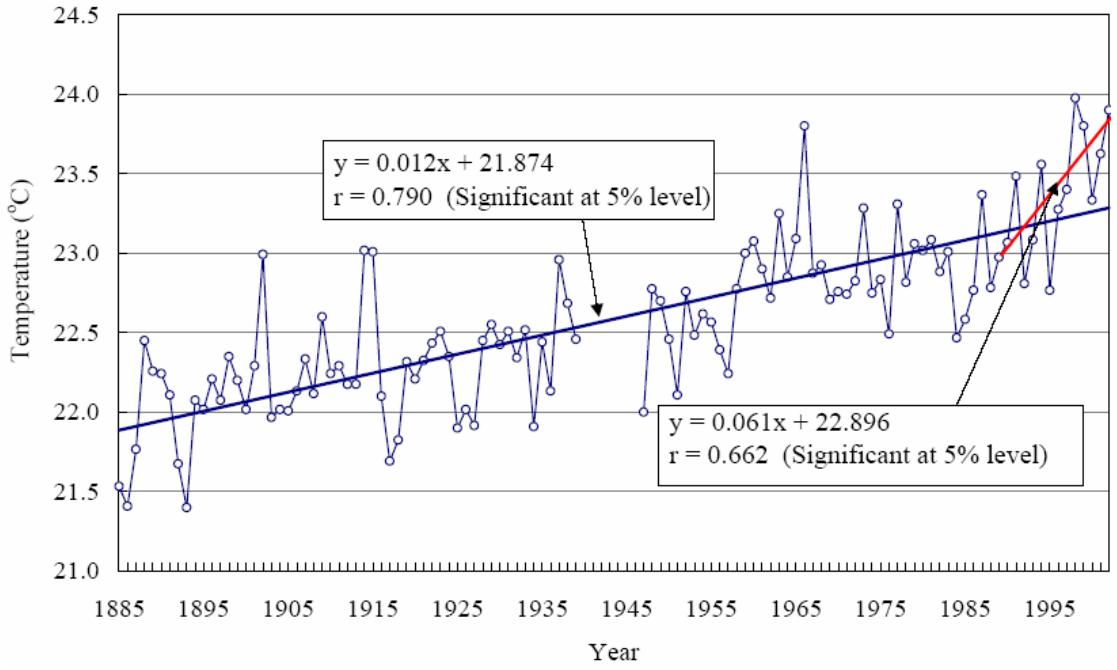

Source: Hong Kong Observatory Technical Note No. 107

Figure 1-2: Annual mean temperature recorded at HKO Headquarters.

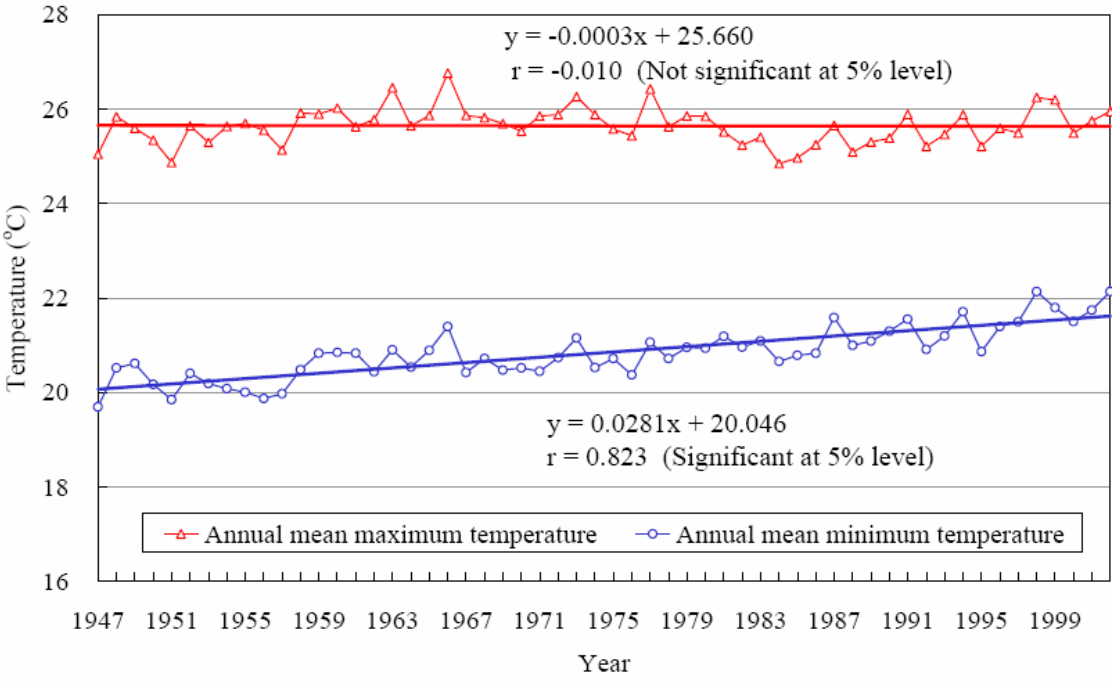

Source: Hong Kong Observatory Technical Note No. 107

Figure 1-3: Annual mean daily maximum and minimum temperatures recorded at HKO Headquarters.

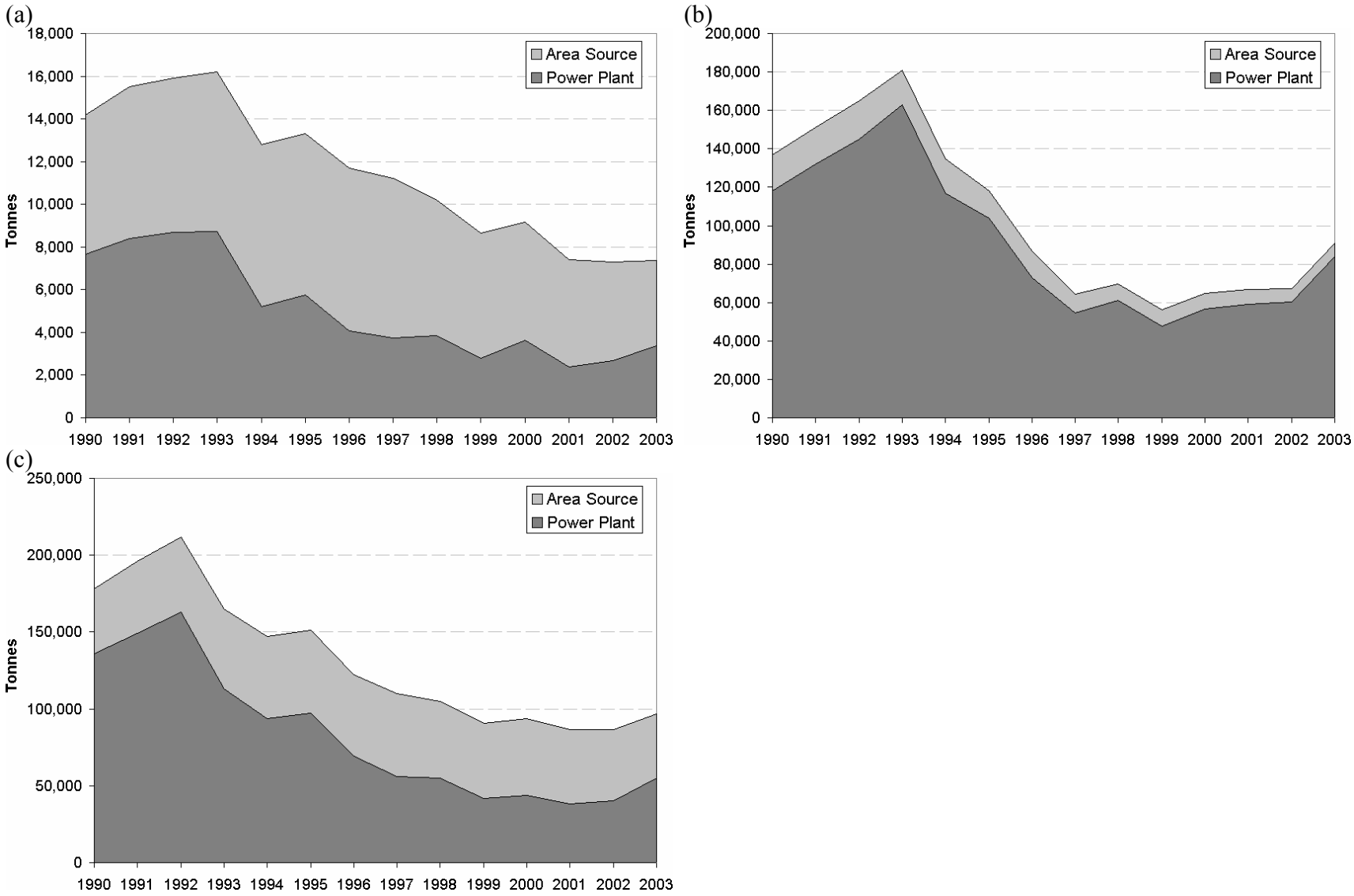

Figure 1-4: Long term trends of air pollution emission in Hong Kong. (a) PM, (b) SO_2 and (c) NO_X.

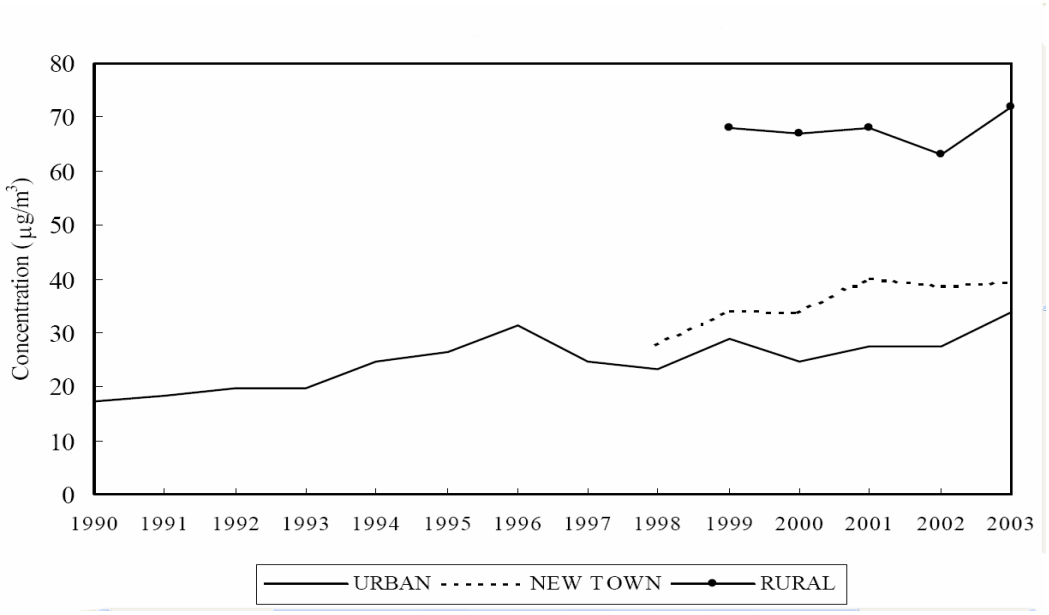

Source: HKEPD annual report, 2003

Figure 1-5: The long-term trend of concentration of O_3 in Hong Kong.

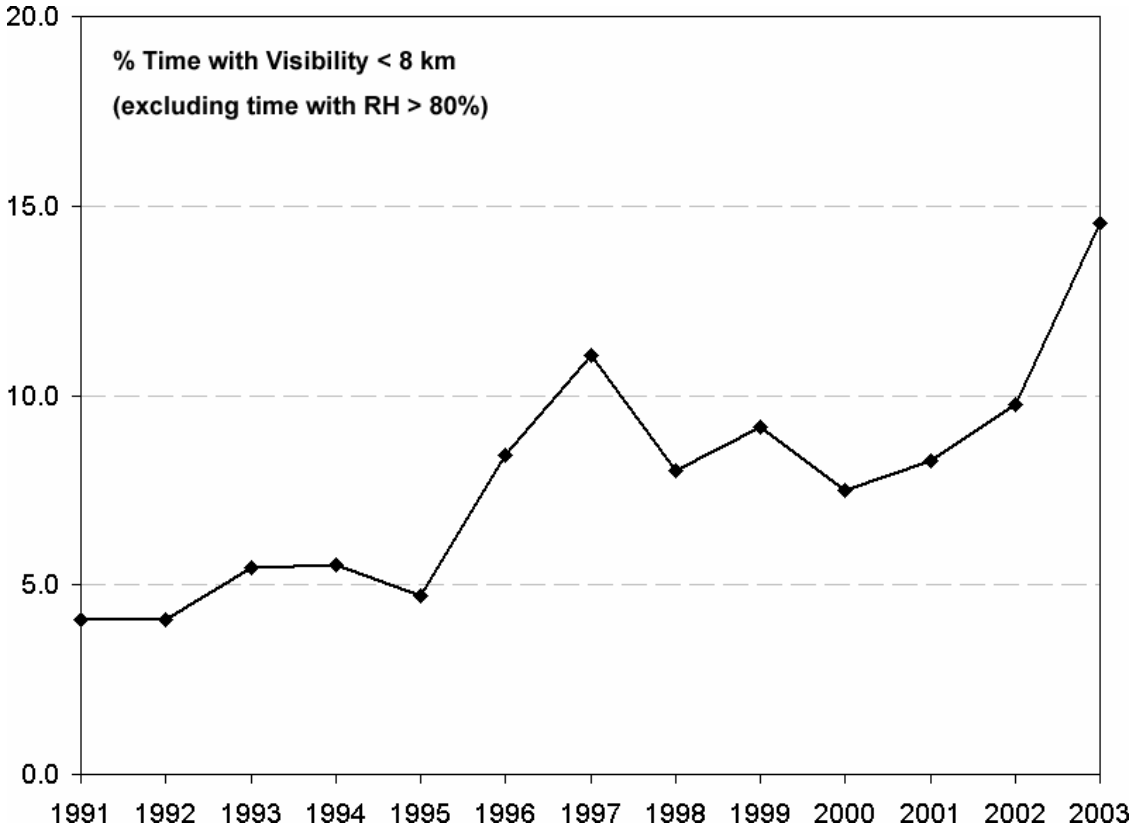

Figure 1-6: Trends of visibility impairment in Hong Kong.

Table 1-1: Population, land area, and GDP of the PRD region.

Cities	**Population (million)**	**Land Area (km^2)**	**GDP (US$ bn)**
Hong Kong	6.8	1100	161.9
Macau	0.4	25.8	6.7
Guangzhou	9.9	7434	36.3
Shenzhen	7.0	1949	27.3
Zhuhai	1.2	705	4.9
Dongguan	6.5	2465	8.1
Foshan	5.3	3914	14.2
Jiangmen	4.0	9541	8.0
Zhongshan	2.4	1800	5.0
Huizhou	3.2	11158	6.3
Zhaoqing	3.4	14856	5.4

Source: Guangdong statistics Year book 2001, 2003; HKSAR Census & Statistics Department

Chapter 2 Description of the Meteorological Model MM5

The meteorological model used in this study is the Pennsylvania State University/National Center for Atmospheric Research (NCAR) Fifth-Generation Mesoscale Model (MM5) version 3.6.3. It is a limited-area, non-hydrostatic, primitive equation model with terrain-following sigma-coordinate (Dudhia, 1993; Grell et al., 1994). It is a widely used community model designed to predict mesoscale and regional-scale atmospheric circulations. Previous studies also proved that MM5 has good performances in numerical weather prediction, air quality studies and hydrological studies over the world (Warner et al., 1991; Mass and Kuo, 1998; Vaughan et al., 2004). This chapter contains the main concepts of the MM5 modeling system.

2.1 Model Horizontal and Vertical Grid

The model vertical coordinate is terrain-following sigma-coordinate (see Figure 2-1) which means that the lower levels follow the terrain while the upper level is flat. Intermediate levels gradually flatten as the pressure decreases toward the model top pressure. The model vertical level is given by:

$$\sigma = (p_0 - p_t)/(p_{s0} - p_t) \tag{2-1}$$

where p_0 is the reference-state pressure, p_t is a specified constant top pressure, and p_{s0} is the reference-state surface pressure.

It can be seen from Equation (2-1) and Figure 2-1 that σ is zero at the model top and one at the surface, and each model level is defined by a value of σ. The model vertical resolution is defined by a list of values between zero and one.

The horizontal grid has an Arakawa-Lamb B-staggering of the velocity variables with respect to the scalars. This is shown in Figure 2-2 that the scalars (T, q etc.) are defined at the center of the grid, while the eastward (u) and northward (v) velocity components are collocated at the corners. The center points of the grid will be referred to as cross points and the corner points are dot points. Hence horizontal velocity is defined at dot points.

All the above variables are defined in the middle of each model vertical layer, referred to as half-σ levels and represented by the dashed lines in Figure 2-2. Vertical velocity (w) is carried at the full levels.

2.2 Initial and Lateral Boundary Conditions

To run any regional numerical weather prediction (NWP) model, it requires initial and lateral boundary conditions. In MM5, all four boundaries have specified horizontal winds, temperature, pressure, and moisture fields. Therefore, boundary values have to be set for these fields before running the simulation.

The boundary values come from analyses at the future times, or previous coarser-mesh simulations, or from another model's forecast. For real-time forecasts the lateral boundaries will ultimately depend on a global-model forecast. In studies of past cases the analyses providing the boundary conditions may be enhanced by observation analysis in the same way as initial conditions are.

There are two ways of doing nesting in MM5. These are one-way nesting and two-way nesting. One-way nesting differs from two-way nesting in having no feedback and coarser temporal resolution at the boundaries. For one-way nesting, the model uses the discrete-time analyses by linearly interpolating them in time to the model time. The analyses completely specify the behavior of the outer row and column of the model. In the next four rows and columns in from the boundary, the model is nudged towards the analyses. The strength of this nudging decreases linearly away from the boundaries.

Two-way nest boundaries are similar but are updated every coarse-mesh time-step and have no relation zone.

2.3 Governing Equations of MM5

The transformation from the Cartesian coordinate system into the sigma coordinate system, i.e., $(x, y, z) \rightarrow (x, y, \sigma)$ is given by

$$\left(\frac{\partial}{\partial x}\right)_z \rightarrow \left(\frac{\partial}{\partial x}\right)_\sigma - \left(\frac{\partial}{\partial x}\right)_\sigma \frac{\partial}{\partial z} \tag{2-2}$$

while

$$\delta z = \frac{\delta p_0}{\rho_0 g} = \frac{(p^* \delta\sigma + \sigma \delta p^*)}{\rho_0 g} \tag{2-3}$$

$$\left(\frac{\partial}{\partial x}\right)_z \rightarrow \left(\frac{\partial}{\partial x}\right)_\sigma - \frac{\sigma}{p^*}\frac{\partial p^*}{\partial x}\frac{\partial}{\partial \sigma} \tag{2-4}$$

In terms of terrain following coordinates (x, y, σ), these are the equations for the nonhydrostatic model's basic variables.

Pressure

$$\frac{\partial p'}{\partial t} - \rho_0 g w + \gamma p \nabla \cdot V = -V.\nabla p' + \frac{\gamma p}{T}\left(\frac{\dot{Q}}{c_p} + \frac{T_0}{\theta_0} D_\theta\right) \tag{2-5}$$

Momentum (x-component)

$$\frac{\partial u}{\partial t} + \frac{m}{\rho}\left(\frac{\partial p'}{\partial x} - \frac{\sigma}{p*}\frac{\partial p*}{\partial x}\frac{\partial p'}{\partial \sigma}\right) = -V \cdot \nabla u + v\left(f + u\frac{\partial m}{\partial y} - v\frac{\partial m}{\partial x}\right) - ew\cos\alpha - \frac{uw}{r_{earth}} + D_u \tag{2-6}$$

Momentum (y-component)

$$\frac{\partial u}{\partial t} + \frac{m}{\rho}\left(\frac{\partial p'}{\partial x} - \frac{\sigma}{p*}\frac{\partial p*}{\partial x}\frac{\partial p'}{\partial \sigma}\right) = -V \cdot \nabla u + v\left(f + u\frac{\partial m}{\partial y} - v\frac{\partial m}{\partial x}\right) - ew\cos\alpha - \frac{uw}{r_{earth}} + D_u \tag{2-7}$$

Momentum (z-component)

$$\frac{\partial w}{\partial t} + \frac{\rho_0}{\rho}\frac{g}{p*}\frac{\partial p'}{\partial \sigma} + \frac{g p'}{\gamma p} = -V \cdot \nabla w + g\frac{p_0}{p}\frac{T'}{T_0} - g\frac{R_d}{c_p}\frac{p'}{p} + e(u\cos\alpha - v\sin\alpha) + \frac{u^2 + v^2}{r_{earth}} + D_w \tag{2-8}$$

Thermodynamics

$$\frac{\partial T}{\partial t} = -V \cdot \nabla T + \frac{1}{\rho c_p}\left(\frac{\partial p'}{\partial t} + V \cdot \nabla p' - \rho_0 g w\right) + \frac{\dot{Q}}{c_p} + \frac{T_0}{\theta_0} D_\theta \tag{2-9}$$

where subscript 0 denotes the reference state, prime denotes deviation from the reference state, and D_ϕ represents the subgrid scale term. Variable used in the equations include ρ (air density), θ (potential temperature), $\dot{Q}$ (adiabatic process), g (acceleration due to gravity), f (Coriolis force), R_d (gas constant of dry dir), γ (ratio of heat capacity for air at constant pressure to that at constant volume). $e = 2\omega\cos\lambda$, $\alpha = \phi - \phi_c$ where λ is

latitude, ϕ is longitude, ϕ_c is central longitude. The $u\frac{\partial m}{\partial y}$, $v\frac{\partial m}{\partial x}$ and r_{earth} terms represent curvature effects, and m is a map-scale factor.

In addition, the advection terms can be expanded as

$$V \cdot \nabla A = mu\frac{\partial A}{\partial m} + mv\frac{\partial A}{\partial y} + \dot{\sigma}\frac{\partial A}{\partial \sigma} \tag{2-10}$$

where

$$\dot{\sigma} = -\frac{\rho_0 g}{p^*}w - \frac{m\sigma}{p^*}\frac{\partial p^*}{\partial x}u - \frac{m\sigma}{p^*}\frac{\partial p^*}{\partial y}v \tag{2-11}$$

and the divergence term is given by

$$\nabla \cdot V = m^2\frac{\partial}{\partial x}\left(\frac{u}{m}\right) - \frac{m\sigma}{p^*}\frac{\partial p^*}{\partial x}\frac{\partial u}{\partial \sigma} + m^2\frac{\partial}{\partial y}\left(\frac{v}{m}\right) - \frac{m\sigma}{p^*}\frac{\partial p^*}{\partial y}\frac{\partial v}{\partial \sigma} - \frac{\rho_0 g}{p^*}\frac{\partial w}{\partial \sigma} \tag{2-12}$$

The set of partial differential equations as represented by Equations (2.4 – 2.8) is solved numerically with finite difference approximations. For the spatial finite differencing scheme, second-order centered finite difference represents the gradients except for the precipitation fall term that uses the first-order upstream for positive definiteness. For temporal finite differencing, a second-order leapfrog time-step scheme is used for these equations but some terms handled used a time-splitting scheme. More details are given in Grell et al., (1994).

Various physical processes are treated as explicitly or implicitly in MM5. Each physical process can be parameterized by different schemes. The physical processes considered in MM5 as parameterization mainly include cumulus process, planetary

boundary layer (PBL), moisture process, atmospheric radiation, land surface process and so on.

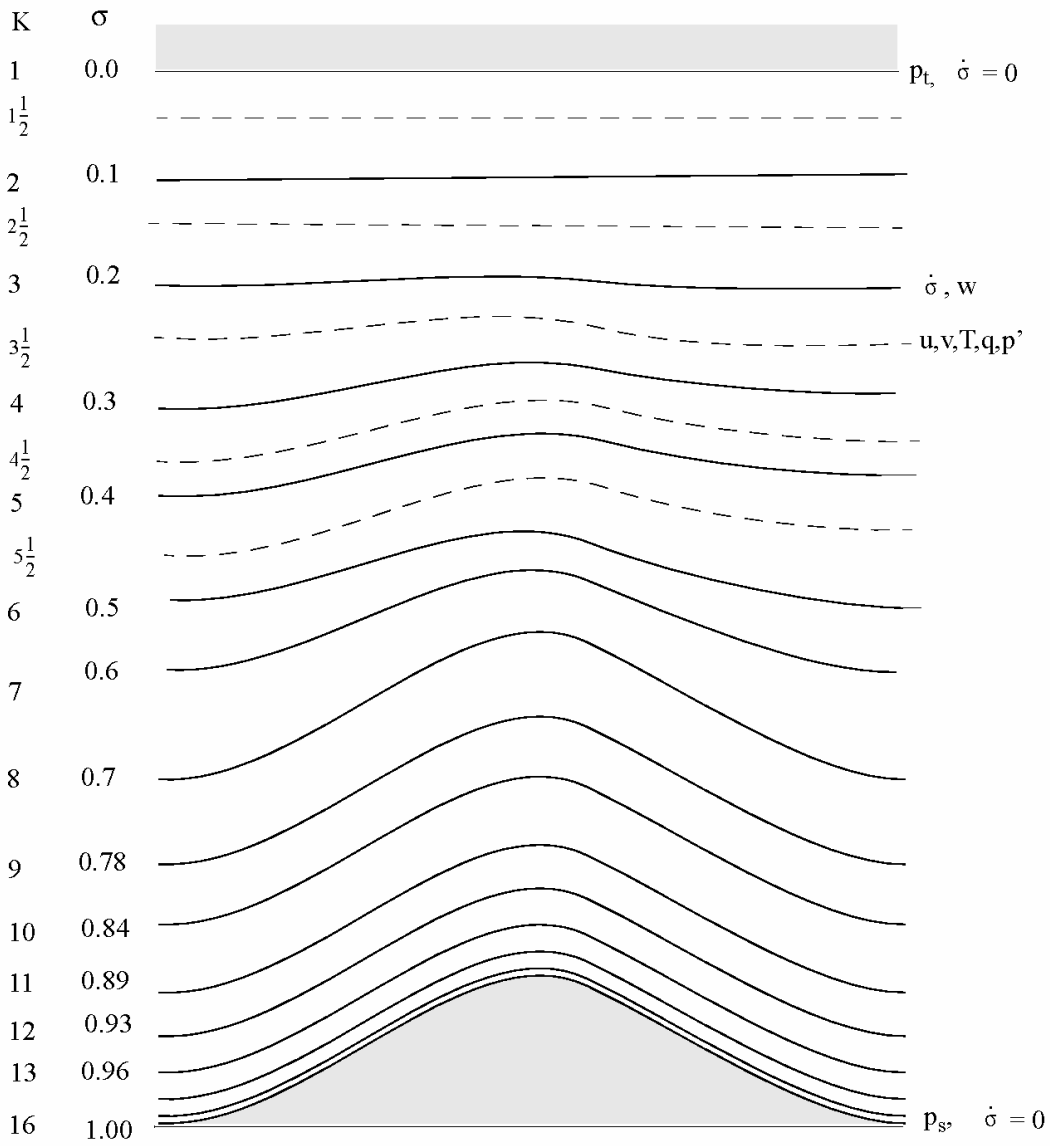

Figure 2-1: Schematic representation of the vertical structure of the model. Dashed lines denote half-sigma levels, solid lines denote full-sigma levels.

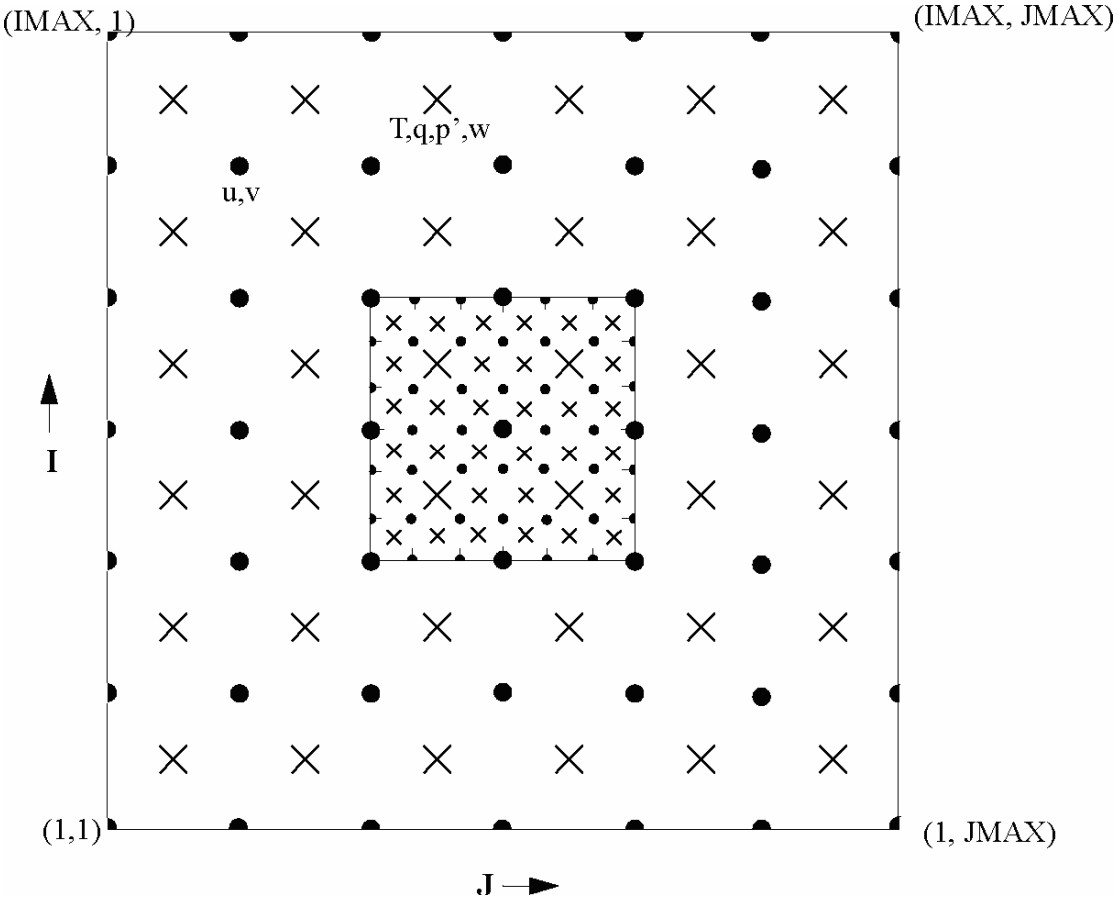

Figure 2-2: Schematic representation showing the horizontal Arakawa B-grid staggering of the dot (•) and cross (×) grid points.

Chapter 3 Description of the Land Surface Model

The land surface model (LSM) used in this study was originally developed at Oregon State University (OSU) in the middle 1980s (Mahrt and Pan, 1984; Pan and Mahrt, 1987). During the next two decades, a number of enhancements have been made in the original OSU LSM by collaborations of various organizations. The OSU LSM has now been renamed as Noah LSM in recognition of the partnership among **N**ational Centers for Environmental Prediction (NCEP), the **O**regon State University, the U.S. **A**ir Force and the Office of **H**ydrological Development (OHD) of the National Weather Service (NWS). This LSM is a well studied model in both uncoupled and coupled mode over a wide range of space scales and timescales.

This chapter contains a brief overview of the Noah LSM, this identifier abbreviates simply as 'LSM' herein, followed by a more detailed description of the model thermodynamics and model hydrology.

3.1 Overview

The LSM is based on coupling of the diurnally-dependent Penman potential evaporation approach of Mahrt and Ek (1984), the multi-layer soil model of Mahrt and Pan (1984) and the primitive canopy model of Pan and Mahrt (1987). Chen et al. (1996) has extended the improvements to include the modestly complex canopy resistance approach of Noihan and Planton (1989) and Jacquemin and Noihan (1990). A schematic description of the LSM is shown in Figure 3-1.

The LSM has one canopy layer and four soil layers from ground surface to the bottom with thickness of 0.1, 0.3, 0.6 and 1.0 m, respectively. The total soil depth is 2 m, with the lower 1 m acts as a reservoir with gravity drainage at the bottom, and the upper 1-m soil serves as the root zone depth. Soil and vegetation types are the primary variables to drive the LSM. Prognostic variables include soil moisture and temperature in the soil layers, water intercepted on the canopy and snow accumulated on the ground. In coupled mode LSM simulations, atmospheric model MM5 provides the near-surface meteorological fields of surface radiation, precipitation, winds, and temperature for the external forcing to the LSM. On the other hand, the LSM feeds back surface energy balance components of net radiation, surface skin temperature, latent, sensible, and ground heat fluxes as the lower boundary condition to MM5.

3.2 Model Thermodynamics

One of the primary functions of the coupled land surface model is to provide the near-surface layer of an atmospheric model with sensible and latent heat fluxes, as well as surface skin temperature to compute upward longwave radiation. The surface skin temperature is determined following Mahrt and Ek (1984) by applying a single linearized surface energy balance equation:

$$T_{skin} = \frac{R_n - \lambda E - G}{\rho C_p C_h |U_a|} + T_a \qquad (3\text{-}1)$$

where Rn is the net radiation (W m^{-2}), G is the ground heat flux (W m^{-2}), λE is the latent heat flux (W m^{-2}), Cp is the air heat capacity (J m^{-3} K^{-1}), U_a is the surface layer wind speed (m s^{-1}), and T_a is the near-surface air temperature (K). Equation (3-1) expands the

sensible heat flux (H) term such that the relationship can be expressed in terms of T_{skin}. As the skin is treated as an infinitesimally thin layer, and has no thermal inertia (heat capacity) of its own, the skin temperature may be very sensitive to forcing (especially radiation) errors. This expression has to be solved iteratively due to the implicit relationship, as some of the terms on the right hand side of the equation also contain skin temperature. The ground heat flux is governed by the diffusion equation for soil temperature (T):

$$C(\theta)\frac{\partial T}{\partial t} = \frac{\partial}{\partial z}\left(K_t(\theta)\frac{\partial T}{\partial z} \right) \tag{3-2}$$

where C is the volumetric heat capacity (J m^{-3} K^{-1}) and K_t is the thermal conductivity (W m^{-1} K^{-1}), and both are functions of θ; θ is fraction of unit soil volume occupied by water; and t and z are time (s) and the vertical distance (m) from the soil surface downward (i.e., the depth), respectively.

C and K_t are formulated as functions of volumetric water content, θ, and are given by:

$$C(\theta) = \theta C_{water} + (1-\theta_s)C_{soil} + (\theta_s - \theta)C_{air} \tag{3-3}$$

$$K_t(\theta) = \begin{cases} 420e^{-(2.7+P_f)}, 0 \le P_f \le 5.1 \\ 0.1744, P_f > 5.1 \;\&\; P_f < 0 \end{cases} \tag{3-4}$$

$$P_f = \log\left(\psi_s \left(\theta_s / \theta \right)^b \right) \tag{3-5}$$

The volumetric heat capacities are C_{water} = 4.2 x 10^6 J m^{-3} K^{-1}, C_{soil}=1.26 x 10^6 J m^{-3} K^{-1}, and C_{air} = 1004 J m^{-3} K^{-1}. θ_s and ψ_s are maximum soil moisture (porosity) and

saturated soil potential (suction), respectively, and both depend on the soil texture (Cosby et al., 1984). The K_t relationship used in the LSM, as suggested by McCumber and Pielke (1981), has been used in many land surface models (e.g. Noihan and Planton, 1989; Viterbo and Beljaars, 1995). However, Peters-Lidard et al. (1998) showed that this approach tends to overestimate/underestimate K_t during wet/dry periods, and the surface heat fluxes are sensitive to the treatment of thermal conductivity. In the LSM, K_t is capped at 1.9 W m^{-1} K^{-1}. Chen and Dudhia (2001) suggested that several thermal conductivity formulations are needed to arrive at the best approach.

Expanding Equation (3-2) for the *i*-th soil layer, yields:

$$\Delta z_i C_i \frac{\partial T_i}{\partial t} = \left(K_t \frac{\partial T}{\partial z} \right)_{z_i+1} - \left(K_t \frac{\partial T}{\partial z} \right)_{z_i} \tag{3-6}$$

where Δz_i is the thickness (m) of the *i*-th soil layer. The prediction of T_i is performed using the fully implicit Crank-Nicholson scheme. In the top layer the last term in Equation (3-6) represents the surface ground heat flux and is computed using the surface skin temperature. The gradient at the lower boundary, assumed to be 3 m below the ground surface, is computed from a specified constant boundary temperature and is taken as the mean annual near-surface air temperature.

3.3 Model Hydrology

The prognostic equation for the volumetric soil water content (θ) in the hydrology of the LSM is given by

$$\frac{\partial \theta}{\partial t} = \frac{\partial}{\partial z}\left(D \frac{\partial \theta}{\partial z} \right) + \frac{\partial K}{\partial z} + F_\theta \tag{3-7}$$

where D and K are the soil water diffusivity ($m^2\ s^{-1}$) and hydraulic conductivity ($m\ s^{-1}$), respectively, and both are functions of θ; t and z are time (s) and the vertical distance (m) from the soil surface downward (i.e., the depth), respectively; and F_θ represents sources and sinks (i.e., precipitation, evaporation and runoff). This diffusive form of the relationship is known as Richard's equation and is derived from Darcy's Law for movement of water in soils (with the assumption of a rigid, isotropic, homogeneous, and one dimensional vertical flow domain) (Hanks and Ashcroft, 1986). The soil water diffusivity (D) is given by

$$D = K(\theta)\left(\frac{\partial \psi}{\partial \theta}\right) \tag{3-8}$$

where ψ is the soil water tension function. Cosby et al. (1984) computed K and ψ using the empirical functions

$$K(\theta) = K_s\left(\frac{\theta}{\theta_s}\right)^{2b+3} \tag{3-9}$$

and

$$\psi(\theta) = \frac{\psi_s}{\left(\frac{\theta}{\theta_s}\right)^{b}} \tag{3-10}$$

where K_s, ψ_s, θ_s and b are the saturated hydraulic conductivity, saturated soil water tension, saturation value of volumetric water content, and a curve-fitting parameter respectively. They all depend on the soil type.

K and D are highly non-linear functions of soil moisture and in particular when the soil is dry, they can change very rapidly by several orders of magnitude, for a small

variation of soil moisture. As the soil-water parameterization is very sensitive to the diurnal partitioning of surface energy into latent and sensible heat (Cuenca et al., 1996), Chen and Dudhia (2001) suggested the investigation of alternative soil hydraulic parameterization schemes that would effectively accommodate the dynamic relationship between hydraulic conductivity and soil moisture.

Expanding the source and sink term (F_θ) and integrating Equation (3-7) over four soil layers, as used in the MM5 model, yields:

$$d_{z1}\frac{\partial\theta_1}{\partial t} = -D\left(\frac{\partial\theta}{\partial z}\right)_{z1} - K_{z1} + P_d - R - E_{dir} - E_{t1} \tag{3-11}$$

$$d_{z2}\frac{\partial\theta_2}{\partial t} = D\left(\frac{\partial\theta}{\partial z}\right)_{z1} - D\left(\frac{\partial\theta}{\partial z}\right)_{z2} + K_{z1} - K_{z2} - E_{t2} \tag{3-12}$$

$$d_{z3}\frac{\partial\theta_3}{\partial t} = D\left(\frac{\partial\theta}{\partial z}\right)_{z2} - D\left(\frac{\partial\theta}{\partial z}\right)_{z3} + K_{z2} - K_{z3} - E_{t3} \tag{3-13}$$

$$d_{z4}\frac{\partial\theta_4}{\partial t} = D\left(\frac{\partial\theta}{\partial z}\right)_{z3} + K_{z3} - K_{z4} \tag{3-14}$$

where d_{zi} is the i-th soil layer thickness, P_d is the precipitation not intercepted by the canopy, R is the surface runoff, and E_{ti} is the canopy transpiration taken by the canopy root in the i-th layer with the root-zone layers. The soil water flux at the bottom of the model domain (i.e., drainage) is determined from the gravitational percolation term K_{z4}, and by assuming the hydraulic diffusivity to be zero at the bottom of the soil model.

Surface runoff is addressed in the LSM using the Simple Water Balance (SWB) model approach given by Schaake et al. (1996). The SWB model is two-reservoir hydrological model that has been well calibrated for large river basins. It takes into account the spatial heterogeneity of rainfall, soil moisture, and runoff. The excess of

precipitation that is not infiltrated into the soil is termed surface runoff ($R = P_d - I_{\max}$), where the maximum infiltration, I_{max}, is given as:

$$I_{\max} = P_d \frac{D_x\left(1 - e^{(-kdt\delta i)}\right)}{P_d + D_x\left(1 - e^{-kdt\delta i}\right)} \tag{3-15}$$

$$D_x = \sum_{i=1}^{4} \Delta Z_i \left(\theta_s - \theta_i\right) \tag{3-16}$$

$$k_{dt} = k_{dtref} \frac{K_s}{K_{ref}} \tag{3-17}$$

δ_i is the conversion of the current model time step δ_t (in seconds) into daily values ($\delta_i = \delta_t / 86400$), K_S is the saturated hydraulic conductivity which depends on soil texture, D_x is soil moisture deficit, θ_s is the volumetric water content at saturation point, θi is the actual volumetric water content, k_{dt} is a runoff parameter, and K_{dtref} = 3.0 and K_{ref} = 2 x 10^{-6} m s^{-1}. Chen and Dudhia (2001) suggested the calibration of these parameters over various basins with different precipitation characteristics.

The total evaporation, E, as formulated in the LSM, is the sum of 1) the direct evaporation from the top shallow soil layer, E_{dir}, 2) evaporation of precipitation intercepted by the canopy, E_c, and 3) transpiration through canopy and roots, E_t.

$$E = E_{dir} + E_t + E_c \tag{3-18}$$

The simple linear expression for bare soil evaporation is:

$$E_{dir} = \left(1 - \sigma_f\right)\left(\frac{\theta - \theta_w}{\theta_{ref} - \theta_w}\right) E_p \tag{3-19}$$

where θ_w and θ_{ref} are the soil wilting point and field capacity (dimensionless), σ_f is the green vegetation fraction (dimensionless) which is critical for the partitioning of total evaporation between bare-soil direct evaporation and canopy transpiration, and E_p is the potential evaporation (m s^{-1}), calculated by a Penman-based energy balance and given by:

$$E_p = \frac{\Delta(R_n - G) + \rho\lambda C_h |u_a|(q^* - q)}{1 + \Delta} \tag{3-20}$$

where Δ is the local derivative of saturation specific humidity (q^*) with respect to temperature (dimensionless), R_n and G are the surface net radiation and ground heat flux (W m^{-2}), u_a is the surface layer wind speed (m s^{-1}), q is specific humidity and ρ, λ and C_h are the air density (Kg m^{-3}), latent heat of vaporization (J kg^{-1}), and surface exchange coefficient (m s^{-1}), respectively.

Evaporation of rainfall intercepted by the canopy is governed by:

$$E_c = \sigma_f E_p \left(\frac{W_c}{S}\right)^n \tag{3-21}$$

where W_c is the canopy intercepted water content (mm), S is the maximum allowed value for W_c (specified here as 0.5 mm), and n = 0.5. W_c is determined by a budget equation:

$$\frac{\partial W_c}{\partial t} = \sigma_f P - D - E_c \tag{3-22}$$

where P is the total precipitation (kg m^{-2} s^{-1}), and D is the drip or precipitation that reaches the ground (mm). This implies that P_d in Equation (3-11) is computed by:

$$P_d = (1 - \sigma_f)P + D \tag{3-23}$$

It is worthwhile to note that after significant rainfall, then W_c reaches S, and the time tendency is Equation (3-22) reduces to zero and $P_d \approx P$. In other words, additional rainfall drips off the canopy and reaches the ground (expect the small amount lost to E_c).

E_t is determined by:

$$E_t = \sigma_f E_p B_c \left(1 - \left(\frac{W_c}{S}\right)^n\right) \tag{3-24}$$

where B_c (dimensionless) is a function of canopy resistance and is expressed as :

$$B_c = \frac{1 + \frac{\Delta}{R_r}}{1 + R_c C_h + \frac{\Delta}{R_r}} \tag{3-25}$$

where R_r (dimensionless) is a function of surface air temperature, surface pressure and C_h (m s^{-1}), and R_c is the canopy resistance (s m^{-1}). Details on C_h, R_r, and Δ are given by Ek and Mahrt (1991). R_c is calculated using the formulation of Jacquemin and Noilhan (1990):

$$R_c = \frac{R_{c\min}}{LAI \cdot F_1 F_2 F_3 F_4} \tag{3-26}$$

where

$$F_1 = \frac{R_{c\min} \Big/ R_{c\max} + f}{1 + f} \tag{3-27}$$

$$f = 0.55 \frac{R_g}{R_{gl}} \frac{2}{LAI} \tag{3-28}$$

$$F_2 = \frac{1}{1 + h_s\left(q_s\left(T_a\right) - q_a\right)} \tag{3-29}$$

$$F_3 = 1 - 0.0016\left(T_{ref} - T_a\right)^2 \tag{3-30}$$

$$F_4 = \sum_{i=1}^{3} \frac{\left(\theta_i - \theta_w\right) d_{zi}}{\left(\theta_{ref} - \theta_w\right)\left(d_{z1} + d_{z2}\right)} \tag{3-31}$$

F_1, F_2, F_3 and F_4 are all subject to 0 and 1 as lower and upper bounds and they represent the effects of solar radiation, vapor pressure deficit, air temperature and soil moisture, respectively. LAI is the leaf area index, R_{cmin} is the minimum stomatal resistance, and R_{cmax} is the cuticular resistance of the leaves and is specified as 5000 s m^{-1} as in Dickinson et al. (1993). R_{gl} (visible solar flux) is 100 W m^{-2} and R_g is determined from radiation physics (Jacquemin and Noilhan, 1990); $q_s(T_a)$ is the saturated water vapor mixing ratio at the air temperature T_a and q_a is the actual specific humidity. The parameter T_{ref} is 298 K (Noilhan and Planton, 1989). The soil moisture stress function, F_4, embodies a linear relationship in soil moisture stress between the field capacity θ_{ref} and the wilting point θ_w, and is only integrated in the root zone which encompasses the first three soil layers in the current formulation.

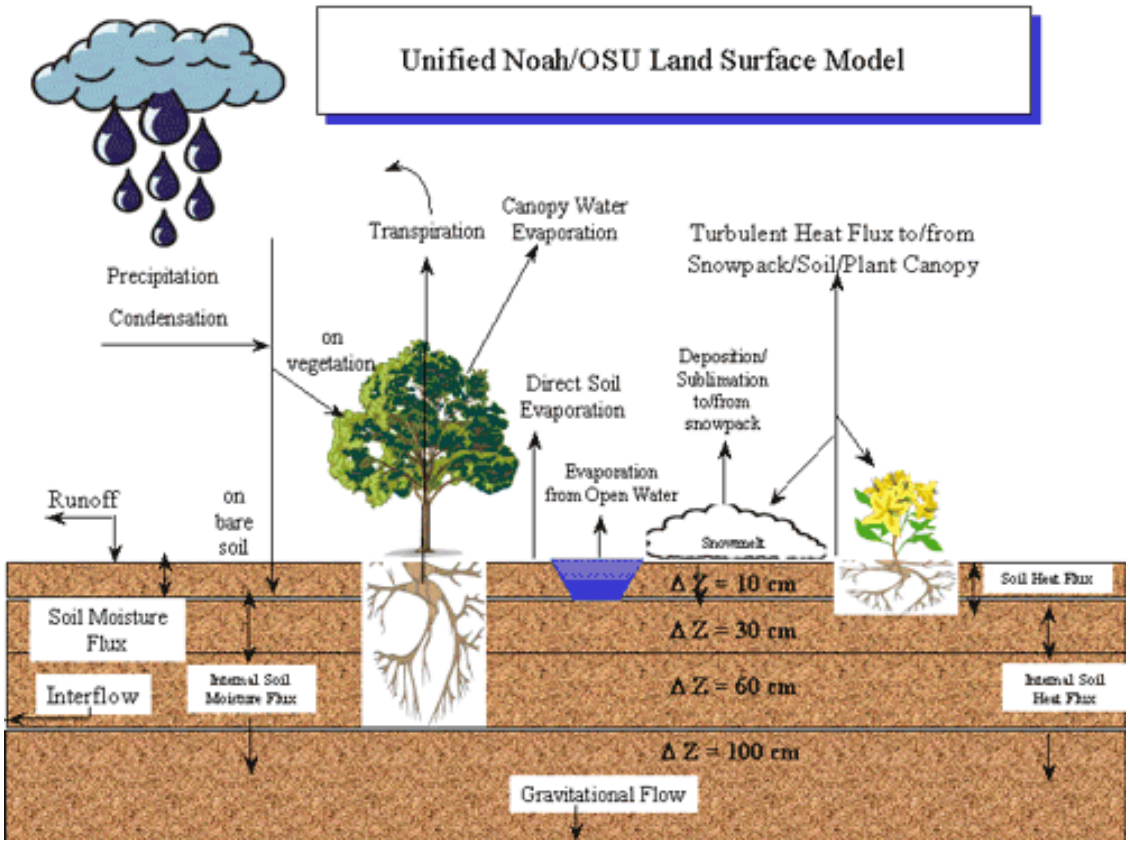

Figure 3-1: A schematic representation of the Noah LSM.

Chapter 4 Implication of Rapid Urban Growth on the Meteorological Conditions in the Pearl River Delta Region

Abstract

The Pearl River Delta (PRD) region, located in the southern part of Guangdong Province in China, is one of the most rapidly developing regions over the world. The evolution of local and regional sea-breeze circulation (SBC) is believed to be responsible to form meteorological conditions for high air pollution events in the PRD. To better understand the impacts of urbanization and its associated urban heat islands on the local and regional scale atmospheric circulations over PRD, a number of high-resolution numerical experiments, with different approaches to treat the land surface and urban processes, have been conducted using the Fifth Generation Penn State/NCAR Mesoscale Model (MM5). Our results show that an accurate urban land-use dataset and a proper urban land-use parameterization are critical for mesoscale models to capture the major features of observed urban heat island effect and land-sea breeze circulations in the PRD. Stronger urban heat island in the PRD increases the differential temperature gradient between urbanized areas and nearby ocean surface, and hence enhances the mesoscale SBC. Consequently, the SBC front penetrates further inland to overcome the prevailing easterly flow in the western part of inland Hong Kong. Additional sensitivity studies indicate that further industrial development and urbanization will strengthen the day-time SBC as well as increase the air temperature in the lowest 2-km atmosphere.

4.1 Introduction

It has been known for some time that urban cities are warmer than their rural surroundings. In cities, where there is less evaporative cooling, buildings and artificial surfaces are typically more capable of storing solar energy than natural surfaces. In addition, the human and industrial activities produce extra heat to the ambient environment causing higher near-surface temperature in a city. This phenomenon is called urban heat island (UHI) effect. It has been observed since the 1960s (Woolum, 1964; Bornstein, 1968) and air temperature in a city can be 1-4°C higher than the surrounding countryside (WMO, 1984). In the past 30 years, a number of climatological and observational studies have recognized that the UHI can have a significant influence on local-scale and mesoscale weather as well as micro-climate. Early climatological studies (Khemani and Murty, 1973; Changnon et al., 1976; Braham, 1979) pointed out that UHI can increase cloudiness and precipitation in a city. Observations (Vukovich, 1971; Bornstein, 1975; Sawai, 1978) also found that in a calm and weak synoptic forcing situation, heat island circulation (HIC) can be generated between a city and surrounding region.

The Pearl River Delta (PRD), located in the southern part of Guangdong Province in China, is a region of 41,700 km^2 in size and 50 million in population. Major cities in the region include Hong Kong, Guangzhou, Shenzhen, Dongguan, Zhongshan, Foshan, and Macau (see Figure 4-1a). As a result of the economic reform started at the end of the 1970s, the economic and industrial growths in the PRD have been phenomenal. The region is now one of the world's largest manufacturing and industrial

bases. However, the rapid urbanization has been causing several environmental impacts in the region such as climate change and substantial air quality deterioration.

According to Hong Kong Observatory (HKO), the UHI effect accounts for the difference of 8°C or above in the daily minimum temperatures between urban and rural areas in Hong Kong during winter (Leung and Ng, 1997). The urban development also related to the reduction of visibility, increase in cloud amount and decrease of solar radiation. The number of heavy rain days has also increased during the period 1947 to 2002 in Hong Kong (Leung et al., 2004). From the annual report by the Hong Kong Environment Department (HKEPD) (HKEPD, 2003), the percentage of time of having poor visibility and the number of ozone (O_3) episode day has been showing an increasing trend in the recent years. The number of days with poor visibility had also increased in the major PRD cities such as Guangzhou, Shenzhen (Ch2M Hill, 2002). These indicate the deteriorating air quality in Hong Kong and the entire PRD region.

Many urban areas in the PRD are located near the coast zone, with a calm winds or weak synoptic forcing where most serve air pollution episodes are occurred, sea breeze circulation (SBC) as well as UIC can occur at the PRD. The SBC has been known to be a significant influence on air flow pattern and affect the air quality over Hong Kong (Kok et al., 1997; Huang et al., 2005; Fung et al., 2005). On 1-3 November of 2003, a record high air-pollution episode occurred in Hong Kong and PRD. The air pollution index (API) had topped 200 and the Hong Kong Environmental Protection Department (HKEPD) issued the first severe air pollution warning since air quality monitoring was introduced in 1995. One of the main reasons causing this pollution

episode given by Wu et al. (2005) is a long-period accumulation of pollutants in PRD by land-sea breeze circulation before the event.

However, due to limited monitoring stations and observations, the SBC and UIC structures in PRD are still not well understood. To better manage the rapid deteriorating air quality, a better understanding of the local and regional circulation, including the complex interactions between the local SBC and the urban environment in the PRD, is needed. It is generally agreed that land surface process has substantial influence on both large-scale and mesoscale circulation (Chen and Dudhia, 2001). Accurate description of land surface fluxes is important for capturing the evolution of the diurnal planetary boundary layer (PBL), a parameter of primary importance for air quality studies. An air quality model could perform well without a good meteorological condition input from meteorological model, while fine scale meteorological model could perform well without a good parameterization of urban land-use. Hence, in this study we used a mesoscale model coupled to different approaches of treating urban land-use to investigate the formation of meteorological conditions conducive to the 1-3 November, 2003, high air-pollution episode.

This study investigated the impacts of rapid urbanization in the PRD on the local- and regional-scale circulations. In the first part, we used a non-hydrostatic, three-dimensional mesoscale meteorological model MM5 to understand and evaluate the three different approaches to treat the UHI and their effects on SBC structures over Hong Kong and the PRD region. The first MM5 experiment used the default MM5 surface characteristics with a simple land surface model (MM5-slab) (Dudhia, 1996). The second experiment was carried out by replacing the standard MM5 land-use with an up-

to-date PRD land-use dataset. The third experiment further enhanced the second experiment with an advanced land surface model (Noah LSM) (Chen and Dudhia, 2001) with a bulk urban land-use treatment. After the evaluation of model performances, sensitivity experiments were conducted for various urban coverage extensions in order to understand the potential effects of rapid urban growth on the local wind and temperature structures in the PRD. We present in Section 4.2 the numerical models and data used in this study. Section 4.3 summarizes the results from numerical simulations using three different urban land-use treatments and their evaluation. In Section 4.4, numerical experiments using different scenarios of urban extension are explored.

4.2 Numerical Models and Land-Use Distribution in the PRD

4.2.1 Meteorological Model and Configuration

The meteorological model used in this study is the Pennsylvania State University-National Center for Atmospheric Research Fifth-Generation Mesoscale Model (MM5) version 3.6.3. It is a limited-area, non-hydrostatic, primitive equation model with terrain-following sigma-coordinate (Dudhia, 1993; Grell et al., 1994). It has been a widely used community model designed to predict mesoscale and regional-scale atmospheric circulations. Previous studies also proved that MM5 has good performances in numerical weather prediction, air quality studies and hydrological studies over different part of the world (Warner et al., 1991; Mass and Kuo, 1998; Vaughan et al., 2004).

Figure 4-2 shows the model domains. Four nested domains with resolution 40.5 (D1, mesh size of 233 x 188), 13.5 (D2, mesh size of 133 x 148), 4.5 (D3, mesh size of

100 x 91) and 1.5 km (D4, mesh size of 151 x 136) were used. Two-way nesting was used such that meteorological variables in an inner domain could be fed back to the coarse domain, and vice versa, through the nested boundary (Zhang et al., 1986). The Lambert Conical Conformal map projection was used as the model horizontal coordinates with true latitudes at 30°N and 60°N. The outermost 40.5-km domain covers the entire China is designed to capture the synoptic-scale features while the innermost 1.5-km domain covers Hong Kong and PRD is designed to resolve local scale circulation features. The verifications and detailed analysis of model results were conducted on D4. Thirty five full sigma-levels[1] from surface to 100 hPa were used, of which the lowest twelve levels are below 1 km in order to have a finer resolution of the Planetary Boundary Layer (PBL). The height of the lowest model layer corresponds to about 10 m above the surface.

The simple explicit microphysical parameterization for cloud water, rain water and ice was applied in all domains (Dudhia, 1993). The Grell convective parameterization scheme was used in D1 and D2 (Grell, 1993), while explicit convection used in D3 and D4. Short wave radiation processes were handled using a cloud radiation scheme (Grell et al., 1994) and Rapid Radiative Transfer Model (RRTM) (Mlawer et al., 1997) was applied for long wave radiation processes. NCEP's Medium-Range Forecast scheme (MRF) was applied for the PBL scheme (Hong and Pan, 1996).

The MM5 runs were initialized using the 1° x 1° National Centers for Environment Prediction (NCEP) Final Analysis (FNL) data as first guess fields. The

[1] Full sigma level = 0.999, 0.997, 0.995, 0.992, 0.988, 0.983, 0.976, 0.967, 0.956, 0.943, 0.927, 0.908, 0.886, 0.860, 0.830, 0.795, 0.755, 0.715, 0.675, 0.635, 0.595, 0.555, 0.515, 0.475, 0.435, 0.395, 0.355, 0.315, 0.275, 0.235, 0.195, 0.155, 0.110, 0.060, 0.000. The vertical coordinate σ is defined as $(p - p_t)/(p_s - p_t)$, where p is pressure, p_s is surface pressure, and p_t is a constant pressure at model top (100hPa).

lateral boundary conditions of the outermost domain were obtained by linearly interpolating 6-hourly FNL data. Upper air and surface observations available on the Global Telecommunication System (GTS) were used to enhance MM5 initial conditions. In addition, upper radiation boundary condition of Klemp and Durran (1983) was used to reduce energy reflection from model top preventing noise and energy blown up vertically. The sea surface temperature was held constant during the simulations (Reynolds and Smith, 1994).

4.2.2 Land Surface Model and Parameterization of Urban Land-Use

The land surface model (LSM) used in MM5 was originally developed at Oregon State University (OSU) in the mid 1980s (Pan and Mahrt, 1987), and has been widely tested and evaluated (e.g., Chen et al., 1996, 1997; Berbery et al., 1996, 1999; Betts et al., 1997; Yucel et al., 1998; Hinkelman et al., 1999; Angevine and Mitchell, 2001; Berbery, 2001; Marshall et al., 2003). The OSU LSM and its successor the Noah LSM has been implemented as the land model component in NCEP operational Eta model (Chen et al., 1997; Ek et al., 2003) and state-of-the-art research model MM5 (Chen and Dudhia, 2001). The Noah LSM consisted of the diurnal dependent Penman potential evaporation approach of Mahrt and Ek (1984), the multi-layer soil model of Mahrt and Pan (1984) and the primitive canopy model of Pan and Mahrt (1987). Later improvements include a bare soil evaporation approach of Noilhan and Planton (1989), the canopy resistance formulation used by Jacquemin and Noihan (1990), and the surface runoff scheme of Schaake et al. (1996). The Noah LSM has one canopy layer and four soil layers. The soil layers thickness are 0.1, 0.3, 0.6 and 1.0 m from the ground surface to the bottom with total soil depth of 2 m. MM5 model simulations of surface

radiation, precipitation, and near-surface winds, humidity, and temperature provide the external forcing for the Noah LSM. The Noah LSM then provides surface sensible heat flux, latent heat flux and skin temperature as lower boundary condition to MM5. These heat and moisture fluxes are then used to drive the atmospheric boundary layer.

The Noah LSM has recently been enhanced with a simple parameterization for urban land-use (Liu et al. 2006). It includes: 1) increasing the roughness length from 0.5 m to 0.8 m to represent turbulence generated by roughness elements and drag due to building. 2) reducing surface albedo from 0.18 to 0.15 to represent the shortwave radiation trapping in the urban canyons; 3) using a larger volumetric heat capacity of 3.0 x 10^6 J m^{-3} K^{-1} for the urban surface (walls, roofs, and roads) which is usually consisted of concrete or asphalt materials; 4) increasing the value of soil thermal conductivity to 3.24 W m^{-1} K^{-1} to parameterize large heat storage in the urban surface and underlying surfaces, and 5) reducing green vegetation fraction and soil moisture over urban city to decrease evaporation. These urban land-use enhancements appear to have significant improvements to represent the urban physical processes over the Oklahoma City in US (Liu et al., 2006).

4.2.3 Rapid Urban Growth in the PRD Region in the Last Decade

In the coupled MM5/Noah modeling system, vegetation/land-use is one of the primary variables to control the land surface processes and the PBL structure, because various physical parameters of surface characteristics, such as albedo, emissivity, roughness length, thermal inertia are determined by the land-use category. In standard MM5, typical land-use classification is given by 30-second-resolution United States Geological Survey (USGS) global land cover characteristics database with 24 vegetation

categories. This land-use dataset is derived from 1-km Advanced Very High Resolution Radiometer (AVHRR) data in a 12-month period spanning from April 1992 to March 1993.

The USGS land-use distribution in the 1.5-km D4 is shown in Figure 4-3a. For simplicity, the 24-category USGS vegetation categories with similar properties are re-grouped into five major classifications: urban, cropland, grassland, forest, water and other. The contributions of the major land-use classifications in the 1.5-km D4 is illustrated in Table 4-1. From the USGS land-use map (Figure 4-3a), it can be seen that in the early 1990s, the majority of the PRD area was still an agricultural region, 45.6% of the domain land mass is cropland while urban areas only contribute 0.5%. Most major cities in the PRD such as Shenzhen, Dongguan, Guangzhou and Zhuhai (see Figure 4-1a for the locations) had not been highly urbanized and some of them were typical small rural towns. The Chinese economy began to take off in the early 1990s and massive urban development began to take place in Guangdong and in the PRD region. Consequently, the land-use distributions of the PRD have been undergoing rapid changes, and the 1993-based USGS land-use pattern may not be applicable any more and certainly underestimate the urban coverage in today's PRD.

In order to produce a long-term development strategy for the next 30 years, the Planning Department of the Government of Hong Kong (HKPD) has carried out a detailed study on land-use pattern in the PRD region in 2003 (HKPD, 2003). It produces an up-to-date 30 m resolution land-use dataset in the PRD region. In order to be compatible with the MM5, this land-use dataset with 17-category was re-mapped to corresponding USGS land-use 24-category vegetation categories. The mapping strategy

is summarized in Table 4-2. Dominant land-use of the 30 m HKPD land-use is derived into 30-sec USGS grid based on the standard interpolation algorithm used by MM5. For example, if the water coverage is more than 50% at the grid, water will be assigned to that grid; if the water coverage is less than 50%, the grid is assigned with the maximum percentage category excluding the water (Gou and Chen, 1994).

Figure 4-3b shows the new 2003 land-use in the 1.5-km D4 and the corresponding contributions of each land-use classification in the domain is listed in Table 4-1. Comparison of the land-use map between 2003 and USGS, one can see that there is a sharp increase in urbanized area. The 2003 land-use map reveals that about 13% of the land-use in the domain is urban, as compared to that of 0.5% of urban land-use in the early 1990s from the USGS land-use map. The decrease in the percentage of cropland from 45.6% to 22.7% also reveals a rapid transformation of PRD from an agricultural region into an industrial base during the past ten years. As the physical properties and parameters between cropland and urban areas are very different, it is expected that this rapid growth of the development should have a great impact on the local circulation.

In the standard MM5-Noah LSM, the green vegetation fraction is assigned by the monthly 5-year climatology of 0.15° AVHRR green vegetation cover data (Gutman and Ignatov, 1998). This parameter is an important weighting factor for bare-soil direct evaporation and plant transpiration. In the present MM5 simulations, the green vegetation fraction in the outer domains D1 and D2 was based on those monthly climatology data. However, there was a problem in interpolating the coarse-resolution AVHRR data into the MM5 inner 1.5-km domain and resulted in low and unrealistic

green vegetation fraction near the coastal regions. Most part of Hong Kong was assigned to a very low green fraction (20 to 30%) which is not realistic. Taking the advantages of the detailed PRD land-use data, we modified the green vegetation fraction in D3 and D4 according to the land-use category (see Table 4-2). Since PRD is located in subtropical region, the seasonal variation of green fraction is very small, thus, the green vegetation can be regarded as an annually invariant field.

The soil parameters in Noah LSM, such as soil temperature, soil moisture and soil water were initialized from the 47-km US Air Force Weather Agency's real-time global agricultural meteorology analysis model (AGRMET) data. The land model component of the AGRMET system also uses Noah LSM. For the urban land-use, we specifically fixed the soil moisture and soil water for all the soil layers as 0.1 m^3/m^3, which is the same as that in default MM5 land surface parameters. The soil moisture was fixed for urban land-use because the resolution of the AGRMET data is still very coarse compared to the inner domains, the soil parameters obtained from AGRMET may not have a good representation of the local characteristics in our finer domains, especially for the urban land-use.

In order to investigate the impact of different land surface treatments on the local circulations, three 36-hr MM5 experiments initialized at 0800 LST 30 October, 2003 have been conducted to study a severe air pollution episode in Hong Kong and PRD. One MM5 experiment used default USGS land-use map with simple land surface treatment MM5-slab (refereed to as SLAB). The second one used the up-to-date 2003 land-use with MM5-slab (refereed to as SLAB-LANDU). The last experiment used the up-to-date 2003 land-use with Noah LSM (refereed to as URBAN-LSM), which has an

enhancement on urban land-use treatment. Table 4-3 lists the similarities and differences between these three experiments.

4.3 Effects of Urban Heat Island in PRD Simulated by Three Different Approaches

4.3.1 Synoptic Weather Condition

On 1-3 November of 2003, a record high air-pollution episode occurred in Hong Kong and PRD with an air pollution index (API) of 200, and the Hong Kong Environmental Protection Department (HKEPD) issued the first severe air pollution warning since air quality monitoring was introduced in 1995. Concentrations of air pollutants such as suspended particulates (RSP), sulfur dioxide (SO_2), carbon monoxide (CO), and nitrogen oxides (NO_X) reached a very high level and exceeded the Air Quality Objectives (AQO) of Hong Kong. The record reading of ozone concentration topped at 402 $\mu g\ m^{-3}$, 67% higher than the AQO of 240 $\mu g\ m^{-3}$ in one hour. Wu et al. (2005) pointed out that a long-period accumulation of pollutants in PRD by land-sea breeze circulation before the event caused this pollution episode. In fact, just before the episode, there was a half month period of stationary weather in the whole southern China and PRD. Under those weakly forced weather conditions, land-sea breeze was the dominant circulation over Hong Kong and PRD.

Figure 4-4a shows the synoptic weather pattern on 0800 LST 31 October, 2003 provided by the Hong Kong Observatory (HKO). Under the influence of dry northeast monsoon, the weather was generally calm and fair over southern China and PRD. Meanwhile, a tropical storm Melor was formed at the east of the Philippines and was

moving northwest across northern Philippines toward Taiwan. From Hong Kong surface meteorological observations, the background wind over Hong Kong was weak easterly wind and SBC was prominent during the episode period.

Figure 4-4b shows the 24-hr simulated surface wind field and sea level pressure of D1 in URBAN-LSM experiment corresponding to the same time as the HKO weather chart. The outer computational domain actually is larger than the region shown in the figure. However, to facilitate the model comparison with the HKO weather chart, we focus on the areas of the East Asia. The simulated synoptic pattern generally agreed well with the HKO weather chart, and the location and intensity of typhoon Melor is also well simulated by the model. This well simulated synoptic pattern is an important criterion for a realistic simulation of local circulation. The simulated synoptic pattern of the SLAB and SLAB-LANDU experiment are similar to that of the URBAN-LSM experiment (not shown). Although these three experiments have a similar synoptic pattern, the simulated local circulations are quite different between them, as discussed in the next section.

4.3.2 Validation of Simulated Sea Breeze Circulation Features

The simulated surface wind fields (10 m AGL) of the three different land surface approaches on D4 (1.5-km grid spacing) is compared with observations at 1400 LST 31st October, 2003 in Hong Kong (Figure 4-5). Under the influence of the northeast high pressure system and typhoon Melor (see Figure 4-4a), the large-scale background wind over Hong Kong is weak easterly; but from observations as shown in Figure 4-5, the local wind is dominant by sea breeze circulation (SCB), which is pronounced in the western part of the New Territories and Lantau Island. Nevertheless, the simulations of

large-scale background winds over the ocean are similar in these three MM5 experiments, locations and structures of the SBC front over the Pearl River Estuary and over Hong Kong are clearly different. The SLAB experiment depicted SBC to some extent (Figure 4-5c), but the SBC front cannot penetrate into further inland because of its weaker land surface forcing. The western part of inland Hong Kong is still covered by background easterly wind. The SLAB simulated SBC front is located in the Pearl River around 15 km from the western seashore of Hong Kong. Based on the up-to-date land-use characteristics, the SLAB-LANDU experiment (Figure 4-5b) seems to capture the SBC in the western Hong Kong, but does not reproduce the observed SBC structure in the inland Hong Kong. By contrast, in the URBAN-LSM experiment, the SBC feature is well simulated (Figure 4-5a), and the strong SBC supersedes the background easterly wind. As a result, westerly wind is well developed in the western part of Hong Kong and southerly wind is prominent over the seashore between Lautau Island and Hong Kong Island.

In order to verify the temporal structure of the simulated winds and the arrival time of the SBC, temporal variations of the observed and simulated surface winds at three stations are shown in Figure 4-6. The three stations are: Waglan Island (WGL), which is located 10 km off the south-east Hong Kong Island serves as large-scale synoptic background winds information; Hong Kong International Airport (HKA) and Lau Fau Shan (LFS), which is located in the north-west Lautau Island and north-west New Territories respectively, are selected to provide the temporal SBC features for verification. As shown in Figure 4-6, observed background easterly winds are persistent for the whole 36-hr simulation period at WGL. The URBAN-LSM experiment generally

well captured these synoptic wind features. On the other hand, the winds patterns simulated by the SLAB-LANDU and SLAB experiments have around 10° systematic biases on wind direction. At the HKA and LFS, SBC is dominant from 1100 to 1800 LST, and is further enhanced on the second day (31st Oct). The SLAB experiment only simulated the weakening of the easterly background wind, but was not able to predict correctly the wind-direction changes as observed at the station. The SLAB-LANDU experiment has better timing of sea breeze than the SLAB. Among the three experiments, the URBAN-LSM produced the best spatial simulation of the sea breeze features and the timing of sea breeze was well captured, especially on the second day. Similar temporal verifications have been performed on other stations at the western part of Hong Kong and the results are similar to HKA and LFS.

From the verification of surface winds, it is clear that an advanced land-surface model, which provided better simulations of the surface heat flux and forcing, was able to reproduce the pattern of observed features of SBC in Hong Kong. The following sections will discuss the structure of the SCB development in the PRD by using the simulation results of the URBAN-LSM.

The temporal variations of surface streamlines from 1000 to 1600 LST 31 October, 2003 are shown in Figure 4-7. The onset of the SBC started near north-western and western part of the Pearl River coastal region around 1000 LST (Figure 4-7a). By noon (Figure 4-7b), the SBC front advanced to Hong Kong, and this westerly wind started to affect the western coast of Hong Kong. A huge divergence zone has developed over the Pearl River Estuary. By 1400 LST (Figure 4-7c), the SBC was more intensified and propagate further inland into the eastern PRD coastal region. By 1600 LST (Figure

4-7d), the SBC started to weaken: the divergence zone which located in the Pearl River Estuary disappeared while southerly wind was dominant over that region instead.

The vertical cross section of wind streams across the Pearl River at latitude of 22.55ºN at 1400 LST is shown in Figure 4-8. The exact location of this cross section is also marked (line AA') in Figure 4-7c. The right side of the vertical cross section is Shenzhen, which is a well developed city in PRD. It can be seen that the afternoon sea breeze circulations were well developed: several closed circulations are developed within the PBL over the coastal region, of which, the most prominent circulation zone is located over the Pearl River Estuary (113.5°E to 114.0°E). The extension of this circulation zone can reach to 50 km in horizontal dimension and 1.5 km in vertical dimension. From the figure, it is interesting to see that not only the SBC, but also the urban heat island circulation (UIC) has been generated between the urban areas in Shenzhen (around 114.15°E) and the surrounding region. Upward vertical velocity reaches to 60 cm s^{-1} in urban area; by contrast, downward 40 cm s^{-1} vertical motion is occurred in the surrounding rural areas.

4.3.3 Spatial Structures Urban Heat Island (UHI) in PRD

Table 4-4 summarizes the comparison between observed and model surface temperature at 33 monitoring stations in Hong Kong. This table is sorted by station mean temperature (36-hr average) in descending order and the locations of these 33 stations are shown in Figure 4-1b. Under the generally fair weather conditions in Hong Kong, the mean surface air temperature varied from 17°C to 26°C. Some stations such as the Peak (VP1), Tate's Cairn (TC) and Tai Mo Shan (TMS) are located in the mountainous

region and generally record lower temperature. Temperature in the urban areas such as Mong Kok (MK), Sham Shui Po (SP) and Hong Kong International Airport (HKA) are generally two to three degrees higher than that of the rural areas such as Tap Mun (TAP), Wagland Island (WGL), and Sai Kung (SKG).

The model results for each station from these three experiments (URBAN-LSM, SLAB-LANDU, and SLAB) were compared with hourly observations, mean-error (ME) and root-mean-square-error (RMSE) were also calculated. The sample size of the statistic is 36 from 0800 LST 30 October to 2000 LST 31 October, 2003. The SLAB surface air temperature has large cold biases and RMSE, especially for urban areas. The SLAB-LANDU improves the model performance by reducing the averaged cold bias and averaged RMSE. The URBAN-LSM experiment produced the best agreement with observations and the urban land-use enhancements reduced the cold bias in urban areas. Comparing with SLAB, both the averaged mean error and the averaged RMSE were reduced from -1.04 to -0.21 and from 1.85 to 1.01 degree respectively.

The distribution of UHI in PRD is clearly seen on Figure 4-9a, which shows the spatial variance of surface brightness temperature from 5-km resolution Moderate Resolution Imaging Spectroradiometer (MODIS) valid at 0200 LST 31 October, 2003. Spatial variance is the temperature at each grid point minus the domain-averaged temperature. At midnight in PRD, temperature in urban cities such as Guangzhou, Foshan, and Dongguan was significantly higher than the surrounding rural areas. Figure 4-9b shows the URBAN-LSM simulated UHI pattern. Temperature over ocean and urban areas are about 4-degree higher than the domain-averaged temperature in midnight. Similarly to the MODIS data, the main high-temperature region is around Guangzhou.

This type of UHI pattern was well captured by the simulations of the URBAN-LSM experiment. However, in the SLAB experiment, nocturnal UHI is less developed (Figure 4-9d), the temperature variation between rural and urban areas is very little, and its high temperature zones are only over the ocean. The UHI pattern from the SLAB-LANDU experiment is similar to that of SLAB (Figure 4-9c), indicating that a good simulation of UHI not only needs an up-to-date urban land-use distribution, but also needs realistic parameterizations on urban land-use.

Figure 4-10 shows land-point-domain-averaged diurnal cycle of surface air temperature and PBL height simulated for the urban and rural areas by URBAN-LSM. Urban areas are generally 2-degree warmer than rural areas, and the UHI is prominent for both daytime and nighttime. This 2-degree temperature difference during the day time appears to correspond to the 200 m deeper PBL in urban areas, however, the nocturnal urban PBL depth is not very different from that over the rural areas. Figure 4-11 shows the corresponding time series of the surface energy budgets from URBAN-LSM simulation. Compared to the rural areas, the dry urban areas produced smaller latent heat (evaporation), larger sensible and ground heat fluxes. The larger sensible heat flux is responsible for the daytime UHI, and the larger ground heat flux (i.e., more heat is stored in the ground during daytime and later released during nighttime) is responsible for nocturnal UHI.

4.4 Impacts of Urban Land-Use Change on Regional Meteorology in the PRD

We have seen in the last section that URBAN-LSM, with an enhancement of urban land-use treatment, was able to capture the major features of the observed surface temperature and wind structures in the PRD. In this section, we utilize the coupled MM5/Noah LSM to conduct several sensitivity experiments by changing the inner domains (D3 and D4) land-use in order to examine the urbanization effect on the meteorological condition over the PRD. In the first sensitivity test (refereed to as NO-URBAN), all urban land-use points in the URBAN-LSM control experiment were replaced by dry cropland (USGS category 2). In the second sensitivity test (refereed to as 2X-URBAN) all cropland points were converted into urban land-use, and it approximately doubles the total urban area in the simulation domains. In the third sensitivity test (ALL-URBAN), representing an extreme case, all land points were assigned as urban land-use, so that the domains only have either urban land-use or water body. The proportion of urban and cropland land-use in D4 of each sensitivity experiment is listed in Table 4-5. All these three experiments are conducted using identical initial conditions and physics schemes as the CONTROL simulation.

4.4.1 Impacts of Urban Land-Use Change on Sea Breeze Circulation

The generation of land-sea breeze circulations is largely controlled by the temperature differences between the ocean surface and the land surface. Because UHI produces higher temperature, the change in the distribution of urban area could affect air flow pattern within the region, particularly during daytime when higher sensible heat

flux and higher temperature of urban areas could have a strong influence on local circulations. Figure 4-12 shows the difference of surface horizontal wind at 1400 LST 31 October, 2003 between CONTROL and NO-URBAN (Figure 4-12a), and between ALL-URBAN and NO-URBAN (Figure 4-12b), respectively. Compared to NO-URBAN simulations, the CONTROL produced a stronger SBC in the eastern Pearl River coast. It is because most of that area has been developed into urban areas in the last 20 years, which produced a higher temperature, and hence intensified SBC. Therefore, it is not surprising that in ALL-URBAN, due to an even higher density of urban areas, SBC penetrated much further inland along the eastern coast. In addition, south-easterly SBC in western Pearl River estuary is intensified by the larger temperature contrast between water and the land.

4.4.2 Impacts of Urban Land-Use Change on PBL Temperature

From section 4.3.3, there is a clear evidence of temperature increase in the overall PRD areas as result of urbanization. Figure 4-13 shows the regional vertical temperature profile difference between CONTROL and the other three sensitivity tests (NO-URBAN, 2X-URBAN, and ALL-URBAN), which is the temperature averaged over all land points over D4. At 1400 LST, a fully converted urban land-use in the PRD produced an average of 1.5-degree higher near-surface temperature than the current land-use distribution in the PRD. The influence of land-use can reach as high as 2 km during daytime. Probably in the next decade, distribution of urban area is expected to be doubled, the surface temperature would increase by about 0.5 degree. On the other hand, without urban areas, the domain-averaged temperature would be reduced by about 0.5 degree.

4.5 Conclusion

In this chapter, three approaches of land surface treatments were used to examine the evolution of local and regional SBC conducive to a high air-pollution episode that occurred in Hong Kong and PRD on 1-3 November 2003. In the current MM5, the 1993-based USGS land-use data underestimated the urban areas extension in the rapidly expanded PRD region. Using this MM5 default land-use map and a simple slab land model, MM5 generated a weak SBC due to insufficient land surface forcing over urban areas. Moreover, a large temperature cold bias is found because of unrealistic land-use distribution. By contrast, using the MM5/Noah LSM, along with an up-to-date high resolution land-use map and enhancements of urban land-use treatment, it was able to capture major features of the observed surface temperature and wind-flow patterns in the PRD.

The role of urban land-use distribution and its associated urban heat island in modulating local and regional air-flow patterns in the PRD was investigated. It is demonstrated that a stronger urban heat island in the PRD increases the differential temperature gradient between urbanized areas and the nearby ocean surface, and hence enhances the mesoscale SBC. Consequently, the SBC front penetrates further inland to overcome the prevailing easterly flow in the western part of inland Hong Kong. Clearly, understanding the modifications of temperature and wind direction in the boundary layer in the PRD metropolitan and rural areas and correctly predicting them, is imperative to improve our ability to predict air quality and dispersion. A precise description of land-use in urban and rural regions proves critical toward establishing an urban air pollution prediction system. Through the sensitivity studies, the impact of urbanization on the

meteorological condition over the PRD was examined. The results showed that further urbanization could strengthen the SBC. With higher sensible heat fluxes, the temperature in the lowest 2-km atmosphere over urban areas can increase by about 1.5°C.

The results also suggest that the air pollution meteorology of the PRD region is strongly influenced by the local sea breeze circulation. The sea breeze convergence region is identified as the principal feature contributing the regional haze problem. The recirculation of pollutants caused by enhanced land-sea breeze circulation may be an important aspect of the local air pollution meteorology that is worthy of further investigation.

(a)

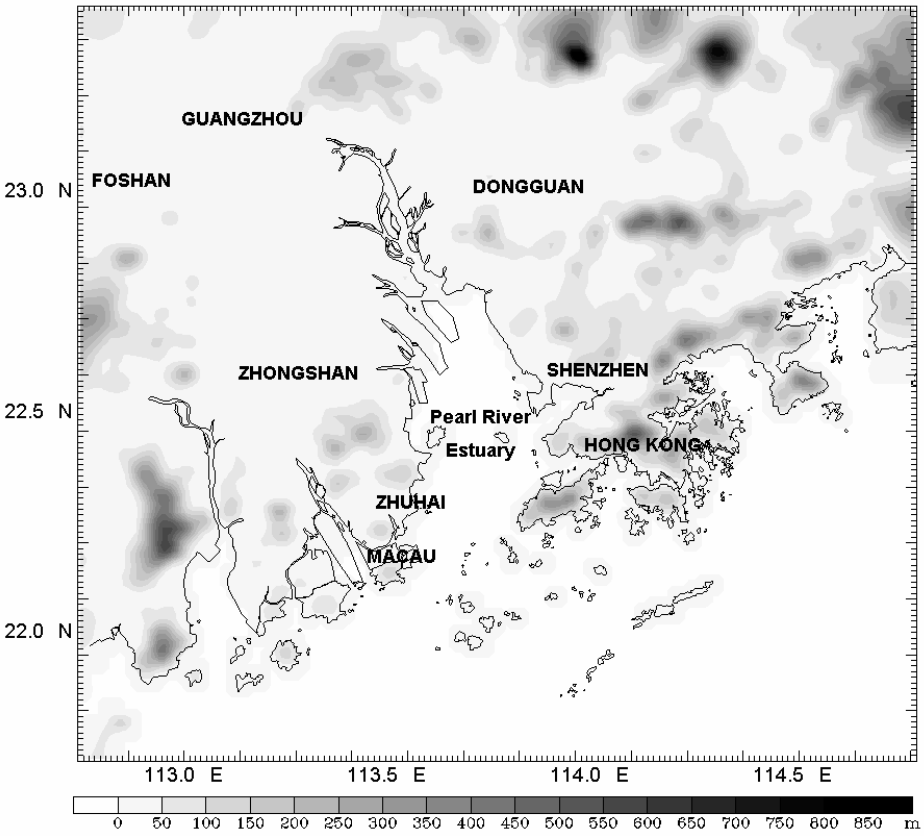

(b)

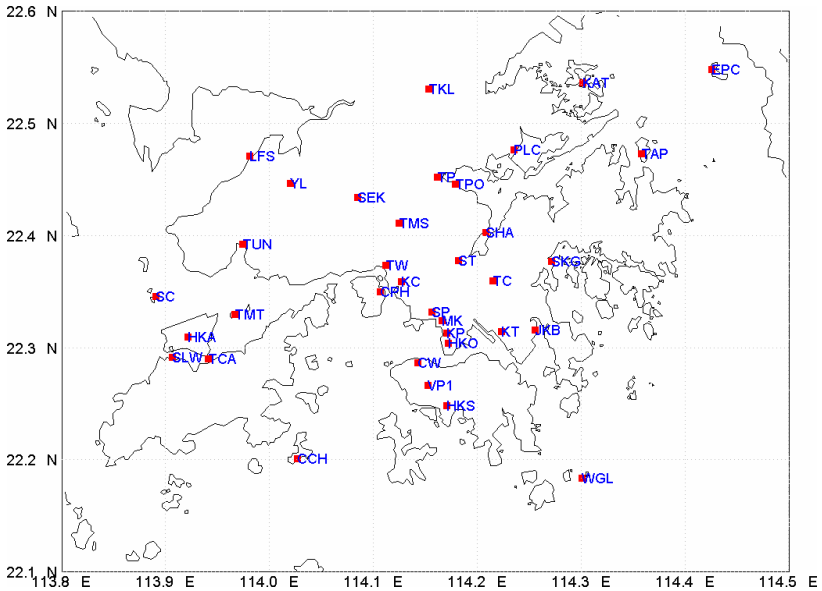

Figure 4-1: Map of Pearl River Delta Region. (a) Topography map and locations of major cities. Contours represent the terrain height, contour interval is 50 m. (b) Locations of the meteorological stations in Hong Kong used to evaluate the performance of the MM5 experiments.

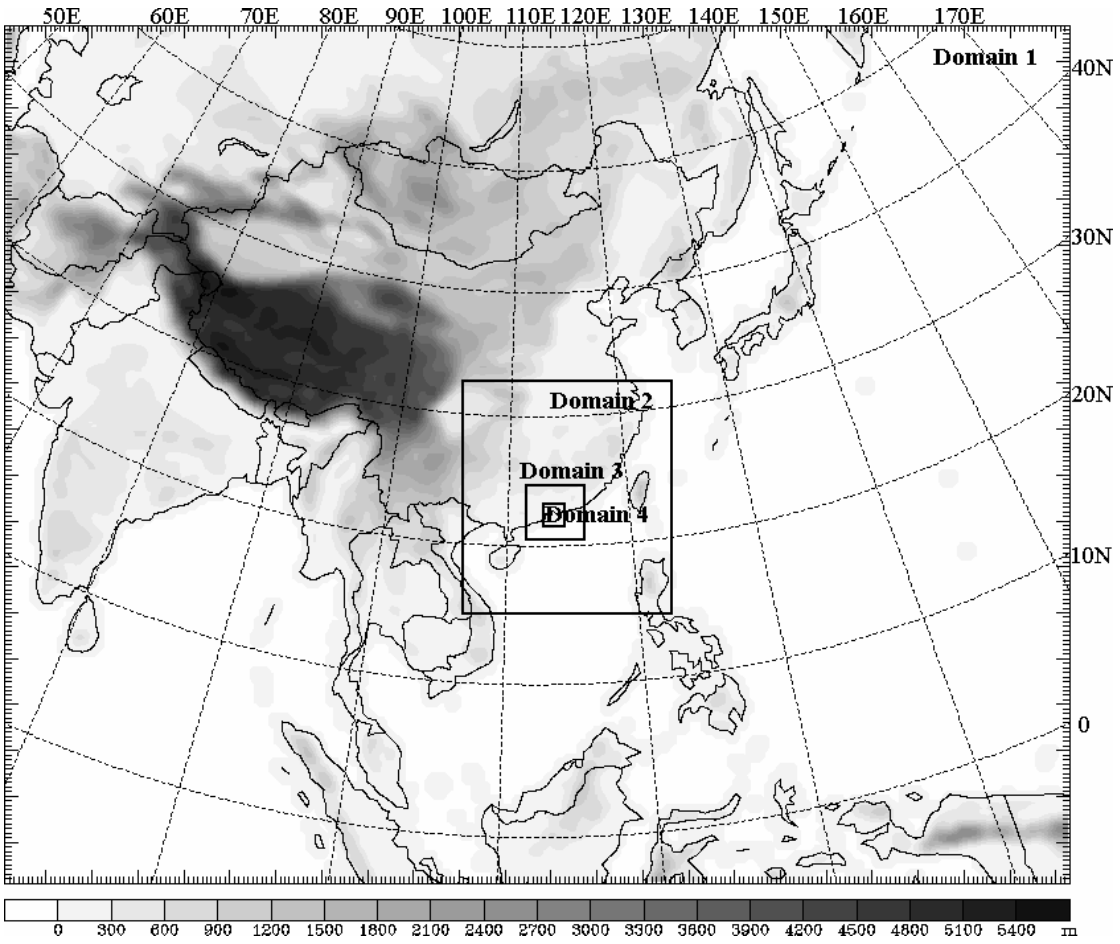

Figure 4-2: Configuration of the four two-way nested domains for MM5 simulations. Grid sizes of the domains are 40.5 km, 13.5 km, 4.5 km and 1.5 km. Terrain contour interval is 300 m.

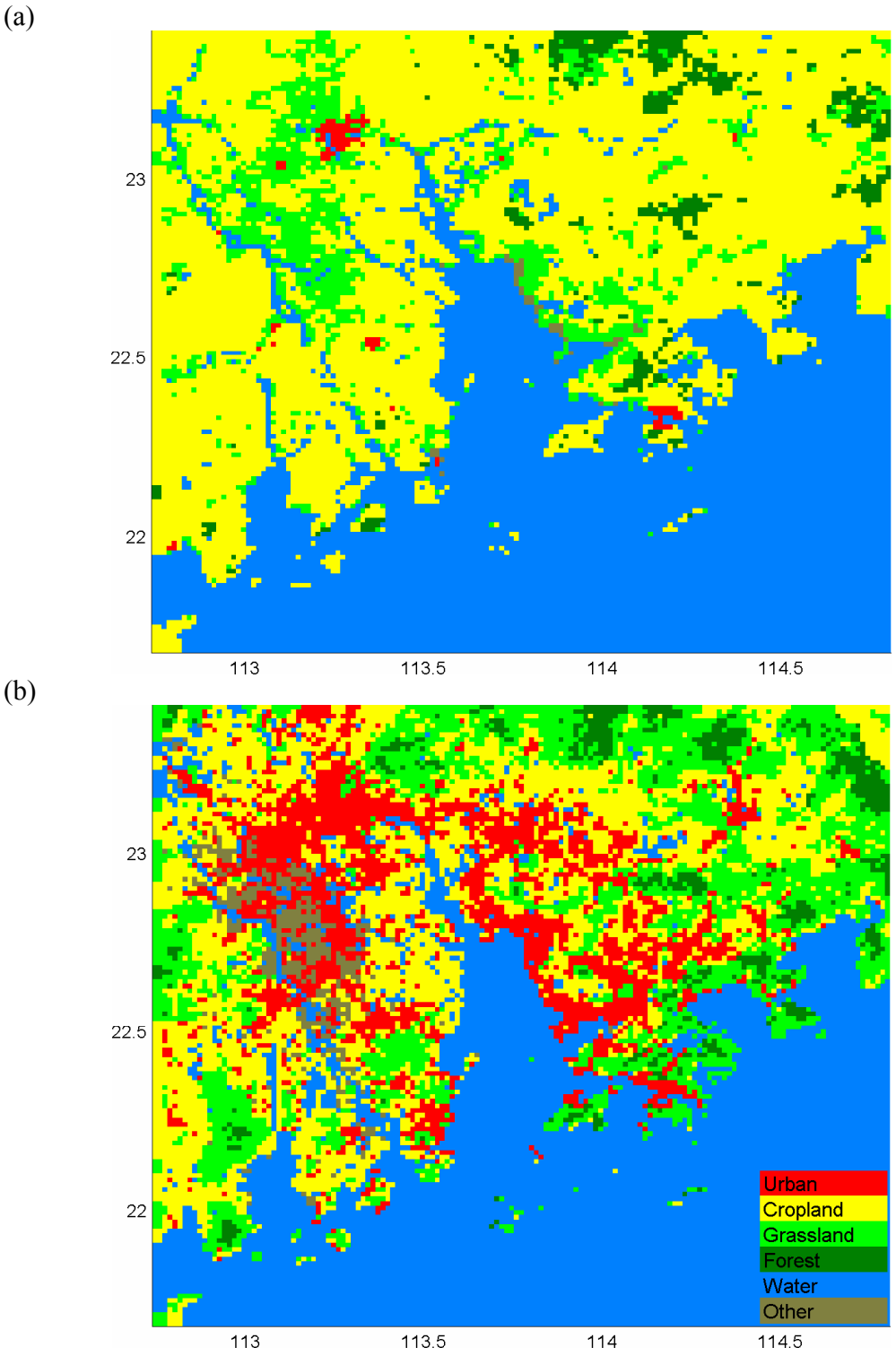

Figure 4-3: Land-use map of the inner-most 1.5-km D4. (a) Original USGS. (b) New 2003 land-use map. The colors indicate urban, cropland, grassland, forest, water and other according to the figure legend.

(a)

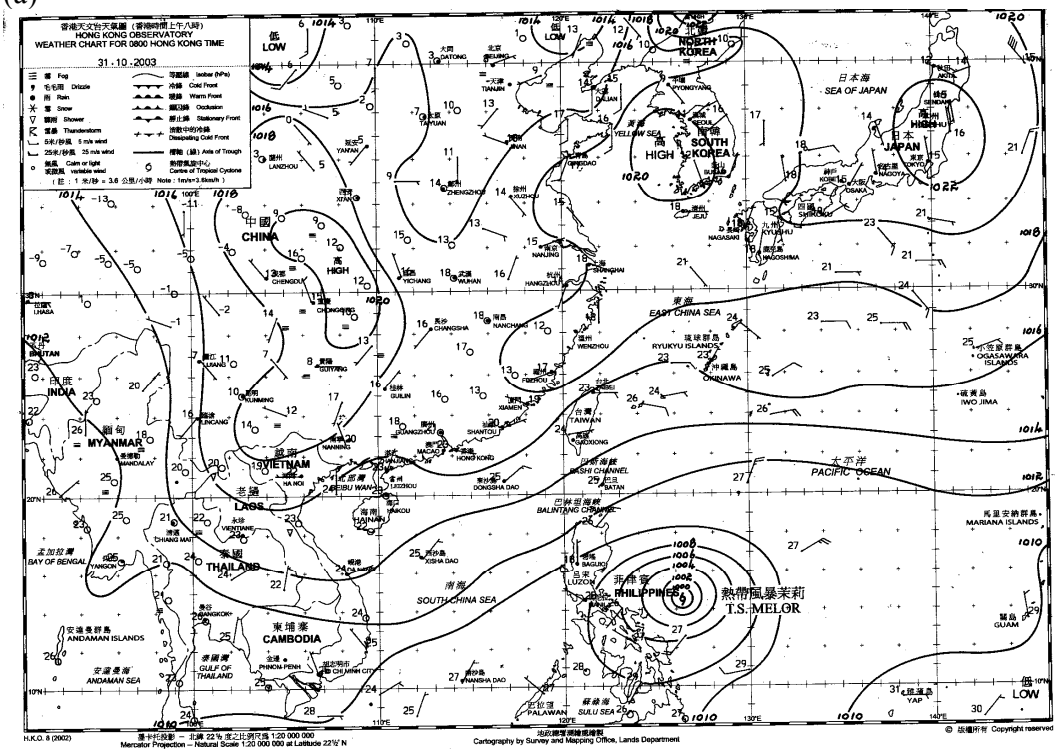

(b)

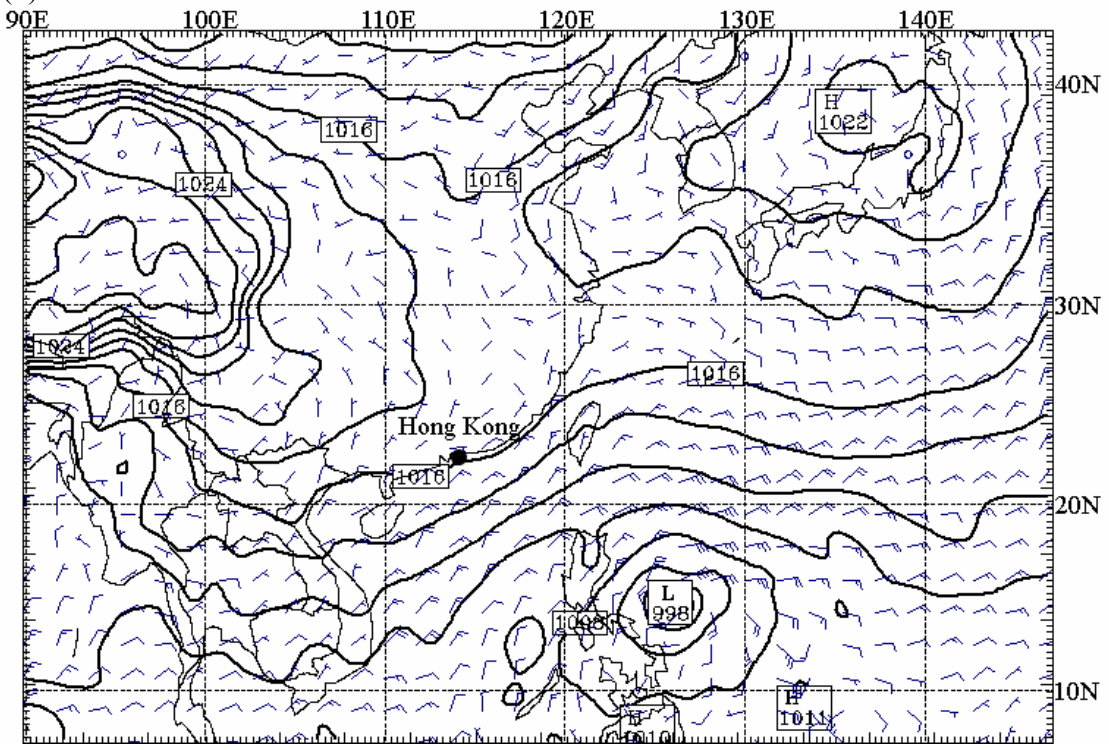

Figure 4-4: Synoptic weather condition on 0800 LST 31 October, 2003: (a) Hong Kong Observatory surface weather chart and (b) URBAN-LSM 24-hr forecast of D1. The contour line interval of sea level pressure is 2 hPa.

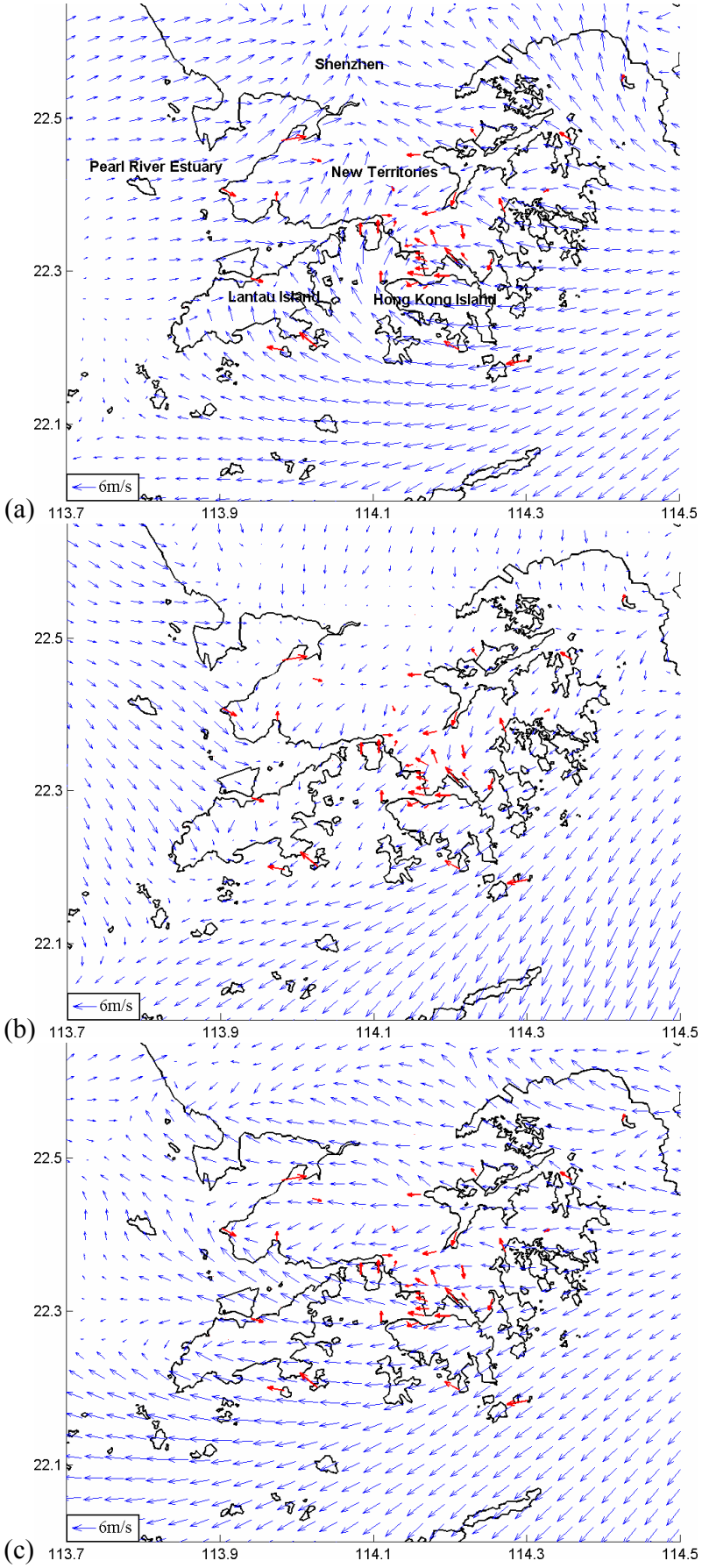

Figure 4-5: Simulation-observation of surface wind field valid at 1400 LST 31 October, 2003 from experiment of: (a) URBAN-LSM, (b) SLAB-LANDU, and (c) SLAB. Red colors indicate observations.

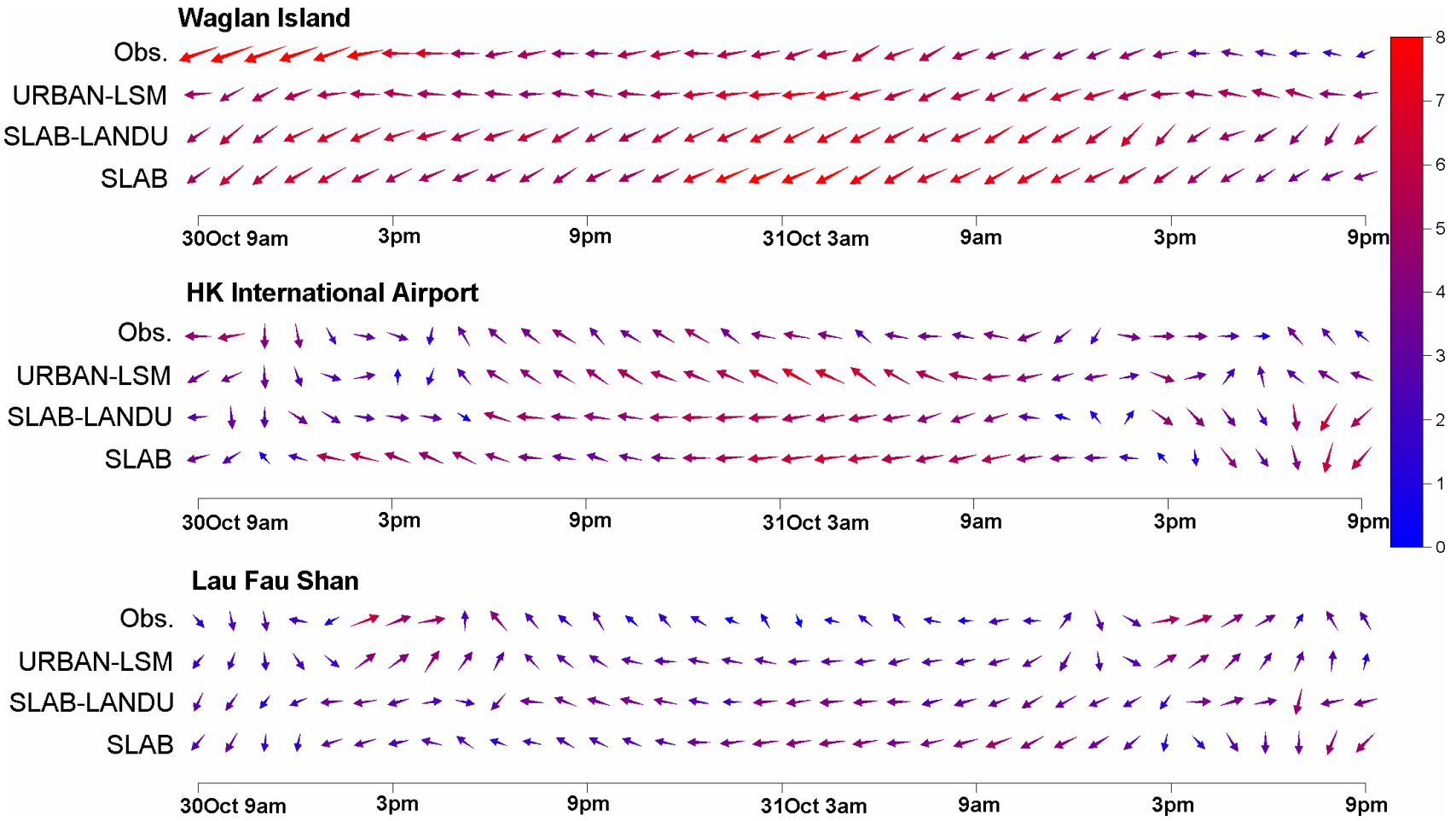

Figure 4-6: Time series of observed (Obs.) and simulated wind at three sites: Waglan island (WGL), HK international airport (HKA), and Lau Fau Shan (LFS).

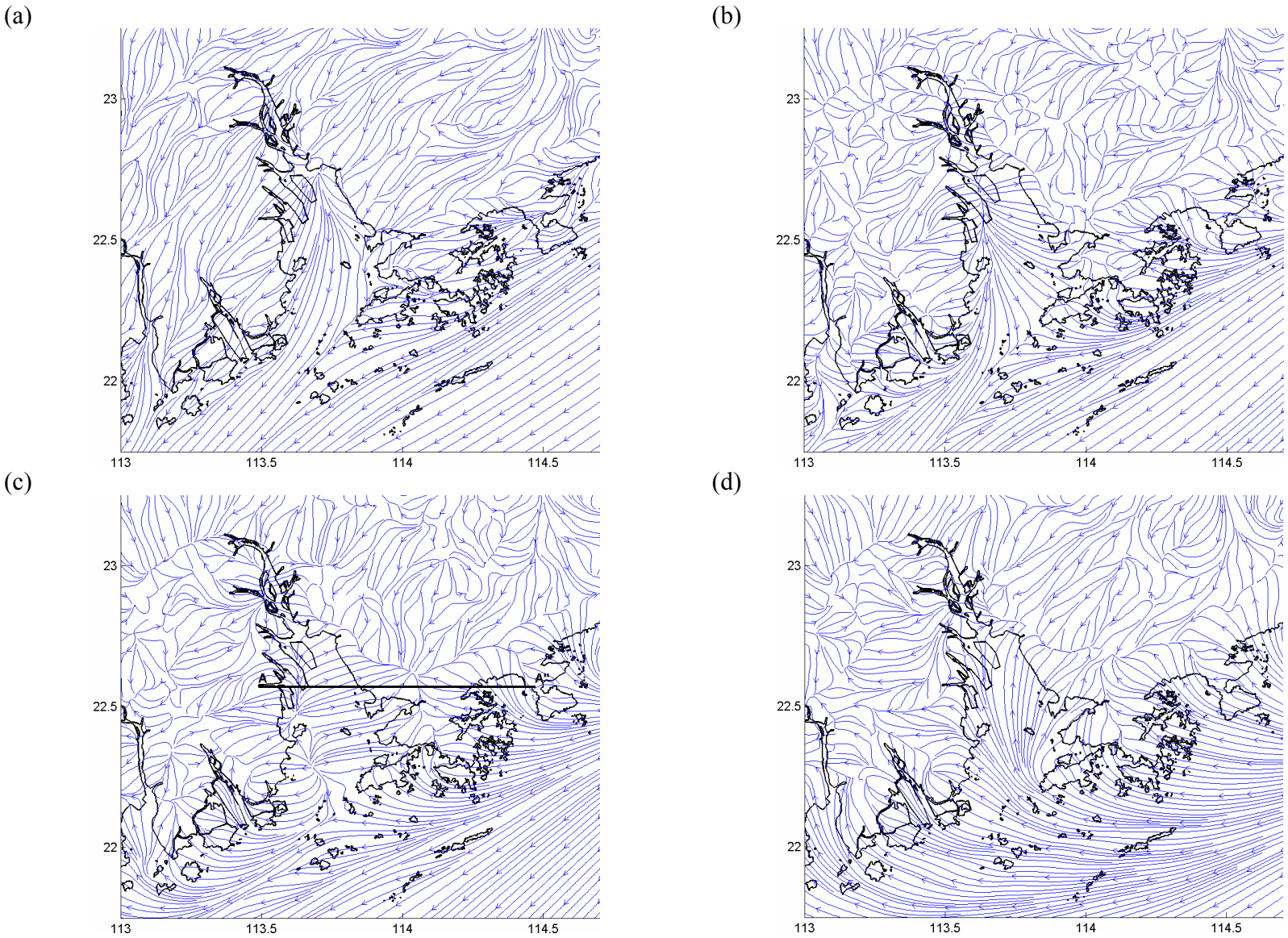

Figure 4-7: Spatial distribution of horizontal wind stream in D4 by URBAN-LSM at (a) 1000, (b) noon, (c) 1400 and (d) 1600 LST 31 October, 2003.

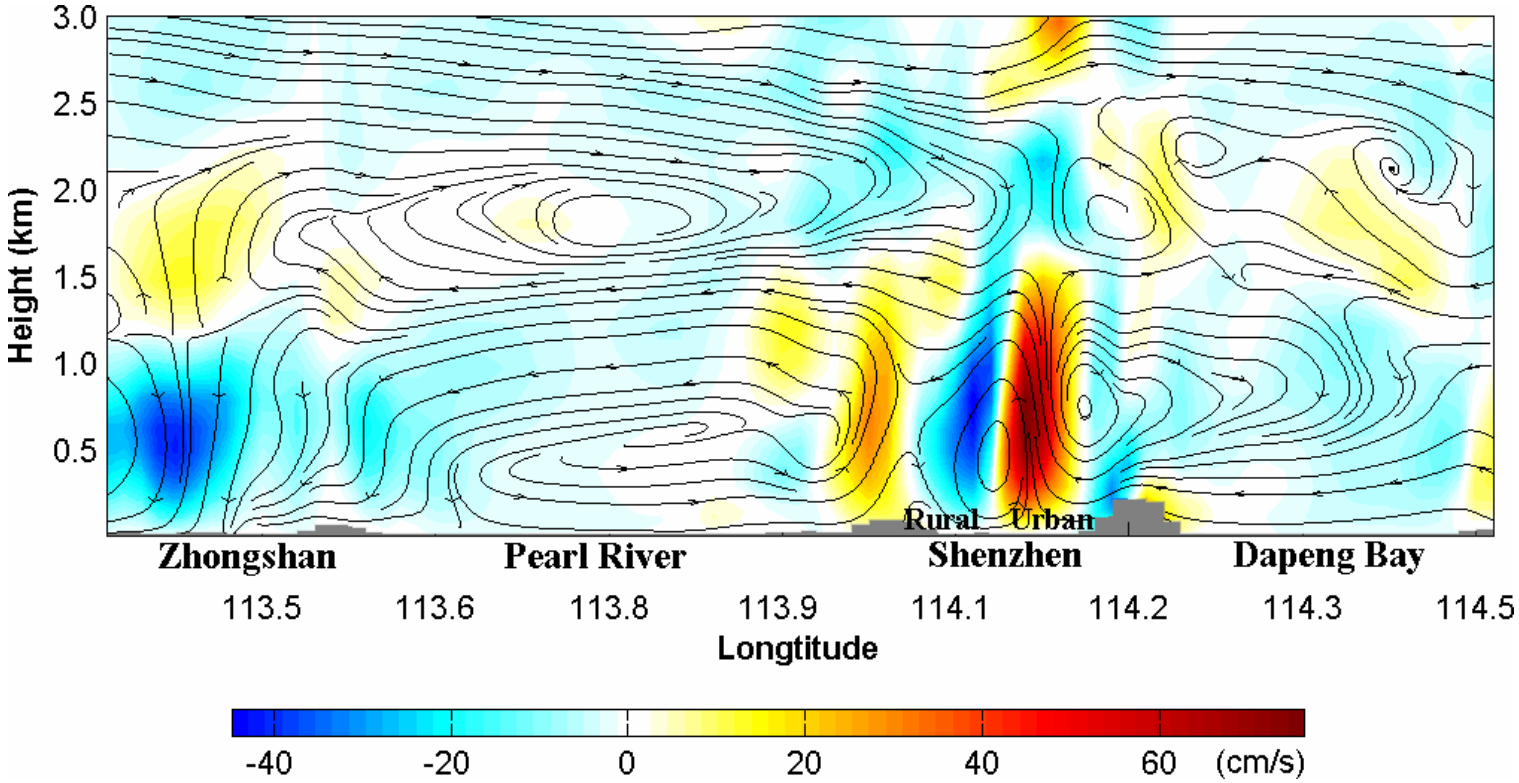

Figure 4-8: Vertical cross-section along the black line in Figure 4-7(c) by URBAN-LSM 30-hr forecast valid at 1400 LST 31 October, 2003, showing the wind stream, and the shaded background is the vertical velocity.

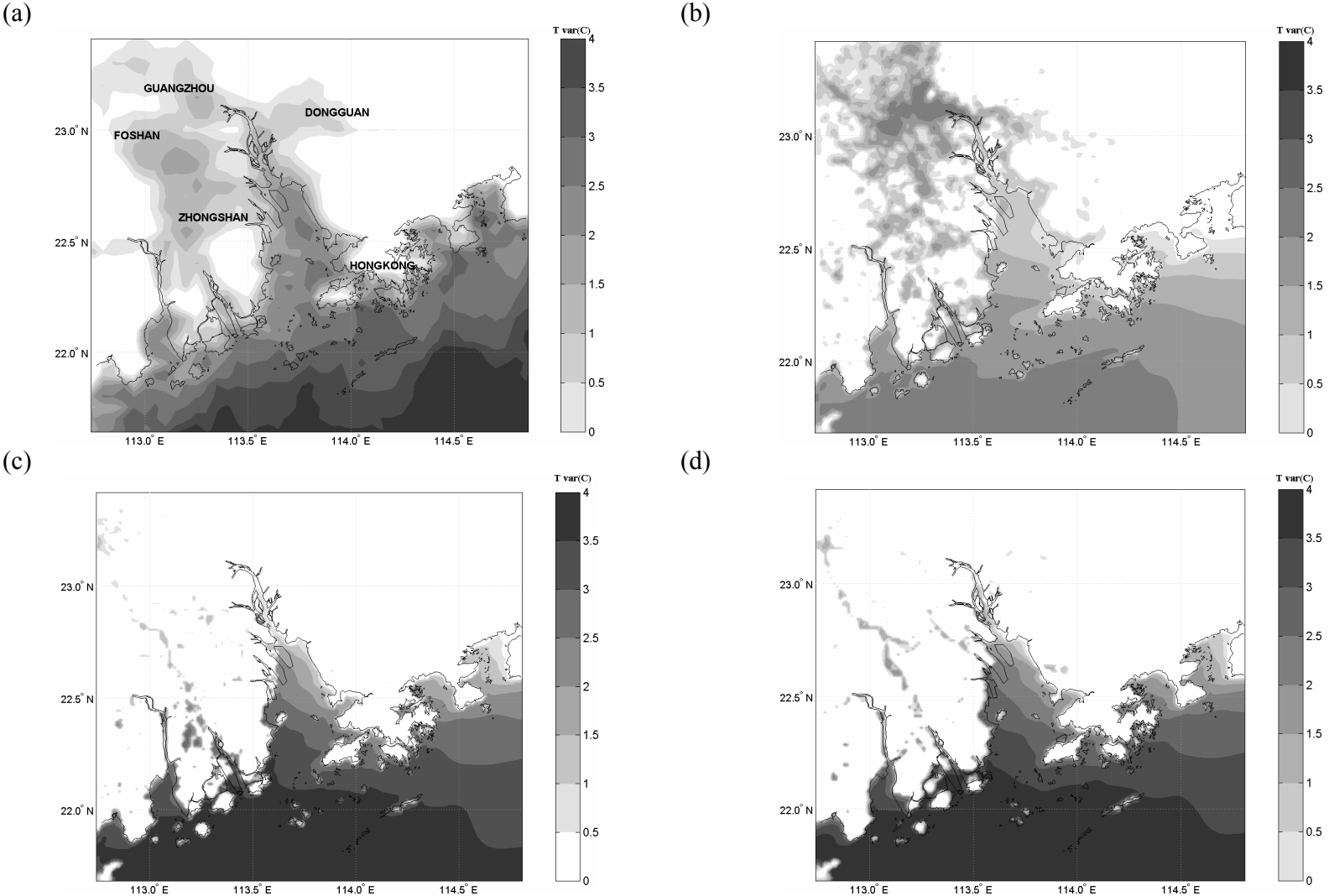

Figure 4-9: Spatial variance of surface temperature valid at 0200 LST 31 October, 2003 by (a) 5-km resolution MODIS, (b) simulation by URBAN-LSM, (c) SLAB-LANDU, and (d) SLAB. Shaded areas represent the positive variance, i.e. areas with higher temperature than domain-averaged.

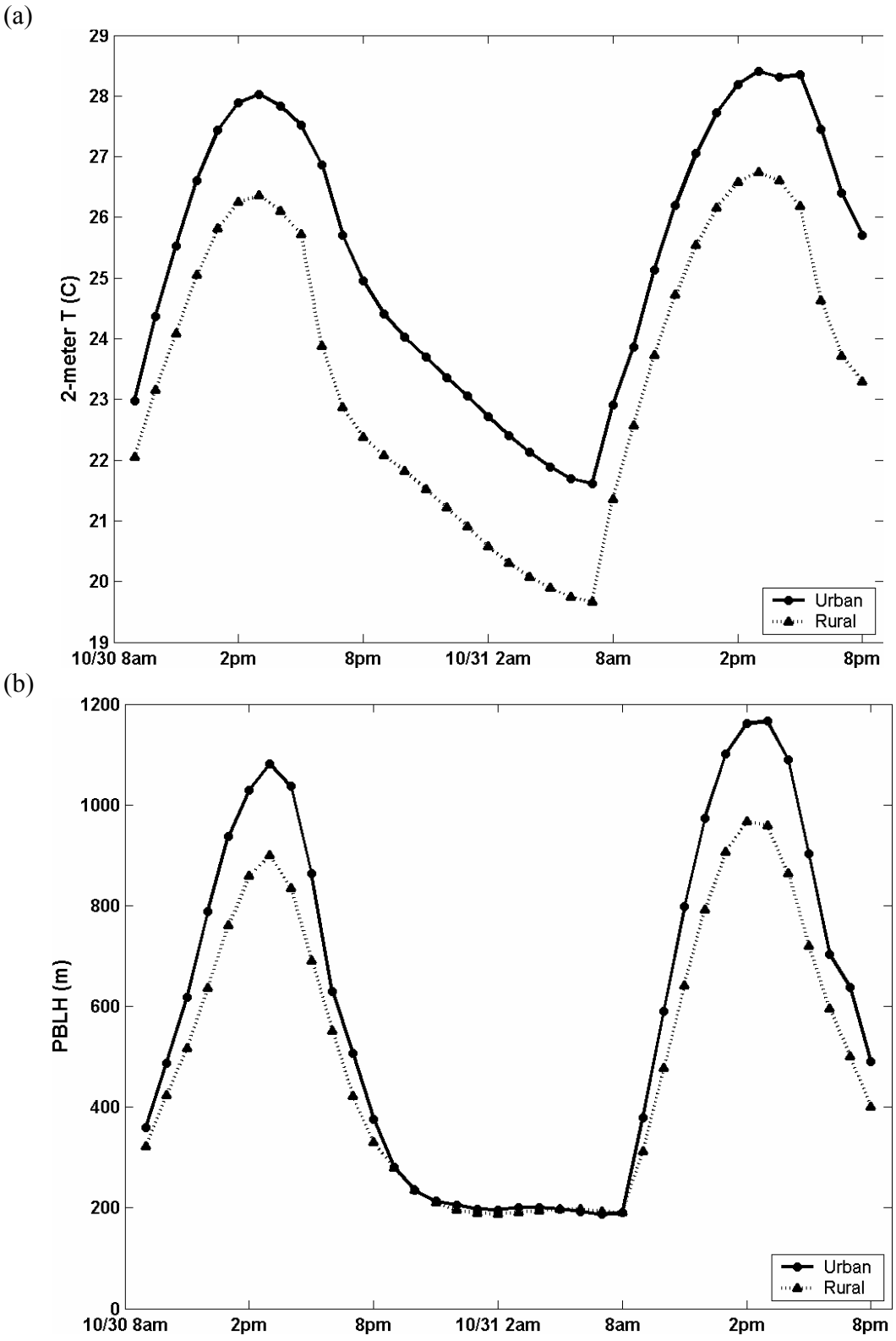

Figure 4-10: Time series of domain average over all land grids in D4 of (a) 2-meter temperature and (b) PBL height. Urban area (solid) and rural area (dotted).

(a)

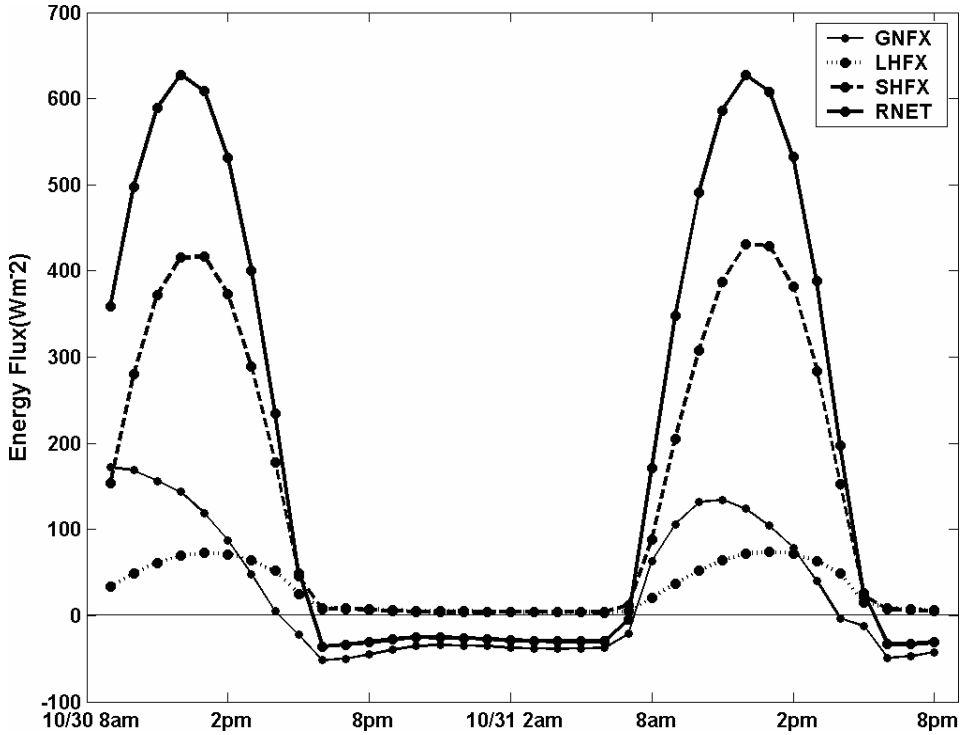

(b)

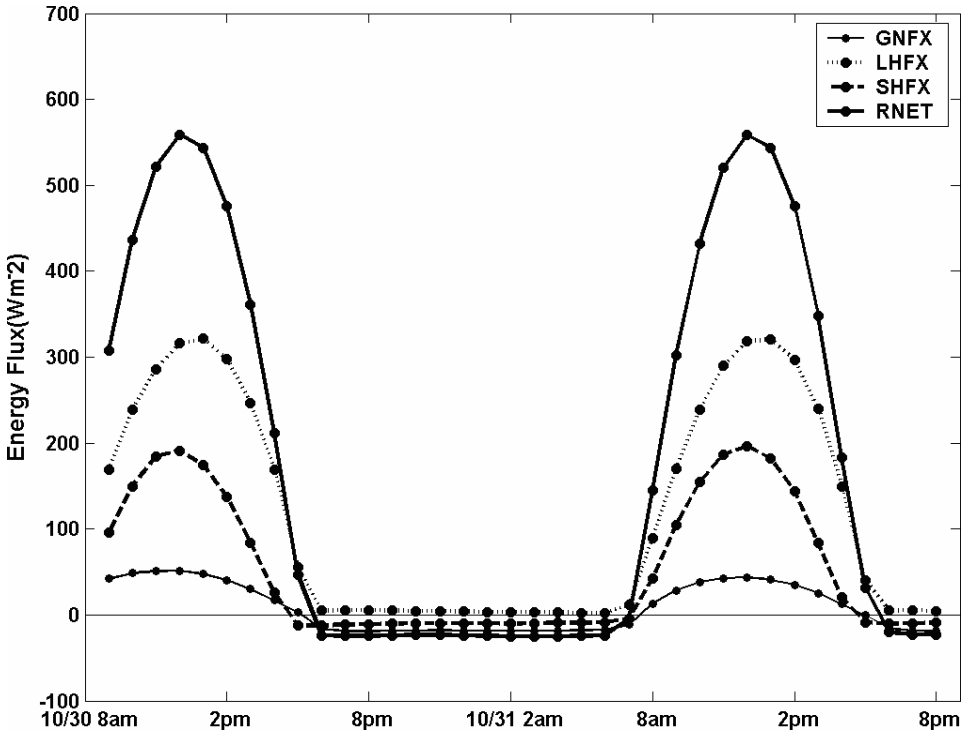

Figure 4-11: Surface energy budget of (a) urban areas and (b) rural areas. Ground heat flux (GNFX), latent heat flux (LHFX), sensible heat flux (SHFX) and net radiation (RNET).

(a)

(b)

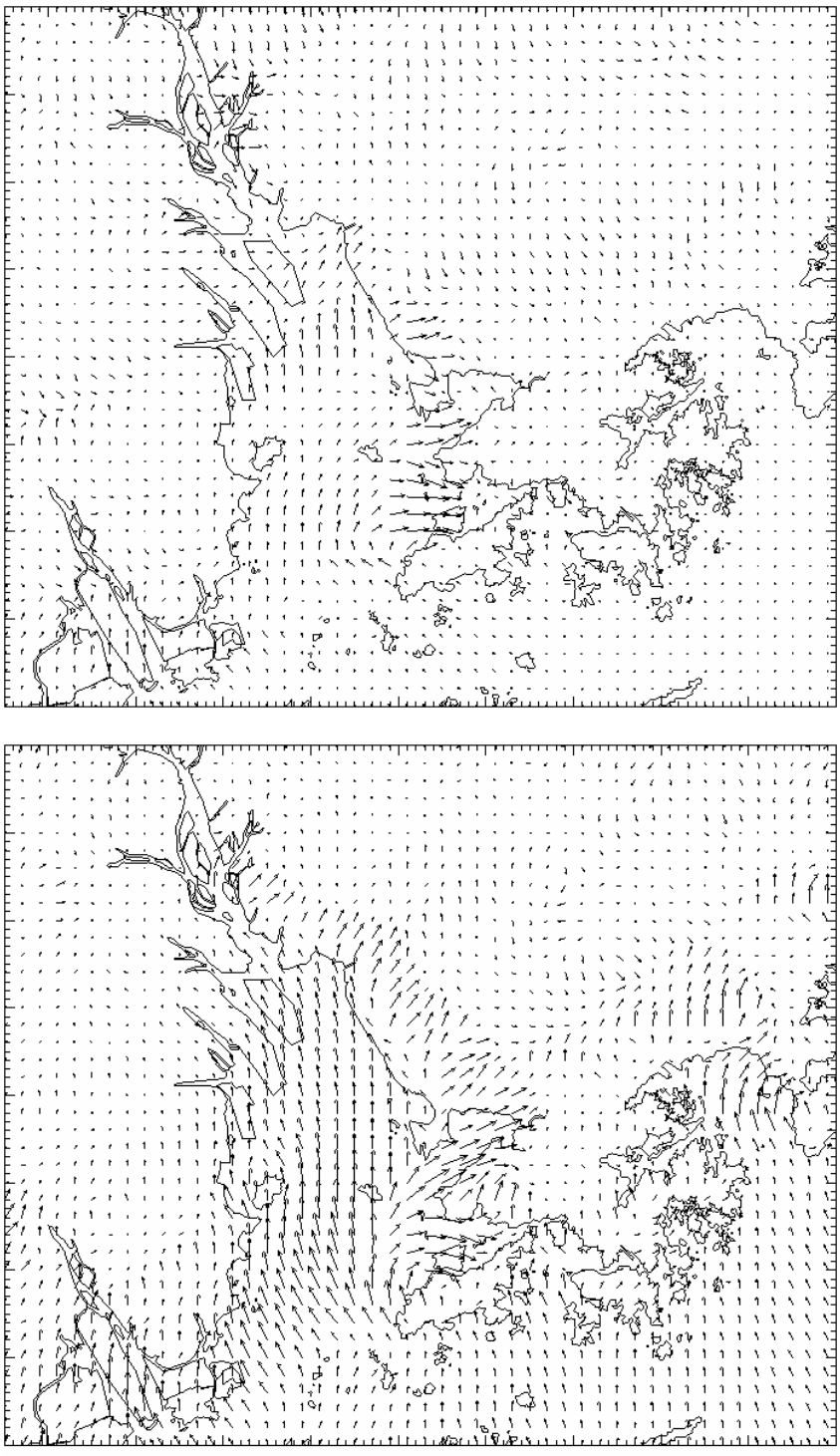

Figure 4-12: Difference of horizontal wind vector at 1400 LST 31 October, 2003 by (a) CONTROL – NO-URBAN and (b) ALL-URBAN – NO-URBAN.

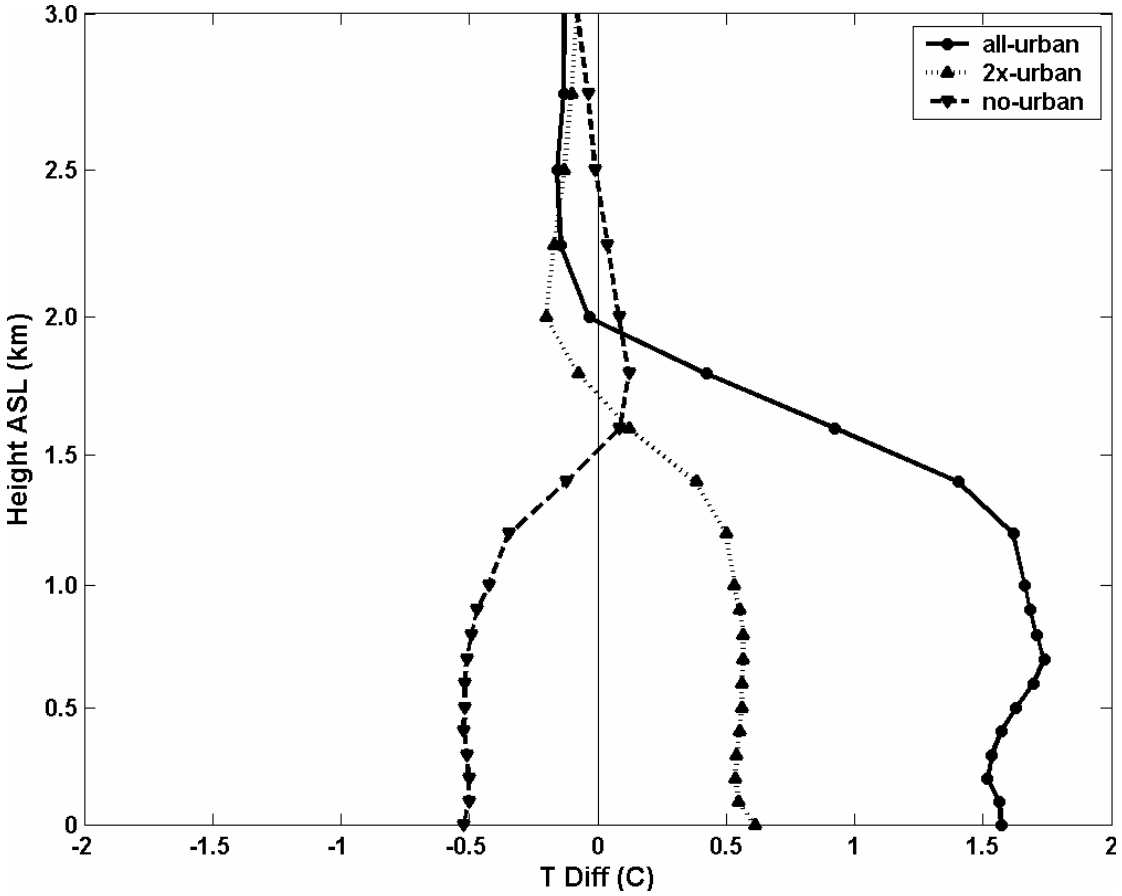

Figure 4-13: Profile of the temperature difference from CONTROL at 1400 LST 31 October, 2003.

Table 4-1: Contributions of the major vegetation classifications in the inner-most 1.5-km D4.

	USGS (%)	**HKPD (%)**
Urban	0.5	12.9
Cropland	45.6	22.7
Grassland	8.6	16.9
Forest	3.1	3.4
Water	42.0	42.1
Other	0.3	2.1

Table 4-2: Summary of the mapping strategy of the HKPD land-use legend to USGS 24-category and the corresponding green vegetation fraction.

HKPD classes	Description	USGS category	Green fraction
Irrigated cropland	Primarily paddy fields	Irr. Crop. Past.	0.8
Dry farmland	Farmlands, nurseries and vegetable gardens	Drylnd Crop. Past.	0.8
Orchards and plantations	Horticulture and floriculture	Drylnd Crop. Past.	0.8
Dyke ponds	Repeat pattern of fishponds and cultivated dykes	Wooded wetland	0.6
Forest	Dense tree covers	Evergrn. Broadlf.	0.95
Sparse woodlands	Sparse forest (< 30% cover) and shrubs	Shrubland	0.7
Dry grassland	Land covered by grasses or low shrubs	Grassland	0.8
Water body	Rivers, canals, lakes and reservoirs	Water Bodies	0
Mudflats	Tidal zones along the coast and river beds	Water Bodies	0
Fishponds	Water bodies for commercial fish farming	Water Bodies	0
Mangroves/swamps	Wetland including swamps and mangroves	Wooded wetland	0.6
Built-up areas	Urban and industrial	Urban	0.1
Construction/bare ground	Areas under construction or bare ground	Urban	0.1
Railways	Railway and associated features	Urban	0.1
Highways and roads	Highway and road network	Urban	0.1
Ports	Major sea or river ports	Urban	0.1
Airports	Civilian airports	Urban	0.1

Table 4-3: Physics options and land surface characteristics used in the experiments.

	Experiment		
	SLAB	**SLAB-LANDU**	**URBAN-LSM**
Cumulus Scheme	Grell Scheme for D1 and D2, None for D3 and D4		
Moisture scheme	Simple ice scheme		
PBL scheme	MRF scheme		
Radiation scheme	RRTM longwave scheme		
Land surface scheme	MM5 Slab	MM5 Slab	Noah LSM
Land-use dataset	24-category USGS	2003 HKPD	2003 HKPD

Table 4-4: Performance statistics for surface temperature of MM5 experiments in Hong Kong.

		Observation		URBAN-LSM		SLAB-LANDU		SLAB	
Station ID	Height	Mean	Std	ME	RMSE	ME	RMSE	ME	RMSE
MK	3	25.95	1.47	-1.23	1.45	-1.55	2.94	-1.81	2.95
SP	17	25.05	1.53	-0.75	1.18	-1.06	2.58	-1.36	2.66
HKA	8	24.92	1.46	0.01	0.66	-0.65	2.20	-1.93	2.21
TW	17	24.88	2.08	-0.80	1.21	-1.23	1.85	-2.14	2.60
KC	13	24.87	2.00	-0.44	1.00	-0.78	2.13	-1.93	2.53
YL	25	24.84	2.47	-0.13	1.12	-0.32	2.00	-1.64	2.36
TUN	69	24.51	1.36	0.02	1.14	-0.58	2.73	-1.77	2.38
ST	21	24.38	2.67	-0.56	1.34	-0.97	1.74	-2.14	2.65
TCA	21	24.29	2.53	-0.38	1.26	-0.07	0.99	-1.21	1.81
CW	18	24.22	1.26	-0.09	0.71	-0.14	1.79	-1.10	1.81
KT	25	24.10	1.08	-0.07	0.81	-0.09	2.45	-0.61	2.27
SEK	26	23.99	2.95	-0.69	1.24	-0.33	1.19	-1.73	2.07
SHA	16	23.97	1.82	0.14	0.64	0.00	1.36	-1.07	1.50
HKO	74	23.92	0.85	0.10	0.96	0.10	2.90	-0.06	2.09
CPH	136	23.91	1.65	0.29	0.77	-0.38	2.43	-1.20	1.81
SLW	71	23.90	2.79	-0.34	1.40	-0.06	1.02	-1.13	1.96
EPC	39	23.87	2.51	-1.12	1.62	-0.89	1.50	-1.84	2.47
LFS	50	23.74	2.17	0.36	0.86	0.39	1.72	-0.49	1.46
TKL	28	23.69	2.83	0.04	0.85	-1.24	1.60	-1.22	1.91
WGL	82	23.67	0.86	-0.34	0.74	0.00	0.63	-0.01	0.74
TAP	37	23.64	1.91	-0.32	1.32	0.08	1.08	-0.79	1.53
TPO	16	23.63	1.50	-0.14	0.45	-0.67	1.33	-1.03	1.39
TP	25	23.60	1.63	0.10	0.55	-0.31	1.65	-1.24	1.69
PLC	71	23.59	1.95	-1.16	1.42	-0.58	1.25	-1.11	1.86
CCH	99	23.56	1.82	-0.25	1.02	0.19	0.91	-0.34	1.27
KP	90	23.54	1.81	0.37	0.87	0.37	2.22	0.22	1.63
KAT	11	23.51	0.99	-0.67	1.07	-0.04	1.19	-0.37	1.23
SKG	31	23.48	1.27	-0.01	0.57	-0.64	1.23	-1.06	1.42
HKS	30	23.48	2.13	0.00	0.69	0.12	0.64	-0.78	1.13
JKB	52	22.89	1.99	0.08	1.14	0.22	1.29	-0.34	1.45
VP1	402	20.58	1.44	0.89	1.10	0.83	2.15	-0.50	1.47
TC	588	18.64	1.15	-0.03	1.17	0.89	2.00	0.04	1.42
TMS	969	17.07	1.62	0.10	0.87	0.17	1.44	-0.80	1.20
Average				-0.21	1.01	-0.28	1.70	-1.04	1.85

Table 4-5: Contributions of urban and cropland land-use in the inner-most 1.5-km D4 of the sensitivity experiments.

Experiment	Urban	Cropland
CONTROL	13%	23%
NO-URBAN	0%	36%
2X-URBAN	36%	0%
FULL-URBAN	58%	0%

Chapter 5 Role of Land-Sea Breeze Circulation Modified by Urbanization on Air Pollution in Pearl River Delta Region

Abstract

Recent satellite observations show that a layer of haze perpetually hangs over the Pearl River Delta (PRD) region and surface observations show numerous violations of the Hong Kong Air Quality Objective. This layer of haze mostly concentrated in the Pearl River estuary and a narrow (20 km wide) band along the shoreline, in particular during weak wind situations. While researchers suspect the land-sea breeze circulation "concentrates" or "traps" various pollutants in this region, the physical mechanism of the phenomenon has never been fully explained or quantified. In this chapter, a mesoscale atmospheric model (MM5) coupled with the Noah land surface model, which has bulk urban land-use treatments along with a detailed Pearl River Delta (PRD) urban land-use map, was used to simulate this land-sea breeze effect. The air mass/pollutant flowing pattern under this land-sea breeze circulation was studied by a three-dimensional particle trajectory model. By examining vertical streamline patterns and the pollutant-flow pattern, the impacts of this land-sea breeze circulation clearly suggest entrapment over this region. Our results also demonstrate how urbanization enhances the pollutant trapping and therefore contributes to the overall poor air quality in the region.

5.1 Introduction

The Pearl River is the largest river system in southern China. The river, approximately 2,200 km long, empties into the South China Sea through an extensive deltaic region to the west of Hong Kong. The Pearl River Delta (PRD) is broadly triangular in shape, extending down both sides of the Pearl River estuary with the city Guangzhou at its northern apex, the Special Economic Zone (SEZ) of Shenzhen at its southeast corner, and the Zhuhai SEZ at its southwest corner (see Figure 5-1). In a broad sense, Hong Kong and Macau occupy the other two angles of the delta. This region is conducive to the development of complex sea breeze interactions (Liu and Chan, 2002; Fung et al., 2005; Lam et al., 2006; Lo et al., 2006a). The PRD covers an area of about 41,700 km^2 and encompasses several major cities including Guangzhou, Shenzhen, Zhuhai, Donguan, Foshan, Zhongshan, Huizhou, Jiangmen and Zhaoqing. It is densely populated with about 50 million people, occupying 44.5% of Guangdong's total population, according to the 5^{th} national census in 2000 (Guangdong Provincial Bureau of Statistics, 2003).

The PRD is the engine of China's economic growth and has developed into the country's most important export base. In 2002, 36% of China's exports, worth US$ 118.5 billion, were produced in this region. Nationwide, the PRD ranked at or near the top in economic growth rates over the past two decades (double-digit growth per annum), mostly due to the accelerated integration into the global production network via Hong Kong. Recently the PRD has become an international manufacturing cluster, in higher value-added manufacturing, rather than in low value-added manufacturing, as in the past. Nevertheless, the PRD is not a uniform manufacturing powerhouse but rather a

constellation of discrete regions with different levels of development. Many PRD manufacturing industries, particularly the domestic market, are concentrated in the western region. The development of manufacturing industries has transformed the economic structure in the western PRD and has resulted in rapid urbanization. By 2000, the urbanization level reached 49.2% (Guangdong Provincial Bureau of Statistics, 2003). Predictions indicate that this level will increase in the next 20 years. Figure 5-2 shows the 1-km resolution land-use maps of the PRD in two different periods, one decade apart. The 2003 land-use map was compiled by the Planning Department of the Government of Hong Kong (HKPD) in 2003. The 1993 land-use map, from the U. S. Geological Survey (USGS), was based on 1992-1993 Advanced Very High Resolution Radiometer (AVHRR) data. Comparing both land-use maps, the 1993 USGS map shows more rural areas for the entire PRD region; however, by 2003 the region was transformed into a much more urbanized region. Also, the 2003 land-use map reflects more spatial variability than in 1993, indicating the development of new urban areas in different parts of the PRD.

Currently there is a trend for cities to integrate and merge for further prosperity, and within this context of rapid urbanization, the PRD is urbanizing rapidly in terms of population structure and land-use. Unfortunately, the increasingly large population with the increase in industrial activities and a higher density of motor vehicles has resulted in the air quality deteriorating substantially in the past two decades.

To mitigate the rapidly deteriorating air quality, an understanding of the local and regional circulation, including the complex interactions between the local land-sea breeze circulation (LSBC) and the urban environment in the PRD, is critical. While

researchers suspect the LSBC cell has a significant influence on air flow pattern and may affect the air quality in this region, the physical mechanism of the phenomenon has never been fully understood or quantified. In this chapter we investigate the structure of LSBC and its influence on the air pollutant transport characteristics over the PRD, with an objective of identifying salient aspects of regional air pollution meteorology. First, we used a non-hydrostatic, three-dimensional MM5 mesoscale model to study typical land-sea breeze events over the PRD region. Second, a three-dimensional particle trajectory model was used to understand the pollutant trapping and accumulation process by LSBC in the region. Third, sensitivity experiments were conducted for the two land-use maps to understand the effects of rapid urban growth on the pollutant transport. Finally, the effects of different background wind strengths on the LSBC structure were investigated. In Section 5.2 the numerical models used in this chapter are presented. Section 5.3 describes the pollutant trapping by the LSBC. In Section 5.4, sensitivity experiments using different land-use maps and background winds are examined.

5.2 Model Description and Numerical Setup

5.2.1 Meteorological Model and Configuration

Table 5-1 lists the domain configurations and physical parameterization schemes used in this chapter. In order to properly treat the complex topography and land-use of PRD, a 1-km-fine-resolution (mesh size, 300 x 300) domain covering Hong Kong and the PRD was used (see Figure 5-2). This 1-km domain was designed to resolve local and regional scale atmospheric circulation features over the PRD. Thirty-five full sigma-levels from surface to 100 hPa were used, of which the lowest twelve levels are below 1

km in order to have a finer resolution of the planetary boundary layer (PBL). The height of the lowest model layer corresponds to about 10 m above the ground.

The simple microphysical parameterization for cloud water, rain water and ice (Dudhia, 1993) and explicit convection were applied in the simulation domain. Short-wave radiation processes were handled using a cloud radiation scheme (Grell et al., 1994) and a Rapid Radiative Transfer Model (RRTM) (Mlawer et al., 1997) was applied for long-wave radiation processes. National Centers for Environment Prediction (NCEP)'s Medium-Range Forecast scheme (MRF) PBL scheme (Hong and Pan, 1996) was used in this investigation. The Noah land surface model (LSM) with a bulk urban land-use treatment was used for the land surface scheme (Chen and Dudhia, 2001; Liu et al., 2006). These physical parameterizations and urban land-use enhancements demonstrate the capability to capture major features of the observed urban heat island effect and sea breeze circulation patterns in the PRD region (Lo et al., 2006a).

To investigate the typical features of the local and regional scale atmospheric circulations and isolate them from other complexities of the real atmosphere, idealized meteorological initial and boundary conditions (ICBC) were ingested into the MM5 simulations. In the present setup, the MM5 runs were initialized using the 1° x 1° NCEP Final Analysis (FNL) data as first guess fields. The lateral boundary conditions were obtained by linearly interpolating 6-hourly FNL data. The idealized ICBC were created by averaging the domain sea level pressure and geopotential height at each upper level, to provide a stationary synoptic condition. The horizontal winds (u and v) profile are specified by 0 m s^{-1} , 3 m s^{-1} and 6 m s^{-1}, constant with height, in order to investigate the effect of different background wind strengths on the local atmospheric circulation. In other words, simulated atmospheric circulations are mainly driven by local thermal

effects and background winds. The simulation period is 0200 LST 31 October 2003 to 0800 LST 1 November 2003, with the first six hours used as the spin-up, to investigate the formation of meteorological condition conducive to the 1-3 November 2003 record high air-pollution episode. The weather during the simulation period was generally calm and fair over southern China and the PRD. This stationary synoptic weather is favorable for the development of LSBC and urban heat island circulation (UHIC).

5.2.2 Particle Trajectory Model (PTM)

A particle trajectory model (PTM), coupled with MM5, was used to investigate the air-flow pattern driven by the local atmospheric circulation in PRD. The prognostic model MM5 is used to predict meteorological condition and advection, which are used to drive the PTM where individual fluid particles are transported according to the wind fields provided by MM5. Pollutant trajectory in the PTM is simulated by tracking a large set of particles. Subsequent positions of each particle which represent a discrete element of pollutant mass at time $t + \Delta t$, are computed from the following equation:

$$x_i(t+\Delta t) = x_i(t) + u_i \Delta t \tag{5-1}$$

where i = 1,2 or 3 for the x, y, and z component. The wind velocity $u_i(x_i,t)$ were obtained directly from the meteorological model MM5 (Fung et al., 2005). A time step Δt = 5s is chosen to resolve fine flow field. Since the grid-scale meteorological variables are defined only on the 1-km MM5 model gridmesh, a linear interpolation scheme (both in time and in space) is used to estimate their values at each particle location. Continuous equal spacing 4 x 4 emission sources were chosen (see Figure 5-3 for their exact locations) to release particle tracers, in order to identify the locations of pollution

sources which occur in different regions over the PRD. The particle tracers were released at the same height at 100 m AGL with the same emission rate of one particle per ten seconds.

5.3 Pollutant Trapping Mechanism in PRD

5.3.1 The Pearl River Delta Circulation Zone (PRDCZ)

In the coastal regions, it is obvious that the pollutant transport characteristics are strongly influenced by LSBC features. Therefore, before going through the pollutant flow pattern using the particle trajectory model, we will first examine the LSBC features in the PRD.

In this simulation, no background winds were ingested into the MM5 ICBC. This case represents an extreme situation of stationary synoptic weather, and local circulations were solely driven by the local thermal effects. The simulated surface streamlines (10 m AGL) and surface temperature (2 m AGL) variances at selected times are displayed in Figure 5-4, showing the development features of the sea breeze circulation (SBC) over the PRD region. The spatial variation of temperature anomalies, defined as differences between the grid-point and domain-average surface temperature was computed. From the MM5 simulations, without the influence of the synoptic forcing, the local circulations were dominated by thermally induced winds (LSBC and Urban Heat Island Circulation (UHIC)). At 1000 LST (Figure 5-4a), while the land surface was still cooler than the ocean, land breeze was dominant over most of the coastal regions. At the same time, in the region near Guangzhou (23.1°N, 113.2°E), where there is a large urban area extension, the UHI effect caused relatively higher temperature than in

the surrounding regions. This high temperature UHI generated a convergence zone near Guangzhou in the early morning. At noon (Figure 5-4b), the SBC started to develop and the prevailing winds switched to landward in most coastal areas. Obvious circulation zones were developed at 10-20 km away from the coastal line. The temperature of urban areas seemed to not be noticeably higher than the surrounding areas; hence the convergence zone near Guangzhou disappeared. The SBC further strengthened at 1400 (Figure 5-4c). The horizontal extension of the SBC can extend to ~30 km and can almost penetrate into half of the Hong Kong territory. Note that when the SBC is prominent, there is a huge circulation zone over the Pearl River Estuary, which we called the PRD circulation zone (PRDCZ), see Figure 5-4d. Since most urban and industrial areas are located along two sides of this circulation zone, the structure of this zone is very crucial to the pollution dispersion in the PRD. At 1600 (Figure 5-4d), the regional SBC along the South China Sea was fully developed and the circulation zones extended to 40-50 km away from the coastal of the South China Sea.

Because of the lack of solar heating, during the night the atmosphere becomes more stable and less convective. Because the land surface is generally cooler than the ocean, the sea breeze disappears and the land breeze is dominant in the region. However, as a result of urbanization, the UHI is usually more significant at night and the flow field in the PRD becomes more complex, rather than a simple land-breeze circulation. At around midnight in the PRD there were two inland hot spots located at the highly urbanized regions near Guangzhou (23.1°N, 113.2°E) and Dongguan (23.0°N, 113.8°E) which caused some convergence zones (see Figure 5-5). These convergence zones have

a strong impact on pollutant trapping and this phenomenon will be discussed in Section 5.3.2.

In order to examine the vertical structure of the flow pattern, two vertical cross-sections of streamlines across the PRDCZ at 1400 LST are shown in Figure 5-6. One is projected on west-east plane along the longitude from 112.4°E to 114.8°E, and the other is on the south-north plane along the latitude from 21.1°N to 22.7°N. In Figure 5-6a, the afternoon SBC were well-developed, i.e., closed circulation cells were found along the coastal region of the Pearl River. Over the eastern coastal region, sea breezes were generated within the lower part of the boundary layer, 1 km above the surface across the Pearl River, while returning winds were dominated from 1 km to 2 km. A similar circulation cell is found over the western coastal region. It is interesting to see that the bi-center of these two circulation cells was not located in the center of the Pearl River, but rather shifted to the western coast. In addition, the horizontal dimension of the eastern SBC cell is relatively larger than that on the western coast, indicating that the eastern circulation cell is relatively stronger. One of the reasons is because the larger urban areas extended to the eastern coast (see the 2003 land-use map in Figure 5-2) and the corresponding UHI caused a stronger SBC.

One geographical characteristic of the PRD is the delta-shaped coast. This particular feature increases the complexity of the afternoon SBC structure. As can be seen from Figure 5-6b, circulation cells not only occurred along the two sides of the Pearl River, but also occurred along the apex of Pearl River estuary.

5.3.2 Pollutant Transport Characteristics

The last section illustrated the general features of LSBC in the PRD under an idealized stationary synoptic forcing. In this section, we utilize the particle trajectory model (PTM) to investigate the pollutant dispersion in that situation. Passive and non-reactive particle tracers were released at regular intervals at a rate of 1:10 seconds from 16 sources (see Figure 5-3 for the locations) at 100 m AGL, in order to identify the locations of pollution sources. A 5-day simulation was conducted by the PTM and the 24-hour MM5 simulated winds were repeatedly used to drive the PTM during the simulation period.

5.3.2.1 Pollutant-flow Patterns

Three plumes (sources G, F, and J) located around the PRDCZ were selected to demonstrate the pollutant transport characteristics. Figure 5-7 presents features of the particle-flow patterns. The positions of particles at selected times were projected onto three planes: one horizontal and two vertical cross-sections.

In Figure 5-7a, at 1500 LST of the first day simulation, while the afternoon SBC is dominant over the PRD, tracers were trapped by the closed SBC. The tracers released at 100 m AGL can be brought to 2 km by the SBC. The horizontal extension of the SBC was about 20 to 30 km. At midnight 0300 (Figure 5-7b), the atmosphere became less convective and the closed SBC disappeared. Pollutants were transported toward the ocean by the land breeze. Meanwhile, as we discussed in Section 5.3.1, because of the UHI and corresponding convergence zone, larger amount of tracers were stagnated in the region around Guangzhou (see Figure 5-7b(i)). On the third afternoon (Figure 5-7c), since there was no strong synoptic wind to clean the pollutants away from the simulation

domain, the situation became much worse. Pollutants were transported back to the coast and were well-mixed within the PBL by the SBC. From Figure 5-7d, we can clearly see that the dispersion tend to spread toward the southeast. The regional LSBC, between the land and South China Sea, is responsible for this phenomenon.

5.3.2.2 The Two Transport Regimes

The time series contributions of the 16 sources to the sampling zones are shown in Figure 5-8, and locations of the sampling zones can be seen in Figure 5-3. There was a diurnal cycle of pollutants in each zone, which are classified in two main regimes:

One regime can be applied to the zones along the two sides of the Pearl River (z1 to z3, and z7 to z9). During daytime, when the sea breeze was dominant, pollutants were trapped and well-mixed within the PBL by the SBC, and the particle amounts increased over the two sides of the Pearl River. The situation improved after sunset, when the land breeze was dominant and the pollutants were carried away from the zones. The timing and duration of this cleanup process seems to be related to the degree of urbanization, as we can see in z3 and z9, which represents the highly urbanized Guangzhou and Dongguan regions respectively. The cleanup process started at midnight, which is relatively late and the duration is much shorter than the other zones (z1 and z2), which are not as urbanized. Further discussions on the urbanization effect on the pollution transport can be found in Section 5.4.1.

The other category can be applied to the region over the PRDCZ (zones z4 to z6) where the diurnal cycle of pollutants was totally reversed. In the PRDCZ, the sea breeze during the daytime generally helped to clean away the pollutants while the pollutants, were accumulated by the land breeze.

Figure 5-8 also illustrates the accumulation tendency of pollutants. Without strong winds, pollutants released over the PRD are trapped by LSBC and well-mixed within the PBL over time. The highest accumulation of pollutants is in z3 (Guangzhou), followed by z8 (Shenzhen) and z7 (Hong Kong). Note that a large proportion of pollutants emitted in the western coastal region were transported to the eastern PRD (z7 and z8). However, it seems to be more difficult for pollutants emitted in the eastern region to be transported to the western region in this situation.

5.3.3 Conceptual Model of Pollutant Trapping

In the previous section, we have seen the possibility of pollutant trapping by the SBC. In this section, we describe the process of pollutant trapping by the SBC within the PRDCZ. Figure 5-9 shows the schematic picture. Power plants, factories and vehicles all release pollutants into the air near the ground along the two sides of the Pearl River. During daytime, the sun heats up the ground and cause the polluted air to rise. The upper-level returning flows of land breeze pushes the polluted air toward the PRDCZ, where pollution from both sides of the border meet and mix. The polluted air cools quickly over the water and sinks to near the surface, where it disperses around the region and returns to the coastal zones by sea breezes. This cycle restarts again causing pollutant trapping and accumulation. Without a strong wind to blow them away, the pollution level can build up significantly over time.

At night, the land breeze generally helps to clear pollutants away from the urban cites. However, because of the UHI effect, similar convergence zones can occur over the urban areas causing nocturnal pollutant trapping. Detail discussions on the urbanization effect on pollutant trapping can be found in next section.

5.4 Sensitivity Studies

The urbanization effect on meteorological conditions, highlighted in the work of Lo et al. (2005), suggests that the SBC can be strengthened by urban sprawl in PRD. In this section, we utilize the coupled MM5/PTM to conduct several experiments by changing the domain land-use to examine the urbanization effect on the pollutant dispersion in PRD. In addition, the effects of different background winds on the pollutant transport have also been investigated.

Table 5-2 summarizes the configuration of the four sensitivity experiments. The land-use maps of the PRD in two different periods (see Figure 5-2) with a combination of three different wind profiles were examined. The PRD is located in the sub-tropical zone; the surface prevailing winds are affected by the northeasterly trade-wind belt most of the time. According to the wind statistics reported by Hong Kong Observatory (Wong and Kwan, 2002), between 1990 and 2000, the probability of prevailing easterly to northeasterly surface winds was about 65%, with an average wind speed of 6 m s^{-1} at Waglan Island, the station generally accepted as representing background wind data for Hong Kong. Therefore, in the sensitivity experiments, one wind profile was set as zero wind speed, representing an extreme situation of total stationary weather. The second wind profile was configured as 3 m s^{-1} easterly wind within the PBL (below 1.5 km AGL) and 3 m s^{-1} westerly wind above the PBL (1.5 km AGL), represented a typical weak wind situation. The third wind profile represented a normal day situation, with 6 m s^{-1} northeasterly wind at the surface and 6 m s^{-1} westerly wind above the PBL (1.5 km AGL).

In the first sensitivity test, the up-to-date HKPD land-use map in the CONTROL experiment was replaced by the USGS land-use map. In the second and third sensitivity test, the weak background wind profile was applied, and the two land-use maps were used to conduct MM5 simulations respectively. In the fourth sensitivity test, the 6 m s^{-1} wind profile was applied, in order to see the pollutant trapping in a normal day situation. All four experiments were conducted using identical MM5 configurations, physics schemes, and emission sources as the CONTROL experiment; only the land-use maps and the ICBC of winds were different.

5.4.1 Effect of Urbanization on Pollutant Transport

The particle-flow patterns of the selected three sources (source G, F, and J in Figure 5-3) located around the PRDCZ of the experiment, without background winds and using the USGS land-use map (referred to as USGS-0), are shown in Figure 5-10. Comparing the particle-flow patterns of CONTROL (Figure 5-7) with the new 2003 HKPD land-use map to the one with USGS-0 (Figure 5-10), pollutant trapping and accumulation was generally more severe in the CONTROL. In the afternoon of the first day simulation, Figure 5-7a(ii), compared to Figure 5-10a(ii) has larger extension of the pollutant trapping zones both in horizontal and vertical directions. It appeared that urbanization caused a stronger temperature gradient between land and sea, creating a stronger SBC and therefore a stronger pollutant-trapping zone was generated. These stronger pollutant trapping zones were more noticeable in the afternoon of the third day simulation, by comparing the cross-section projections of Figure 5-7(c) and Figure 5-10(c). This comparison implies that urbanization can enhance daytime pollution trapping,

re-circulation and mixing in PRD. During the nighttime, the UHI caused the atmosphere in CONTROL to be more convective than the USGS-0.

The time series of contributions of the 16 sources to the sampling zones of the experiment USGS-0 are summarized in Figure 5-11 and the locations of the sampling zones can be seen in Figure 5-3. We took sampling zone z3, near Guangzhou, as an example to demonstrate the urbanization effect on pollutant transport. In Figure 5-11, the amount of pollutants in this zone has an obvious diurnal cycle: pollutants started accumulating at noon when the SBC was dominant, while the amount of pollutants dropped after the sunset (1800 LST) during the land breeze period. This was the situation when this particular zone was still a rural area. From the 2003 land-use map, this zone is currently a highly urbanized region, while it is a small city according to the USGS land-use map in 1993.

Recall that Figure 5-8 (z3) demonstrated the current situation of this zone. Because of the effect of urbanization, the accumulation of pollutants is generally higher than what would occur in a rural area (Figure 5-11, z3). The diurnal cycle experienced two changes: 1) pollutants start accumulating at 1000, about 2 hours earlier than USGS-0 and 2) the amount of pollutants does not drop immediately after sunset, but delays a few hours before midnight.

This result implies that urbanization can induce or enhance early morning and nocturnal pollution trapping in the PRD. Because of urbanization, low evaporation and high heat conductivity of buildings in urban areas causes the region to warm much faster than the surrounding rural regions (see Figure 5-4a). This higher temperature generated a convergence zone and which caused pollutants to accumulate in the early morning hours.

During nighttime, the surface temperature in urban areas does not drop as much as in the rural areas. Surface temperatures over an urban area are comparable to the sea, or even higher than the SST (see Figure 5-5). Therefore, a weaker land breeze, or even a UHIC convergence zone was created over urban areas. These conditions are not favorable for pollutant dispersion.

In order to quantify the pollution level over the PRD in different situations of the sensitivity tests, we used a quantity called the Pollutant Trapping Index (PTI). PTI is the ratio of the total amount of pollutants from the 16 sources accumulated in the 9 sampling zones in a particular case to that in the CONTROL during the 5-day simulation. Table 5-2 lists the PTI of each sensitivity test. The difference of 0.17 in PTI between the CONTROL and USGS-0, indicates there is a 17% difference in the amount of pollutant accumulation in the PRD between the two situations.

5.4.2 Effect of Background Wind Strength on Pollutant Transport

The particle-flow patterns of the three sources using the 2003 land-use map under a weak 3 m s^{-1} background wind (refereed to as HKPD-3) is presented in Figure 5-12, and the corresponding time series of contributions of the 16 sources to the sampling zones is displayed in Figure 5-13. Comparing this to the particle-flow pattern with CONTROL (Figure 5-7), the background wind generally helps pollutant dispersion with PTI drops to 0.7. However, this weak wind profile was not able to destroy the afternoon SBC completely. Pollutants released around the PRDCZ were still trapped by the SBC cells, as shown in the cross-sections in Figure 5-12a and c.

When applying this weak wind profile with the USGS land-use map (USGS-3), the amount of pollutants (Figure 5-14) was much reduced (PTI 0.54) over the entire PRD. The SBC was weakened by the background wind, and daytime pollutant trapping were not severe in this case. The urbanization effect gives further explanation of the increasing pollution episodes in the PRD in recent years. It is clear that urban sprawl strengthens the SBC, and this strong SBC would need a stronger synoptic wind to destroy it. However, the frequency of a strong wind situation does not change much over time. With the same weak wind frequency, the probability of pollutant trapping is much higher in the current PRD than two decades ago. Therefore, the rapid urbanization not only increases the pollution emission sources, but also affects meteorological conditions that enhance the chances of high-pollution episodes.

Figures 5-15 and 5-16 present the situation on a normal-day with 6 m s^{-1} wind speed (HKPD-6). In Figure 5-15a, the sharp of the SBC was strongly influenced by the background wind. The SBC cells were not well developed compared to the CONTROL over the PRDCZ. However, these 6 m s^{-1} winds could not completely destroy the afternoon SBC, since a small account of pollutants were trapped, causing a daily maximum amount of pollutant in the zones beside the PRDCZ during the afternoon (Figure 5-16). During the night, pollutants followed the background wind and were transported out of the domain. In this situation, daily pollutant accumulation was not found and the PTI was only 0.34.

5.5 Conclusions

Using a state-of-the-art meteorological model (MM5), coupled with a three-dimensional particle trajectory model, the pollutant transport mechanisms affected by

the local and regional atmospheric circulations over the PRD was studied. The temporal and spatial variations of the land-sea breeze circulation interacting with an urban heat island circulation were simulated by the MM5. Numerical experiments were conducted to explore the structure and the trapping mechanism over the Pearl River Delta Circulation Zone.

The dispersion of passive and non-reactive pollutants was simulated by the particle trajectory model. Results suggested that pollutants emitted in the cities besides the Pearl River Delta Circulation Zone were trapped by the sea breeze circulation and well-mixed within the planetary boundary layer. The research showed that the amount of pollutants accumulated when the sea breeze is dominant over the coastal zone and the land breeze generally helps to clean the pollutants away from the coastal cities.

The urbanization effects on the pollutant transport also have been examined. Urban sprawl hinders air pollution dispersion in the Pearl River Delta. In the afternoon, urbanization strengthens the sea breeze circulation and more pollutants are trapped and brought to coastal zones. During the night and early morning, an urban heat island effect weakens the land breeze and creates circulation convergence zones causing the nocturnal pollutants trapping and early morning pollutants to accumulate. With the same weak wind speed frequency, the probability of pollutant trapping in the current PRD is much higher than two decades ago.

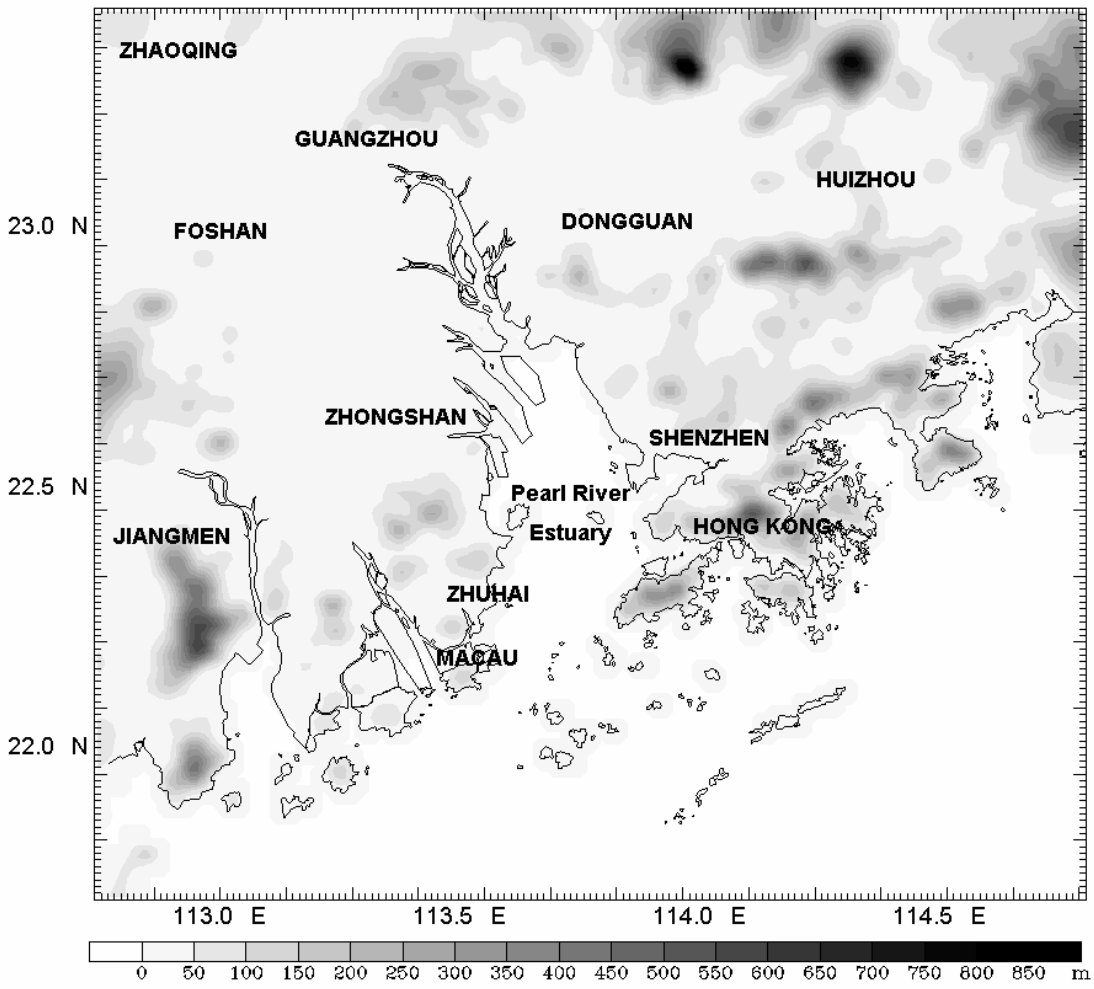

Figure 5-1: Topography map and locations of major cities in Pearl River Delta region. Contours represent the terrain height, contour interval is 50 m.

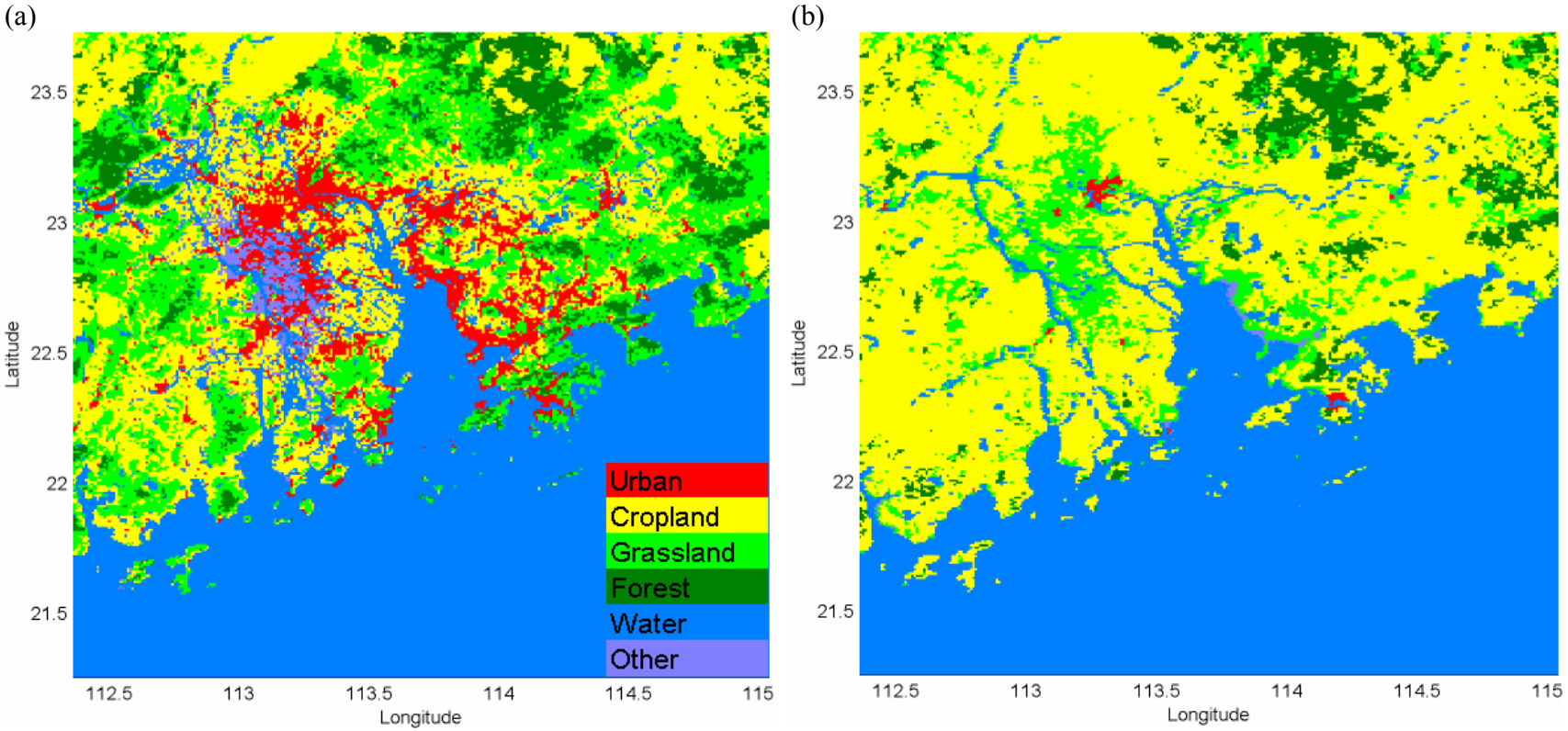

Figure 5-2: Land-use map over PRD region shown on the 1-km MM5 domain. (a) 2003 land-use obtained from HKPD. (b) 1993 land-use based on the 24-category USGS dataset. The colors indicate urban, cropland, grassland, forest, water and other according to the figure legend.

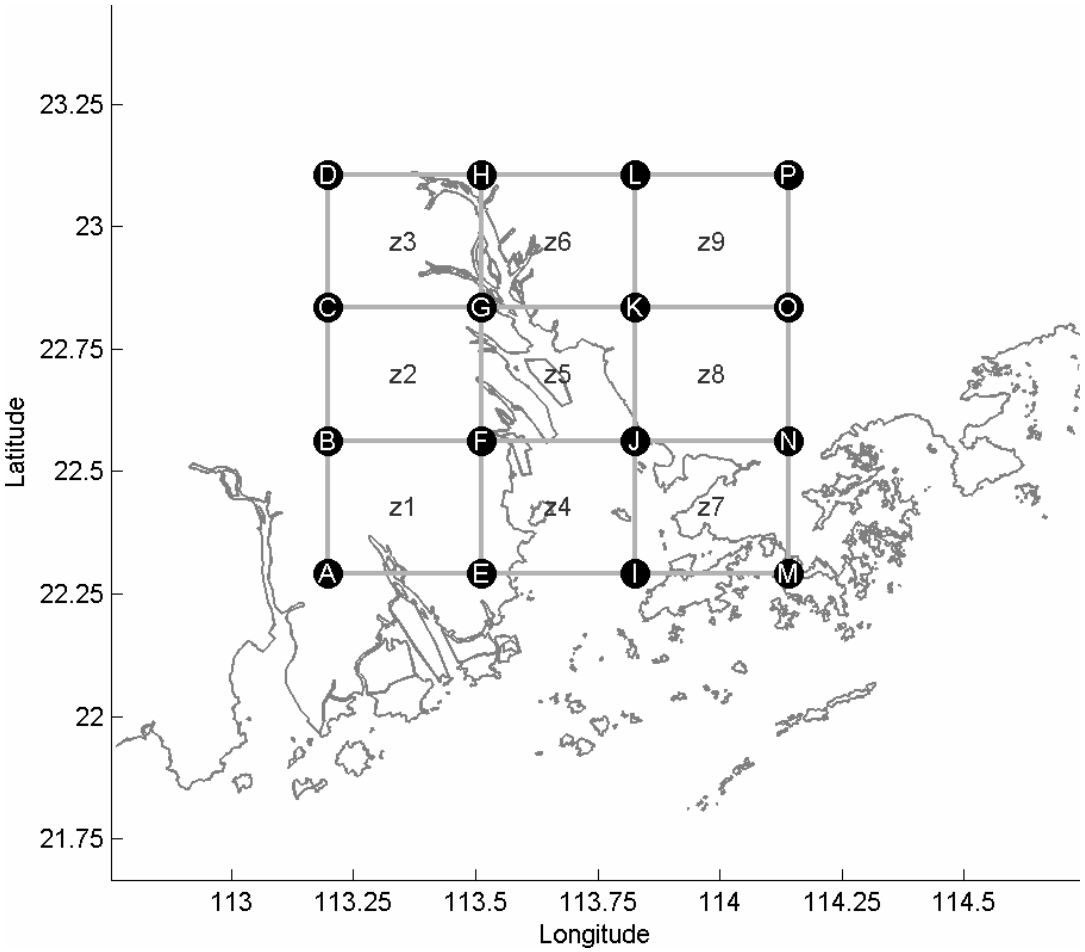

Figure 5-3: Map showing locations of the 4 x 4 emission sources (solid dots A-P) and extension of the 3 x 3 sampling zones (grey boxes z1 to z9).

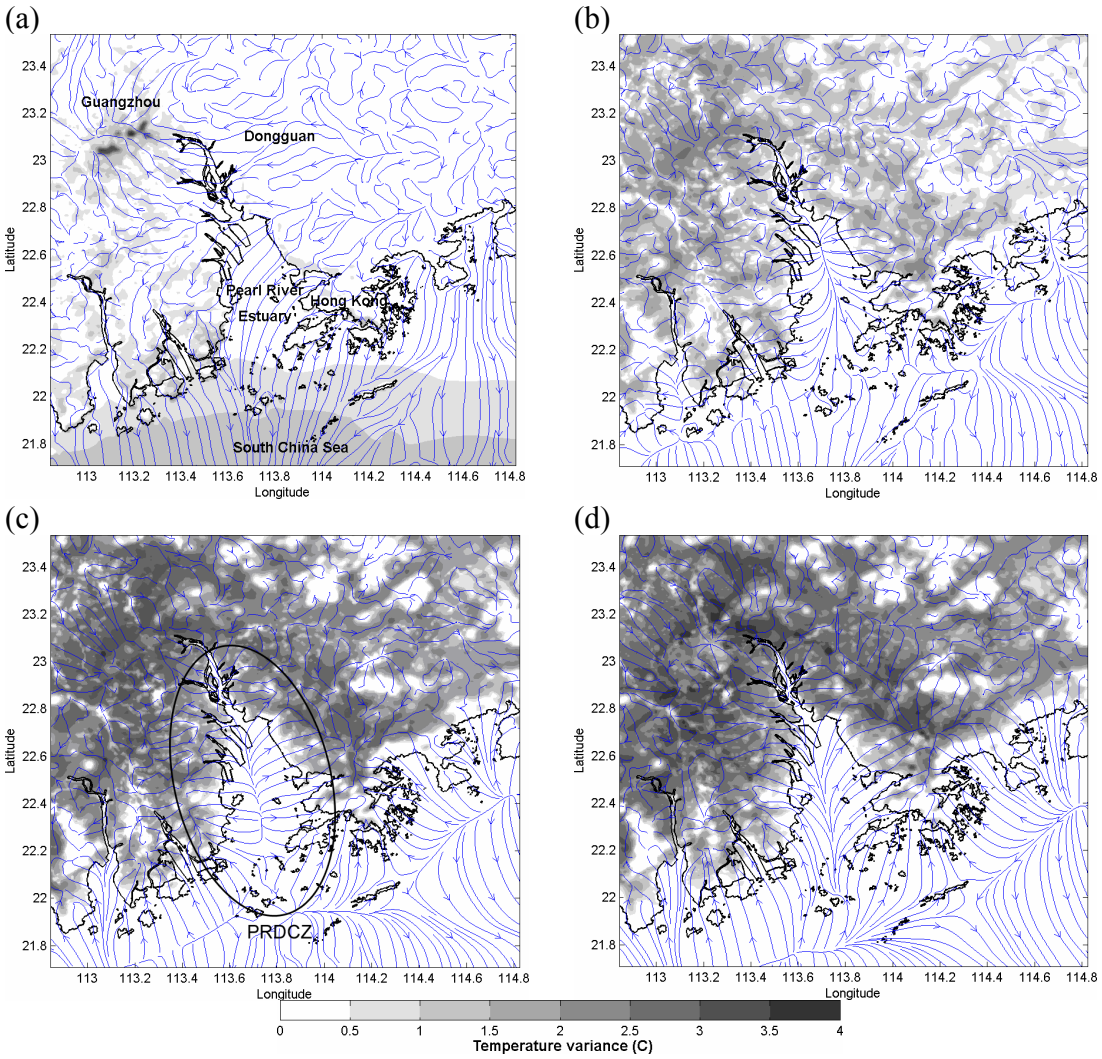

Figure 5-4: Horizontal distribution of surface streamlines (a) at 1000, (b) noon, (c) 1400, and (d) 1600 LST, showing the SBC development features in an idealized zero background wind situation. Shaded areas represent the positive surface temperature anomaly, i.e. areas with higher temperature than domain-averaged.

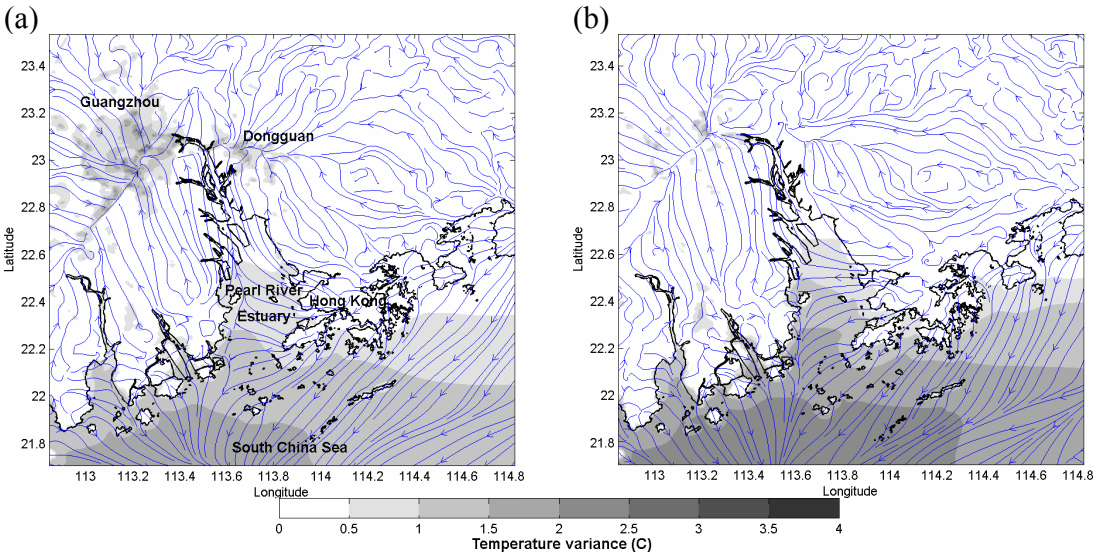

Figure 5-5: Same as Figure 4 but for (a) 0000, and (b) 0200 LST, showing the land breeze features over PRD.

(a)

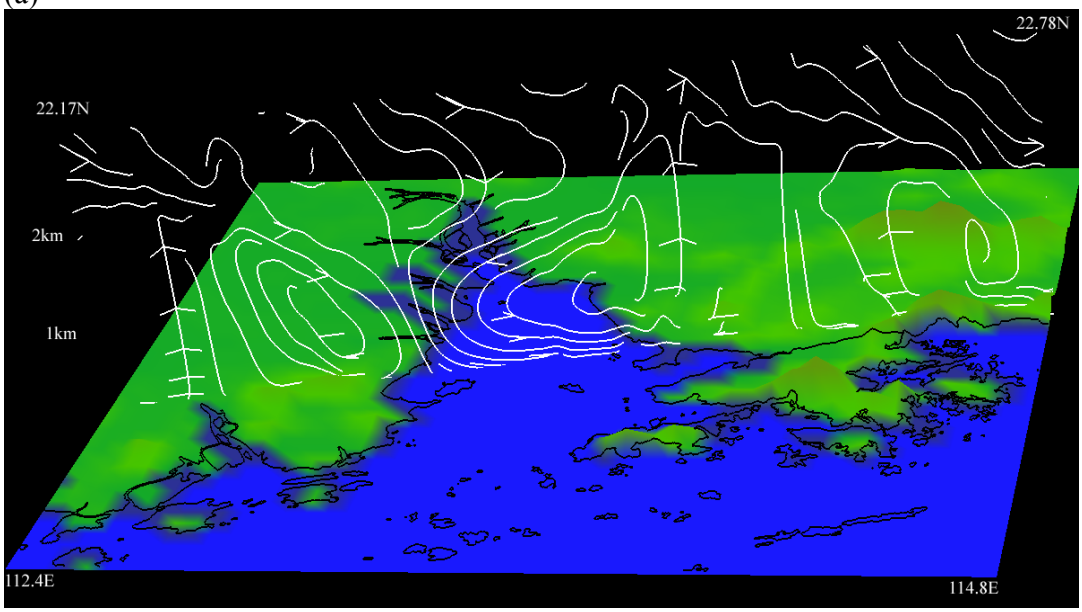

(b)

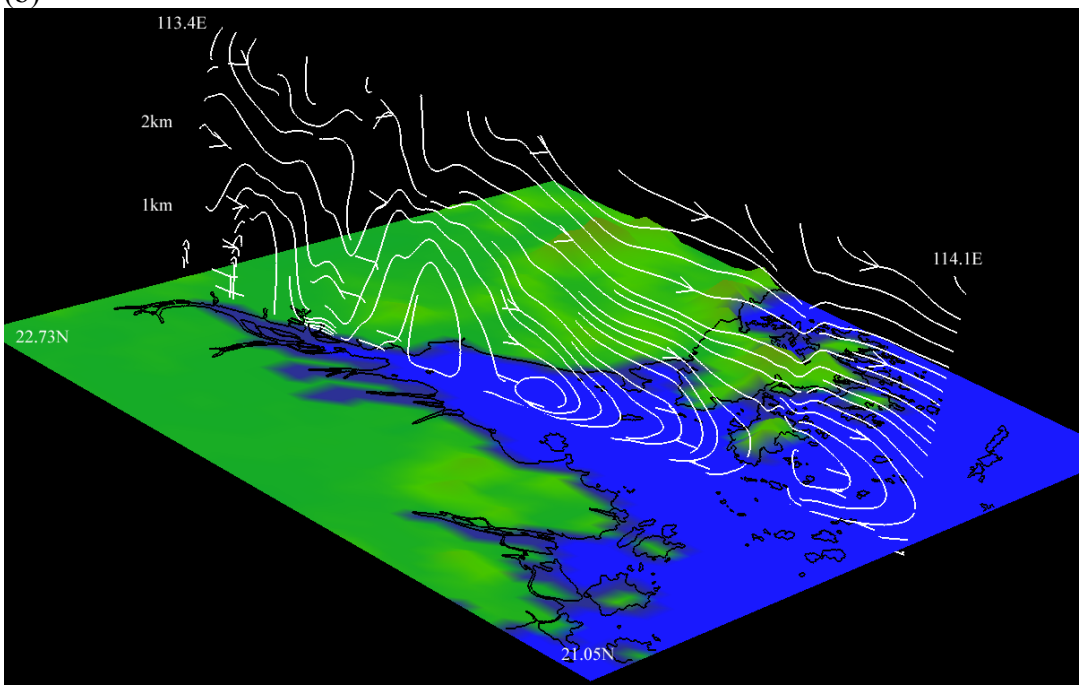

Figure 5-6: Vertical cross sections of streamline at 1400 LST projected on (a) west-east plane, and (b) south-north plane.

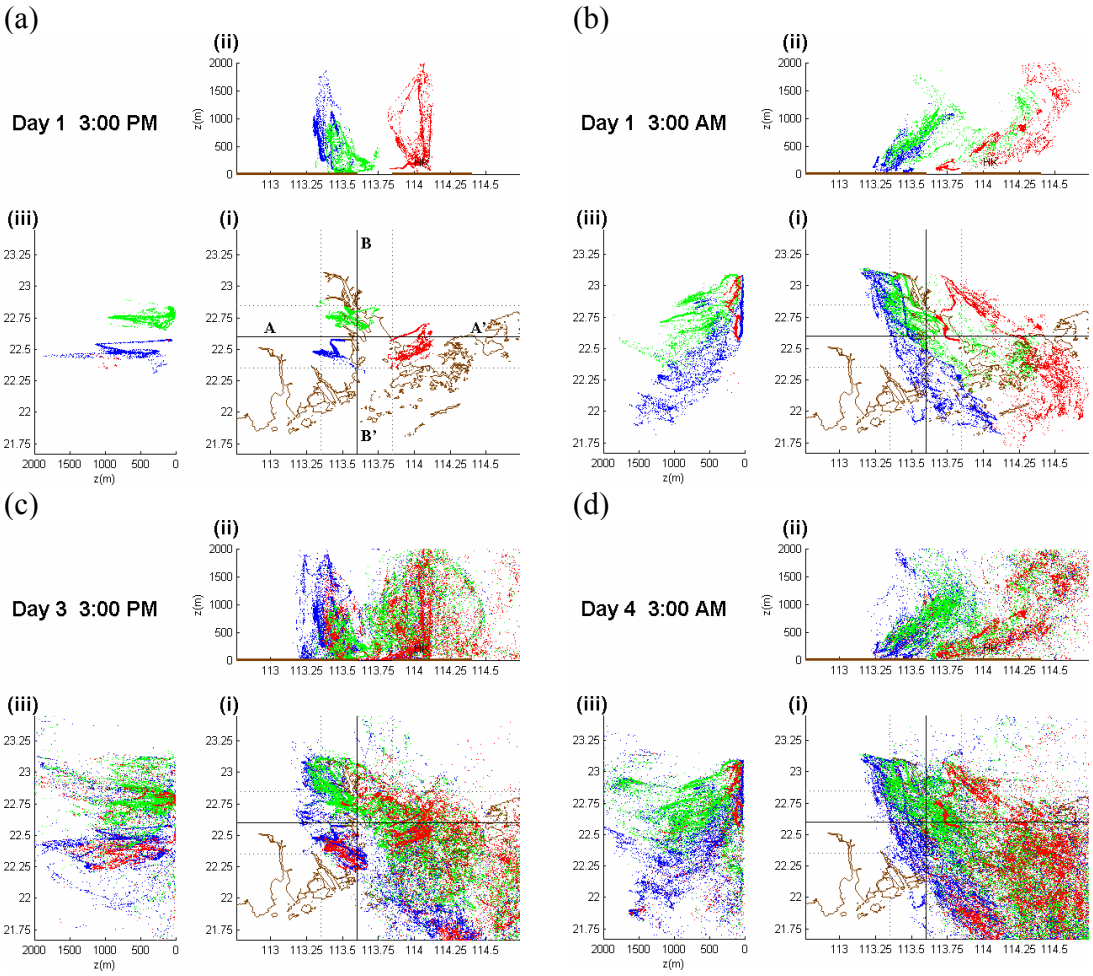

Figure 5-7: Particle-flow patterns at (a) 8-hr, (b) 20-hr, (c) 68-hr and (d) 80-hr simulation for the case without background winds and using the 2003 land-use map. Three emission sources at 100 m AGL located at Shenzhen (sources J in Figure 5-3, red color), Humen (source G in Figure 5-3, green color), and Zhuhai (source F in Figure 5-3, blue color) are used. Figure (i) shows the horizontal cross section of the dispersion pattern. Figure (ii) shows the west-east vertical projection on solid line AA' with thickness 50 km as shown in the dotted line. Figure (iii) shows the south-north vertical projection along solid line BB' with thickness 50 km as shown in the dotted line.

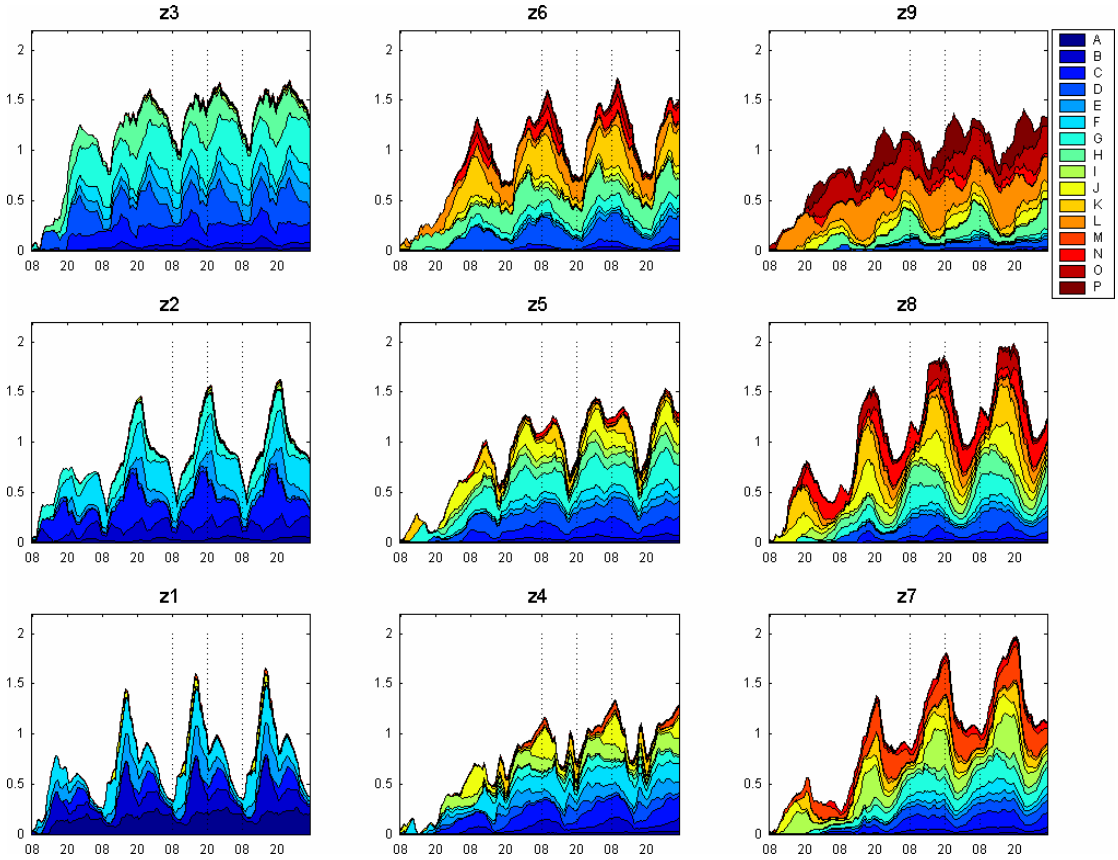

Figure 5-8: Time series of the amount of particle contributions from the 16 sources to the sampling zones for the experiment using the 2003 land-use map without background winds. x-axis is the LST. y-axis is the number of particle in unit of 10^4. Amount of particle were only counted below 2 km MSL.

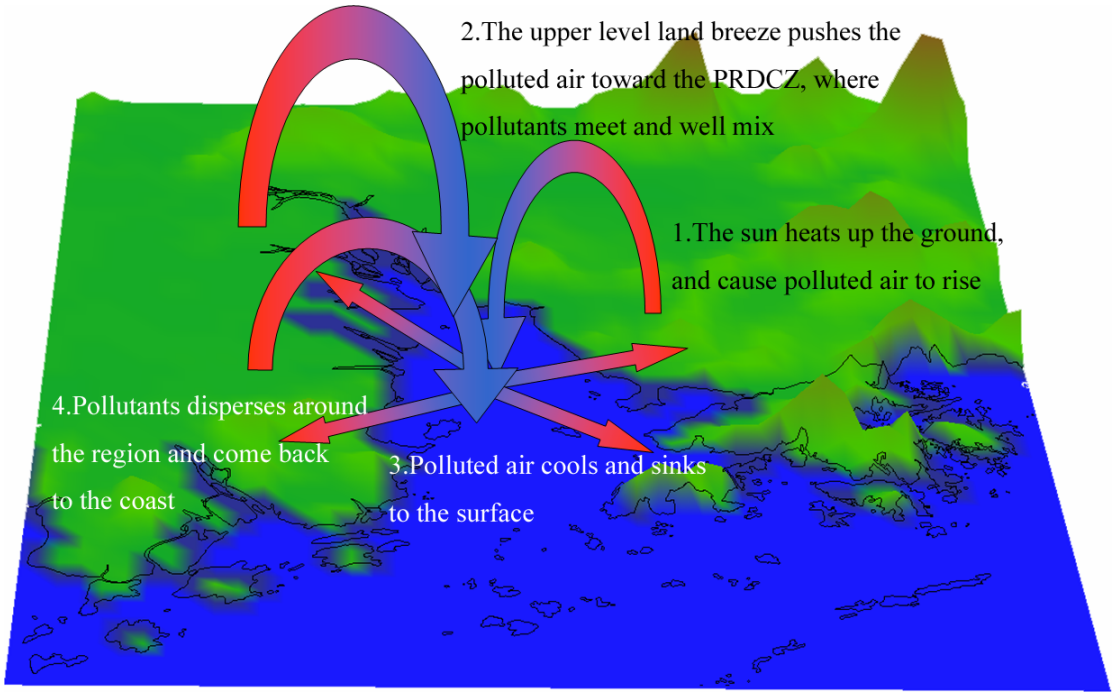

Figure 5-9: Schematic representation of the pollutant trapping mechanism by the sea breeze circulation over PRD.

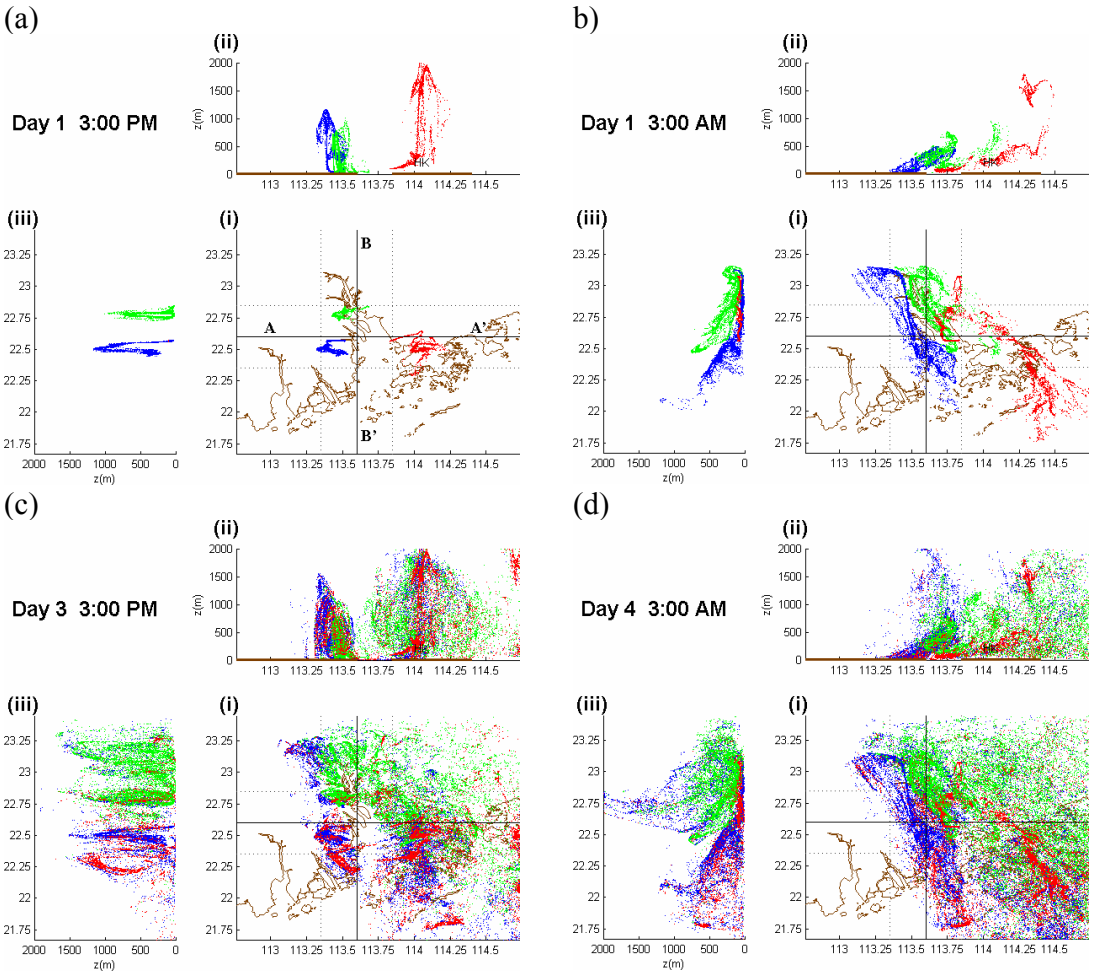

Figure 5-10: Same as Figure 5-7 but for experiment USGS-0.

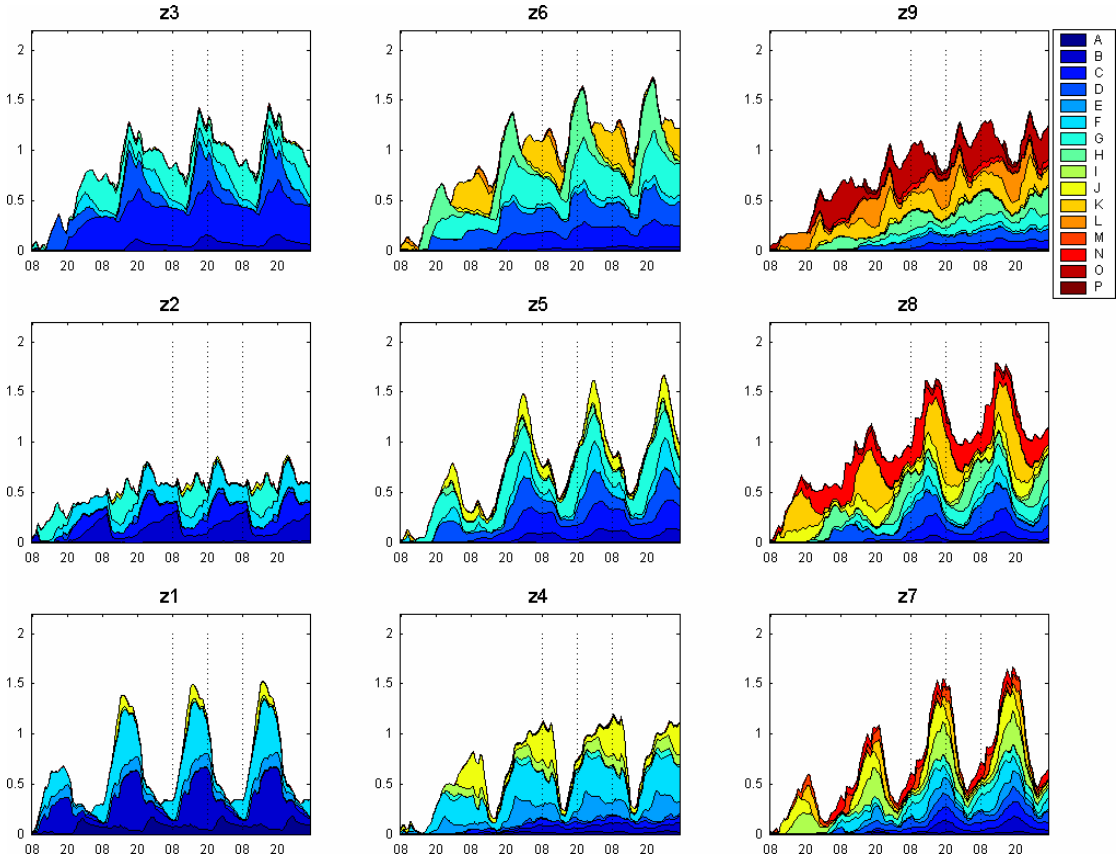

Figure 5-11: Same as Figure 5-8 but for experiment USGS-0.

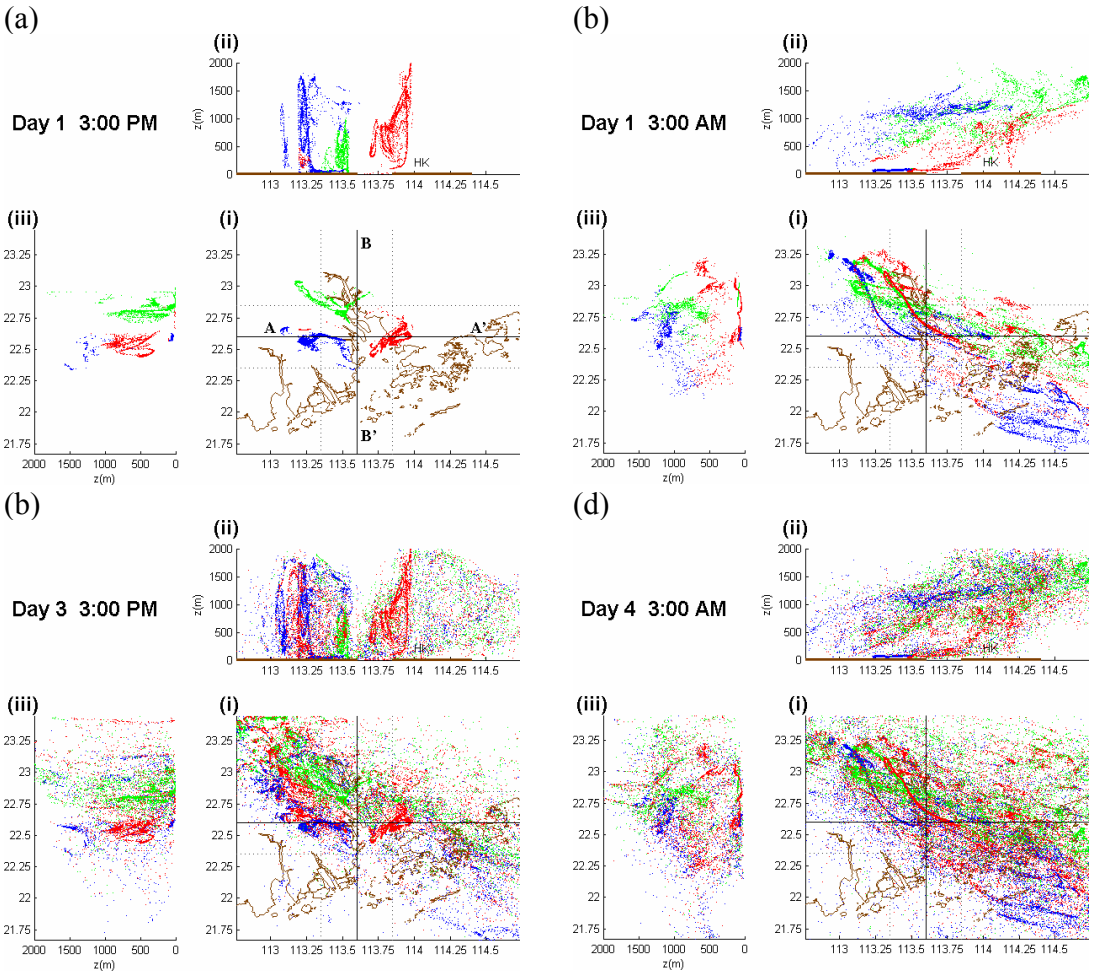

Figure 5-12: Same as Figure 5-7 but for experiment HKPD-3.

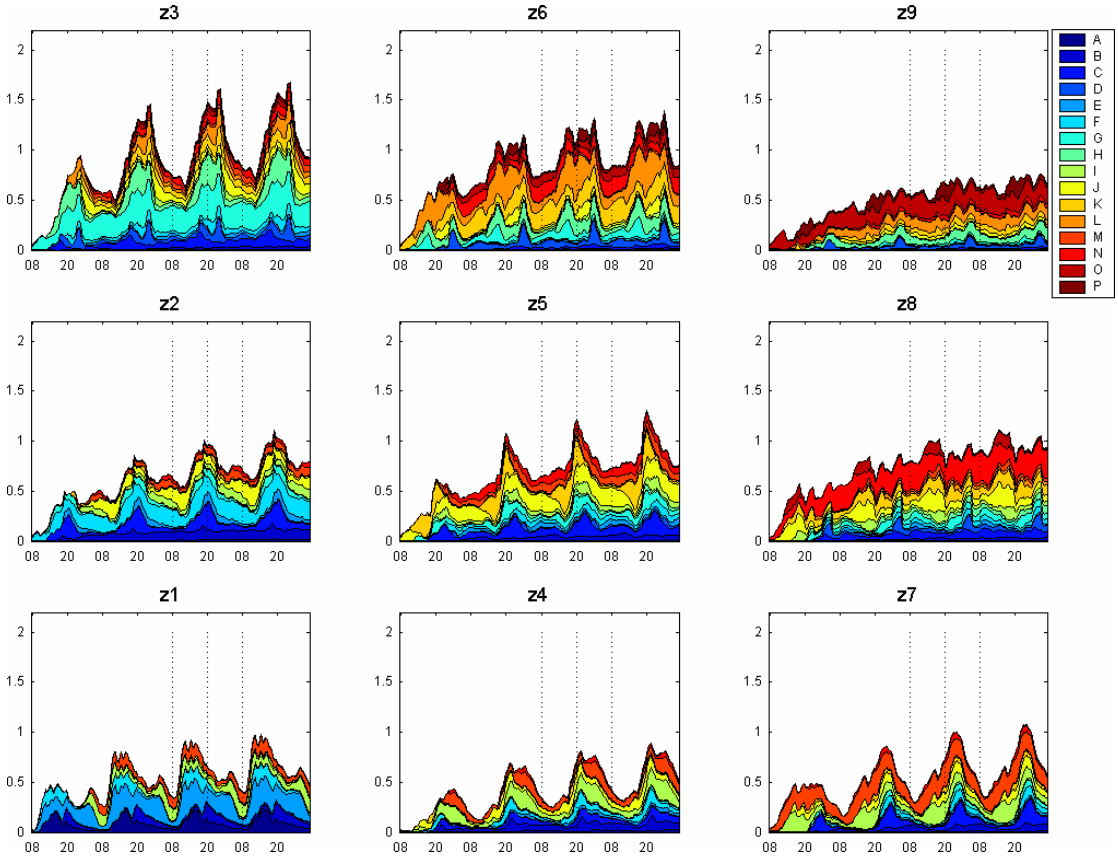

Figure 5-13: Same as Figure 5-8 but for experiment HKPD-3.

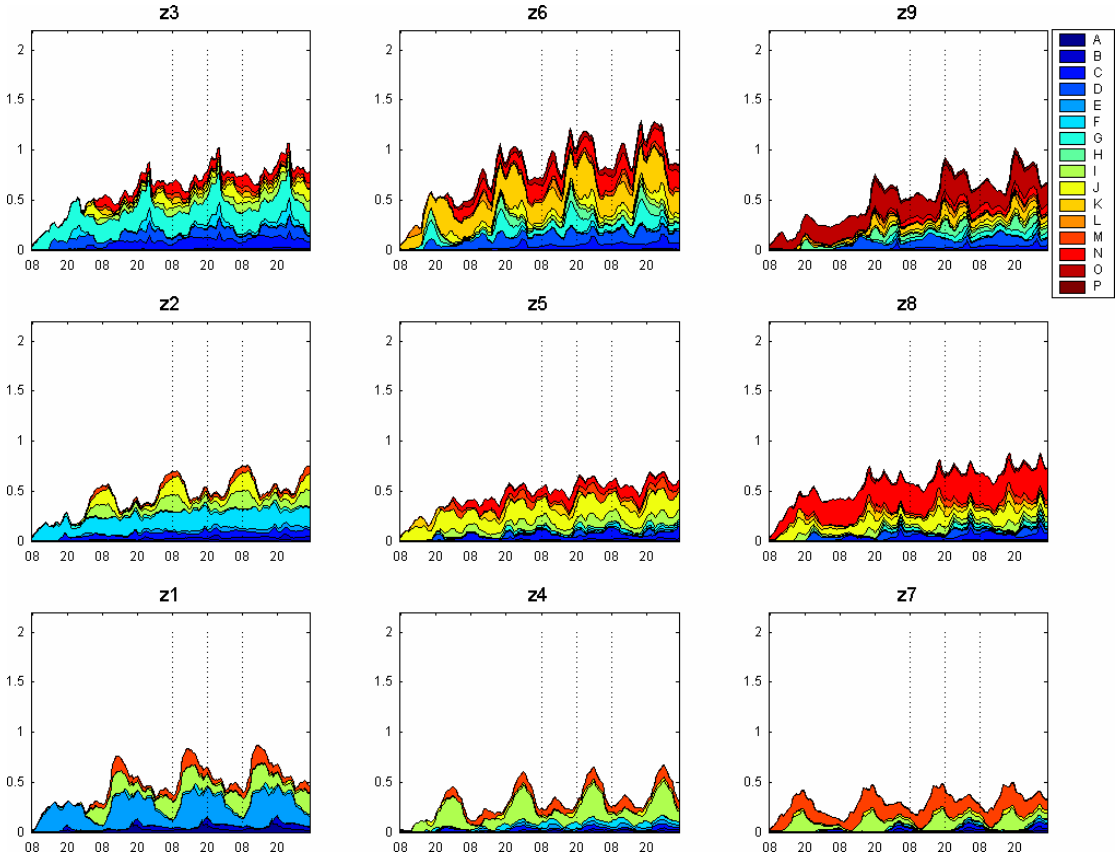

Figure 5-14: Same as Figure 5-8 but for experiment USGS-3.

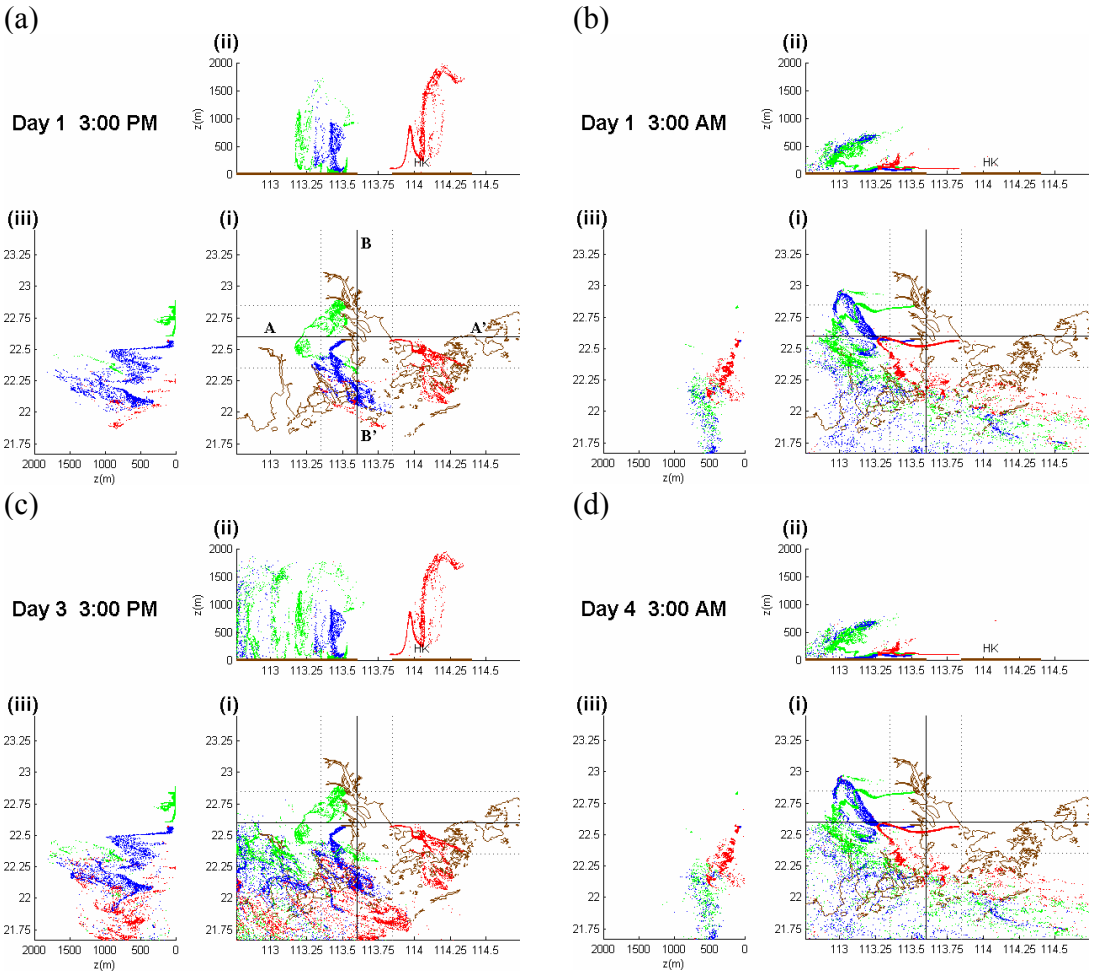

Figure 5-15: Same as Figure 5-7 but for experiment HKPD-6.

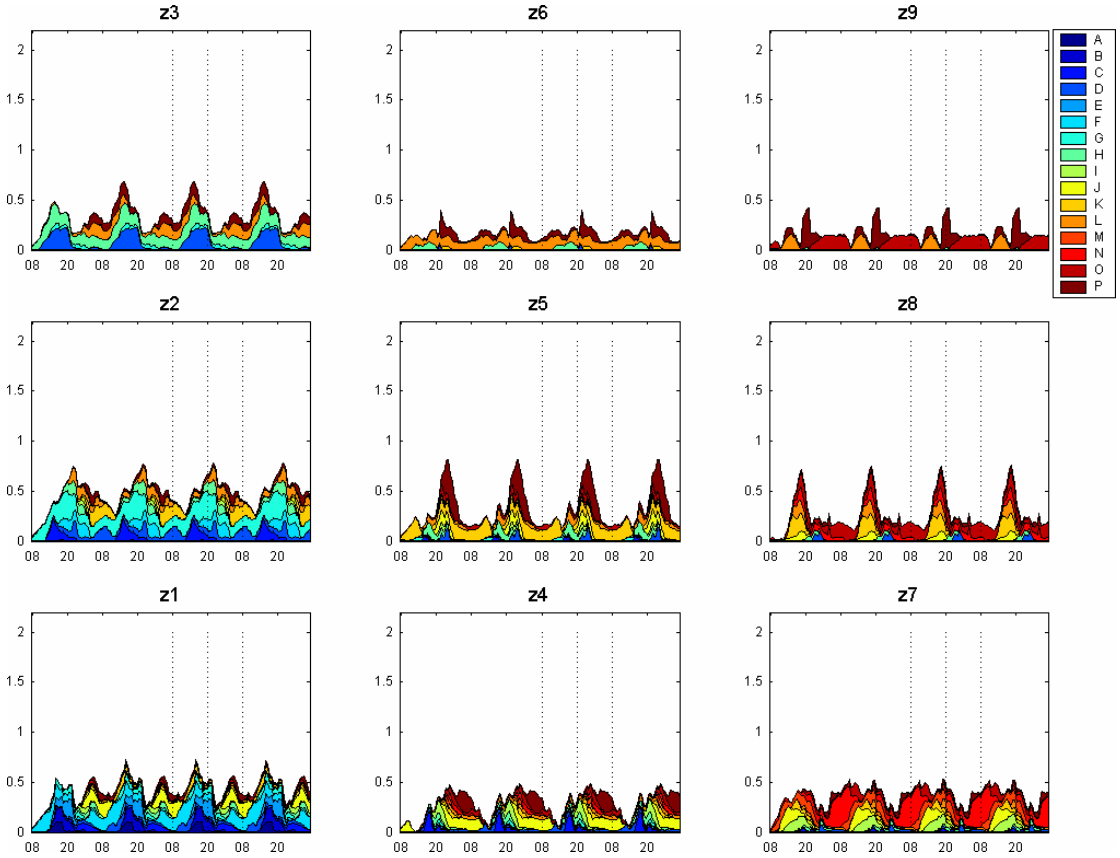

Figure 5-16: Same as Figure 5-8 but for experiment HKPD-6.

Table 5-1: Domain configurations and physics options used in the experiments.

Domain dimensions	300 x 300
Grid size	1 km
Vertical layers	35
Cumulus Scheme	None
Moisture scheme	Simple ice scheme
PBL scheme	MRF scheme
Radiation scheme	RRTM longwave scheme
Land surface scheme	Noah LSM

Table 5-2: The land-use map and wind profile used in the MM5 sensitivity experiments and the corresponding pollution level in the PRD.

Experiment	Land-use map	Wind profile	Pollutant trapping index
CONTROL	HKPD-2003	NIL	1.00
USGS-0	USGS-1993	NIL	0.83
HKPD-3	HKPD-2003	WEAK 3 m s^{-1}	0.70
USGS-3	USGS-1993	WEAK 3 m s^{-1}	0.54
HKPD-6	HKPD-2003	NORMAL 6 m s^{-1}	0.34

Chapter 6 A Physical Modeling Approach for Identification of Source Regions of Air Pollutants

Abstract

This chapter describes a new methodology to identify the contribution of primary and secondary air pollutants from the local/regional emission sources to Hong Kong, a highly urbanized city with complex terrain and coastlines. The meteorological model MM5 coupled with a three-dimensional particle trajectory model was used to identify salient aspects of regional air pollutant transport characteristics during some typical meteorological conditions over the Pearl River Delta (PRD) region. Several weighting factors were determined for calculating the air mass/pollutant trajectory and used to evaluate the local and regional contribution of primary pollutants over the PRD to Hong Kong pollution. The relationships between emission inventories, physical paths and chemical transformation rates of the pollutants, and observational measurements were formulated. The local and regional contributions of secondary pollutants were obtained by this conceptual module under different weather scenarios. Our results demonstrated that major pollution sources over Hong Kong come from regional transport. In calm weather, 78% of the respirable suspended particulates (RSP) totals in Hong Kong was contributed by regional transport, 49% was contributed by power plants within the PRD. During a normal-day situation, 71% of the RSP was contributed by regional transport and 45% was contributed by the power plants.

6.1 Introduction

Hong Kong, located in the southeast part of the Pearl River Delta (PRD) region, is a mega city of 1100 km^2 area containing 7 million people. In the past decades, both Hong Kong and the PRD have seen significant economic and population growth, but unfortunately, this growth is accompanied by deteriorated air quality within the entire PRD region. According to the Hong Kong Environment Protection Department (HKEPD), street-level pollution and smog are the two major pollution problems in Hong Kong. The poor air quality in street level is primarily caused by the high volume of local traffics. While the regional smog problems, such as the poor visibility, high levels of respirable suspended particulates (RSP) and ozone (O3) episodes, are caused not only by the emissions from the motor vehicles, but also by emissions from the industry and power plants both within Hong Kong and in the PRD (HKEPD, 2003).

Under a series of stringent air quality control implemented by the Hong Kong government, such as cutting sulphur content of industrial fuels and ameliorating motor vehicle fuel quality, emissions from local industry and automobile have been reducing in the recent decade. According to HKEPD, emissions of sulfur dioxide (SO_2), particulate matters (PM), and nitrogen oxide (NO_X) in 2003 dropped by 54%, 50% and 41% respectively compared with their levels in 1993 (see Figure 6-1). However, the ozone level in Hong Kong, as evidenced by the duration of poor visibility and frequency of occurrence of ozone episodes, has been in an increasing trend in the recent years (HKEPD, 2003). The percentage of dates with poor visibility (visibility less than 8 km with relative humidity recorded less than 80%) in 2003 (15%), as shown in Figure 6-2,

was 2.5 times the 1993 value (6%). Since ozone and smog problem is a regional air pollution issue, the rising trend generally reflects deterioration in air quality on a regional scale over the past decade. A question has been raised as to whether local emission sources or pollutants transported from outside Hong Kong are responsible for this air quality impairment.

As air pollution is a trans-boundary issue, certain air pollutants can be transported long distances and impact the locations far from the sources. It is sometime difficult to identify the source regions of air pollutants which have contribution to the pollution episodes. In previous air quality studies, air mass trajectory analyses, which trace air parcels forward or backward in time from the receptor, was generally used to identify source regions of air pollutants (e.g. Harris et al., 1994; Chan et al., 2001; Oltmans et al., 2004). However, this method usually only involves physical advection calculation, and it cannot compute or categorize the contributions of specific pollutants.

The purpose of this chapter is to introduce a new methodology which based on trajectory calculations for identification of source regions of air pollutants. The meteorological model MM5 coupled with a three-dimensional particle trajectory model (PTM) was used to identify salient aspects of regional air pollutant transport characteristics during two typical meteorological conditions over the PRD: 1) calm weather days with stationary synoptic-scale forcing. 2) normal-day situations with most frequently occurrence wind profiles. Several weighting factor tables were established to the air mass trajectory calculations and used to evaluate the local and regional contribution of primary pollutants to Hong Kong pollution. A conceptual module was set up for the air quality study in the region. The module formulated the relationships

between emission inventories, physical paths and chemical transformation rates of the pollutants, and observational measurements. The conversion rates of primary gas phase pollutants to secondary PM (e.g. SO_2 to sulfate and NO_X to nitrate) were obtained by the conceptual module. These conversion rates provided the information of local and regional secondary pollutants in Hong Kong. The differences of pollutant transport characteristics over western and eastern Hong Kong have also been investigated.

6.2 Methodology

6.2.1 Meteorological Model and Configuration

The physical parameterization schemes are summarized in Table 6-1. A 1-km-fine-resolution (mesh size, 300 x 300) domain covers Hong Kong and PRD (see Figure 6-3) was used to resolve local and regional scale atmospheric circulations features.

In order to investigate the typical features of the local and regional scale atmospheric circulations and isolate these conditions from the other complexities of the real atmosphere, idealized meteorological initial and boundary conditions were ingested to the MM5 simulations. The pollutants transport characteristics over PRD under two different meteorological conditions were examined. The first one represented an extreme situation of total stationary weather, with no horizontal pressure gradient and no background winds for in the MM5 initial and boundary conditions, i.e. circulations were solely driven by the local thermal effects over the PRD. The second one represented a typical normal-day situation with 6 m s^{-1} north-easterly wind at the surface. Detailed discussions of the idealized meteorological conditions setup can be found in Lo et al. (2006b). A 30-hour simulation was conducted by MM5, with the first six hours used as

the spin-up, and the rest 24 hours as the effective simulation in order to capture the daily diurnal cycle of the thermally induced winds (LSBC and UHIC) over PRD.

6.2.2 Particle Trajectory Model (PTM)

A particle trajectory model (PTM) was used to investigate the air mass flowing pattern driven by the local atmospheric circulations in PRD. The prognostic model MM5 was used to predict meteorological conditions, and advection were carried out by the PTM in which individual fluid particles were transported according to the wind provided by MM5. Pollutant-flow trajectory in the PTM was simulated by tracking a large set of particles. Subsequent positions of each particle which represented a discrete element of pollutant mass at time $t+\Delta t$ are computed from the following equation:

$$x_i(t+\Delta t) = x_i(t) + u_i \Delta t \tag{6-1}$$

where i = 1,2 or 3 for the x, y, and z component. The wind velocity $u_i(x_i,t)$ were obtained directly from the meteorological model MM5 (Fung et al., 2005). The time step Δt = 5s is chosen to resolve fine scale flow. Since the grid-scale meteorological variables are defined only on the 1-km MM5 model gridmesh, a linear interpolation scheme (both in time and in space) is used to estimate their values at each particle location. Continuous-equal-spacing 4 by 4 emission sources were chosen (see Figure 6-3 for their exact locations) to release particle tracers, in order to identify the locations of pollution sources over PRD which contribute to Hong Kong pollution. They were all released with the same emission rate of one particle per ten seconds at two different heights: one was located at 10 m AGL representing ground level emissions; the other was located at 300 m AGL representing emissions from power plants. A 5-day simulation was conducted

by the PTM and the 24-hour MM5 simulated winds were repeatedly used to drive the PTM during the simulation period. To investigate the pollutant transport characteristics over the western and eastern Hong Kong, two sampling zones roughly representing western and eastern Hong Kong were chosen (see Figure 6-3 for the extensions).

6.2.3 Emission Weighting Factors

In reality, the distribution of air pollution emission sources is not homogenous across the PRD region. The emission inventories highly depend on the degree of urbanization, industrial and economic activities, as well as population in the region. Because of the inhomogeneous distribution of the emission sources, constant emission rate in the PTM cannot represent the actual situation over the PRD. Therefore, several weighting factor tables of various pollutants were introduced for each source. By spatially interpolating the emission database provided by HKEPD in 2001, three weighting factor tables of primary pollutants PM, SO_2 and NO_X were obtained in Table 6-2 to Table 6-4 respectively. The weighting factor represents the percentage of annual averaged contribution of the emission source to the total emission of the specific pollutant in the study domain. Two types of emission sources were evaluated: 1) ground level emissions (10 m AGL), and 2) power plant emissions (300 m AGL). Major surface-emission sources include road vehicles, railways, marine traffic, and fuel combustion. The power plant emissions included the 59 major power plants within the study domain (see Figure 6-3 for the locations).

For the emission of PM over the PRD, as shown in Table 6-2, surface emission at source D (Guangzhou) has the highest weighting factor of 26.0, indicating it contributes 26% to the total PM emission in the study domain. The second largest producer with

weighting factor 12.7 is contributed by the surface emission at source J (Shenzhen). The local street-level emissions from Hong Kong (sources I and M with weighting factor of 0.57 and 2.01 respectively) are relatively low comparing with the sources outside the territory. The total PM emission from power plants is around one-eighth of the surface emissions. Among the power plant emission, source H, the areas between Guangzhou and Dongguan, is the major contributor with weighting factor 4.38. The mass proportion parameter M_{PM} = 0.15 stated in Table 6-2 implies the overall emission of PM in mass contributed 15% to the total emission of PM, SO_2 and NO_X in the region.

Most of the emissions of SO_2 (68%) in the study domain, as summarized in Table 6-3, come of power plants. Major SO_2 sources included the emissions from power plants located at Guangzhou (source H, WF = 17.09) and Dongguan (source K, WF = 14.7), and ground level emissions at Guangzhou (source D, WF = 10.54). The three power plants in Hong Kong, Lamma power station (source M), and Castle Peak power station and Black Point power station (source I), with weighting factor 5.9 and 4.74 respectively, contribute around 11% of total SO_2 emission in the region. Note that the mass proportion parameter M_{SO} = 0.53, denotes SO_2 is the major primary pollution emissions in the region, contributing over half of the pollutant mass among the three primary sources.

For the NO_X emission which is listed in Table 6-4, surface emissions and plant power emissions contribute about the same amount to the region. Major contributor includes emissions from the area sources (source D, WF = 12.37), and power plants emission at Guangzhou (source H, WF = 12.14) and Dongguan (source K, WF = 12.14). The overall NO_X emission in mass is 0.32 among the total emission of the three primary pollution emissions.

To evaluate the local and regional contribution of primary pollutants to Hong Kong pollution, the amount of tracers from the 16 sources collected in the sampling zones was multiplied by their corresponding weighting factor. For example, the contribution of pollutant X (where X could be PM, SO_2 or NO_X) from emission source i to Hong Kong at time t is calculated by:

$$X(i,t) = AT(i,t) \cdot M_X \cdot WF_X(i) \tag{6-2}$$

where M_X and is WF_X the mass proportion parameter and the weighting factor of the source i for a specific pollutant, respectively. AT is the amount of tracers collected in the sampling zones (western or eastern Hong Kong) from the source. Note that Equation (6-2) provides the relative contribution of the 16 sources to Hong Kong pollution instead of the absolute amount of pollutants.

6.2.4 Conversion Factors

Ambient particulate matter consists of both primary and secondary particles (Seinfeld and Pandis, 1998). Primary particles are those directly emitted by sources. These particles undergo few changes between source and receptor, and the atmospheric concentrations are, on average, proportional to the quantities emitted. On the other hand, secondary particles are those formed in the atmosphere from gases which are directly emitted by sources. Sulfate, nitrate, ammonium, and possibly hydrogen ions, are the most common components of secondary particles in the atmosphere. These particles are mainly associated with emissions of SO_2, NO_X, and ammonia (NH_3) gases.

Yuan et al. (2006b) estimated that secondary aerosol accounted for an annual average of 44% of PM_{10} in Hong Kong. Therefore, formation of secondary particles

should not be neglected for any PM study in Hong Kong and PRD area. The ambient concentrations of secondary particles are not necessarily proportional to quantities of emissions since the rates at which they form and their gas/particle equilibria may be controlled by factors other than the concentration of the precursor gases. Reactive organic gases are also precursors to secondary particles. On the basis of the past observational records, Yuan et al. (2006a) has derived an empirical relationship between local secondary sulfate and secondary organic carbon (SOC) in Hong Kong, and this relationship could serve as a tool for further secondary organic compound estimation. Since the emission and chemical transformation processes of SOC precursors are much less known than those for inorganic species, this study limits itself to the inorganic components of secondary aerosol.

In the present study, the ambient RSP level is roughly assumed as the sum of primary particles and two types of secondary inorganic particles, ammoniated sulfate and ammoniated nitrate. Two parameters, R_S and R_N, are introduced here to account for the fractions of SO_2 and NO_X that are eventually transformed to sulfate and nitrate, respectively. A first-order assumption has been made here that these parameters remain constant for all the source points, regardless of how far the emission sources to the receptor are. Therefore, Equation (6-2) could be generalized to the form

$$\text{RSP} = \text{Primary PM (PPM)} + \text{Sulfate} + \text{Nitrate} \tag{6-3}$$

$$RSP(i,t) = AT(i,t) \cdot \{M_{PM} \cdot WF_{PM}(i) + R_S \cdot M_{SO} \cdot WF_{SO}(i) + R_N \cdot M_{NO} \cdot WF_{NO}(i)\} \tag{6-4}$$

where

$$R_S = \left(\frac{SO_4}{PPM}\right)_{Obs} \cdot \frac{M_{PM} \cdot \sum_i \sum_t AT(i,t) \cdot WF_{PM}(i)}{M_{SO} \cdot \sum_i \sum_t AT(i,t) \cdot WF_{SO}(i)} \quad (6\text{-}5)$$

$$R_N = \left(\frac{NO_3}{PPM}\right)_{Obs} \cdot \frac{M_{PM} \cdot \sum_i \sum_t AT(i,t) \cdot WF_{PM}(i)}{M_{NO} \cdot \sum_i \sum_t AT(i,t) \cdot WF_{NO}(i)} \quad (6\text{-}6)$$

Based on the PM_{10} observations in a 4.5-year period, Yuan et al. (2006b) applied Positive Matrix Factorization model to apportion the ambient PM level in Hong Kong into sources or source categories. This technique could be used for source identification and as a result, sources responsible for primary pollutants as well as secondary sulfate and nitrate could be derived and the values, also shown in Table 6-5 could serve as inputs to the above equations. The components in Equations (6-5) and (6-6) include chemical transformation rates (R_S and R_N) which are derived from other components in the present study, observational measurements (SO_4/PPM and NO_3/PPM), spatially varied source contribution resulted from emission inventories (*M* and *WF*), and physical paths of the air masses/pollutants (*AT*).

6.3 Regional Pollutant Sources during Calm Weather

Geographically, Hong Kong is a highly urbanized city with mountainous terrain and complex coastlines. With a calm background winds or weak synoptic forcing which is conducive to severe air pollution episodes, thermally induced winds such as land sea breeze circulation (LSBC) and urban heat island circulation (UHIC) can occur in Hong Kong and PRD. The LSBC has been proved as a significant influence on air-flow pattern and affects the air quality, both in Hong Kong (Kok et al., 1997; Fung et al., 2005; Huang et al., 2005; Lam et al., 2006) and in the PRD (Lo et al. 2006a, 2006b). For this

reason, we will first examine the pollutants transport characteristics over PRD under a situation of total stationary weather. In this simulation, no horizontal pressure gradient and no background winds were ingested in the MM5 initial and boundary conditions. This case represents an extreme situation of total stationary synoptic weather, and therefore circulations were solely driven by the local thermal effects.

6.3.1 Particle-Flow Patterns

Three plume emitters located at ground level (10 m AGL) at Guangzhou, Shenzhen, and Hong Kong (sources D, J, and M respectively) were selected to demonstrate the pollutants transport characteristics under this stationary meteorological condition. Figure 6-4 illustrates features of the particle-flow patterns. The positions of particles at selected times were projected onto a horizontal and a vertical plane. These particle-flow patterns were not weighted and it can be regarded as the physical path component AT in Equations (6-4), (6-5) and (6-6).

In Figure 6-4a, at 1500 LST of the first day simulation, while the afternoon sea breeze circulation (SBC) was dominant over the PRD, the particles released at Shenzhen and Hong Kong were trapped by the closed SBC over the Hong Kong territory. From the vertical cross projection (Figure 6-4aii), the tracers released at 10 m AGL can be brought to 2 km by the SBC. The horizontal extension of the SBC was about 20 to 30 km and penetrated almost half of the Hong Kong territory. On the third afternoon (Figure 6-4b), since there was no strong synoptic wind to clean the pollutants away from the simulation domain, the situation became much worse. Pollutants released at Guangzhou were transported to Hong Kong and well-mixed with the other two sources within the PBL by the SBC.

This result demonstrates that under a calm meteorological condition, air mass/pollutant flow pattern over PRD are substantially controlled by the LSBC. Pollutants emitted in the PRD can be transported long distances by the LSBC and impact the air quality in Hong Kong. In the afternoon, the SBC can trap the pollutants from local production or from regional transport, and enhance the pollutant accumulation and cross-mixing within the PBL over the Hong Kong territory.

6.3.2 Contribution of the Regional Emission Sources

By applying Equation (6-4), time series of the contribution of the ground level emissions and power plant emissions from the 16 sources to total RSP with the PBL (below 1 km MSL) in western/eastern Hong Kong under this stationary meteorological condition is shown in Figures 6-5 and 6-6.

The RSP in western Hong Kong, as shown in Figure 6-5, were mostly contributed by the surface emissions from Guangzhou (source D) in this case. The power plant emissions from local production (source I) and regional transport from Dongguan (source K) and Shenzhen (source J) also contributed a large amount of RSP to Hong Kong. The pollution level in Hong Kong was highly correlated with the diurnal cycle of LSBC. During the daytime, while SBC was prominent, pollutants emitted from local production (source I) and from the neighboring city Shenzhen (source J) were trapped by the SCB. The SBC not only trapped local pollutants, but also transported, accumulated and cross mixed pollutants from the other PRD cities (source C, D, H and K), thus causing a late afternoon daily pollution peak around 2000 LST in the western Hong Kong. During the nighttime, emission sources from eastern Pearl River coast (source I, J, and K) generally dispersed away the territory by the land-breeze. However,

at the same time, large amount of pollutants were being transported from northwestern PRD (source D and H) to western Hong Kong by the regional scale land-breeze over the PRD, partly compensating the dispersion by local land-breeze. In addition, pollutants from the local emission source M (Kowloon) were transported to the western Hong Kong during the nighttime.

The air quality in the eastern Hong Kong, as shown in Figure 6-6, was generally better than that in western side. Table 6-6 summarizes the pollution level in western and eastern Hong Kong. Under the calm meteorological condition, the amount of RSP in eastern side (40%) was 33% less than the value in western side (60%). During the daytime, large amount of pollutants emitted from ground level at eastern Shenzhen (source N) and small amount pollutants from local production (source M) were trapped by the SCB. Because the eastern Hong Kong is not directly connected with the Pearl River Estuary (see Figure 6-3), where most urban and industrial areas are located along the two sides, regional pollutant transport by the SBC was not as serious as that in western side during the afternoon. Instead, pollutants were mainly transported to eastern Hong Kong during the nighttime by the land breeze, and accumulated in the territory.

Table 6-7 summarizes the proportion of pollutants from local production and regional transport in Hong Kong during the 5-day simulation. Emission sources I and M are regarded local production while the other emission sources are regarded as regional transport. During the calm meteorological conditions, 78% of the RSP in Hong Kong were contributed by regional transport while the local production only contributed 22%. The power plants within the PRD contributed 49%, while the local power plants only contribute 16% of the RSP total in Hong Kong.

6.4 Regional Pollutant Sources during Normal Day

Hong Kong is located in the sub-tropical zone; the surface prevailing winds are affected by the northeasterly trade-wind belt most of the time. According to the wind statistics reported by Hong Kong Observatory (Wong and Kwan, 2002), between 1990 and 2000, the probability of prevailing easterly to northeasterly surface winds was about 65%, with an average wind speed of 6 m s^{-1} at Waglan Island, the station generally accepted as representing background wind data for Hong Kong. Therefore in this simulation, a wind profile with 6 m s^{-1} northeasterly wind at the surface and 6 m s^{-1} westerly wind above the PBL (1.5 km AGL), was ingested into the MM5 initial and boundary conditions, in order to examine the pollutants transport characteristics over PRD in a normal-day situation.

6.4.1 Particle-Flow Patterns

Figures 6-7 present the particle-flow patterns of the three sources (source D, J and M) under this normal-day meteorological condition. From the vertical cross section, it can be seen that the structure of the SBC was strongly influenced by the background winds. The SBC cells were not well developed compared to that in calm weather case (Figure 4) over Hong Kong. However, these 6 m s^{-1} winds could not completely eliminate the afternoon SBC, since a small account of pollutants were still trapped along the Hong Kong coast during the afternoon. The air quality of Hong Kong in this situation was much better than those during calm weather. Most of the pollutants were cleaned away in the computational domain by the strong background winds.

6.4.2 Contribution of the Regional Emission Sources

The contribution of the 16 emission sources to total RSP in western Hong Kong during this normal-day situation is shown in Figure 6-8, while the values in eastern Hong Kong is shown in Figure 6-9. Comparing with the case without background winds (Figure 6-5 and 6-6), the strong winds generally help to disperse the pollution and reduce the diurnal variation of surface-emission sources. The level of pollution trapping and accumulation in both western and in eastern Hong Kong was substantially reduced. During the daytime, because the strong background winds still cannot destroy the SBC completely, small amount of pollutants were trapped over the Hong Kong coast as evidenced by the daily pollution maximum from source I and J to western Hong Kong (Figure 6-8), and source N and M to eastern Hong Kong (Figure 6-9). For source N, it is interesting to see that during the nighttime, while the sea-breeze diminished, pollutants were no longer trapped in the eastern Hong Kong (Figure 6-9, N), but being transported by the background wind toward the western Hong Kong (Figure 6-8, N).

In this normal-day situation, pollutant trapping and accumulation was not severe over Hong Kong. As summarized in Table 6-6, the ratio of the total amount of pollutants from the 16 sources accumulated in Hong Kong to that in the calm weather case during the whole 5-day simulation is 0.28, indicates there is a 72% difference in the amount of pollutants accumulation in Hong Kong between the two situations. Regional transport contributed 70% of RSP total in Hong Kong while the local production only contributed 30%.

6.5 Conclusions

Using the state-of-the-art meteorological model MM5 coupled with a three-dimensional particle trajectory model, the pollutant transport characteristics over Hong Kong under two typical meteorological conditions were studied. A conceptual module was used to evaluate the contribution of source regions of RSP. The results demonstrated that major pollution sources over Hong Kong come from regional transport. In calm weather days, 78% of the RSP in Hong Kong was contributed by regional sources outside Hong Kong, of which surface emissions from Guangzhou are the largest contributor. On the other hand, in normal-day situation with northeasterly surface wind, 71% of the RSP was contributed by regional transport. Ground level emissions from Shenzhen affect Hong Kong the most in this case.

A physical modeling approach was used to calculate two chemical gas-to-particle conversion rates for SO_2 to sulphate (R_S=0.29) and NO_X to nitrate (R_N=0.24). It should be pointed out that the derivation of these values is subject to the assumption that they remain constant for all the sources and time. In addition, these values tended to be very sensitive to the accuracy of emission data for primary pollutants, based on Equations (6-5) and (6-6). Nevertheless, although these two parameters are in first-order approximation in present study, our results demonstrate the importance and usefulness of these two parameters in estimating ambient levels of secondary pollutants in air quality study. For a more accurate investigation, detailed and sophisticated atmospheric chemistry modelling would be required to estimate these two parameters, including their spatial and temporal variations.

The air quality in eastern Hong Kong is relatively better than the western side. It can be explained that the LSBC cells in the western Hong Kong are directly connected with the Pearl River estuary, where most urban and industrial areas are located along the two sides. Pollutants emitted from both sides of the Pearl River Estuary can be transported, cross-mixed and re-circulated over the western Hong Kong, which generally causing worse air quality.

Finally, this chapter illustrates the significance of regional transport on air pollution in the entire PRD region. Therefore, to better manage the regional air pollution problem, the government of Hong Kong should work more closely with its Guangdong counterpart to achieve good air quality for the whole region in the long term.

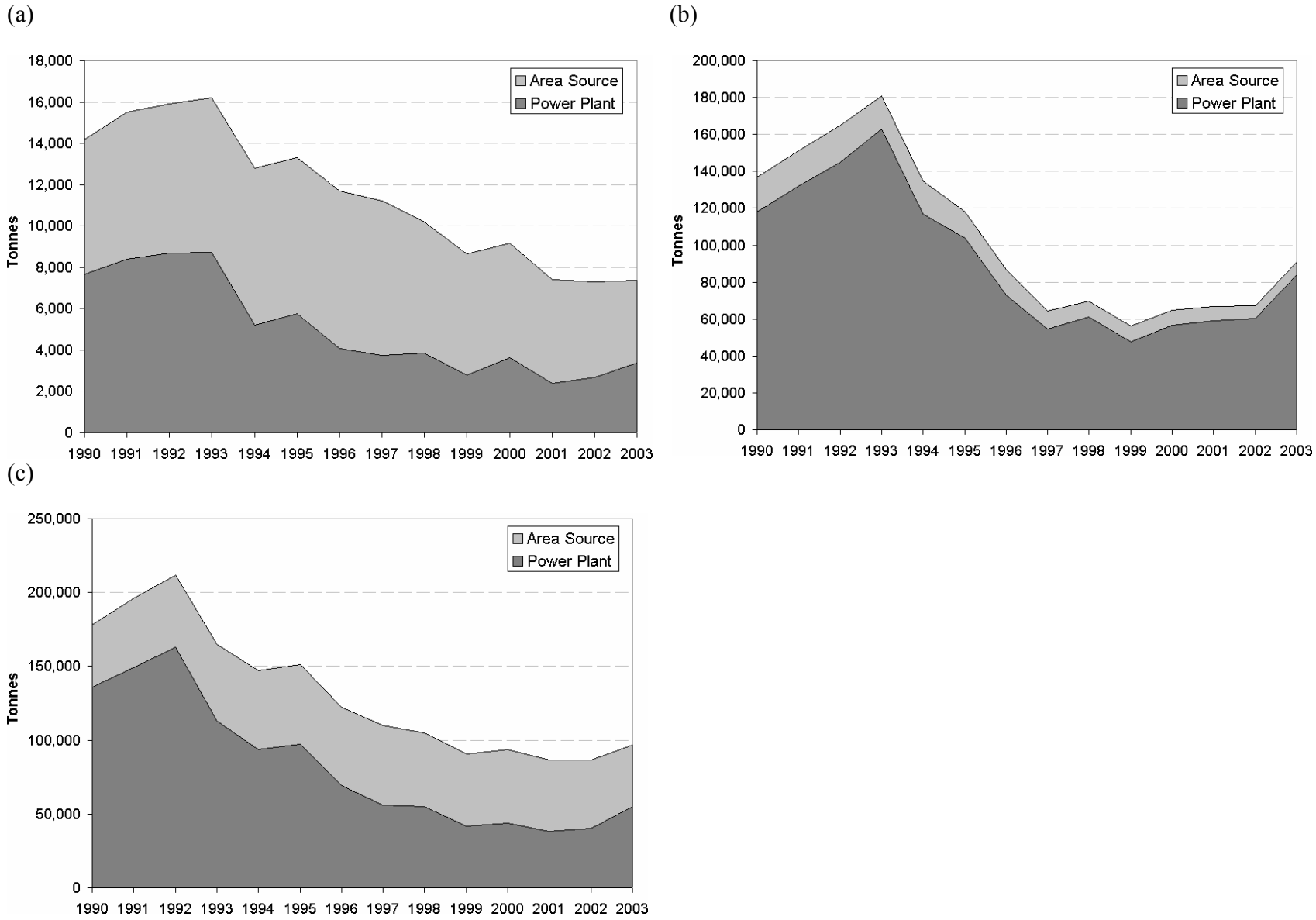

Figure 6-1: Long term trends of air pollution emission in Hong Kong. (a) PM, (b) SO_2 and (c) NO_X.

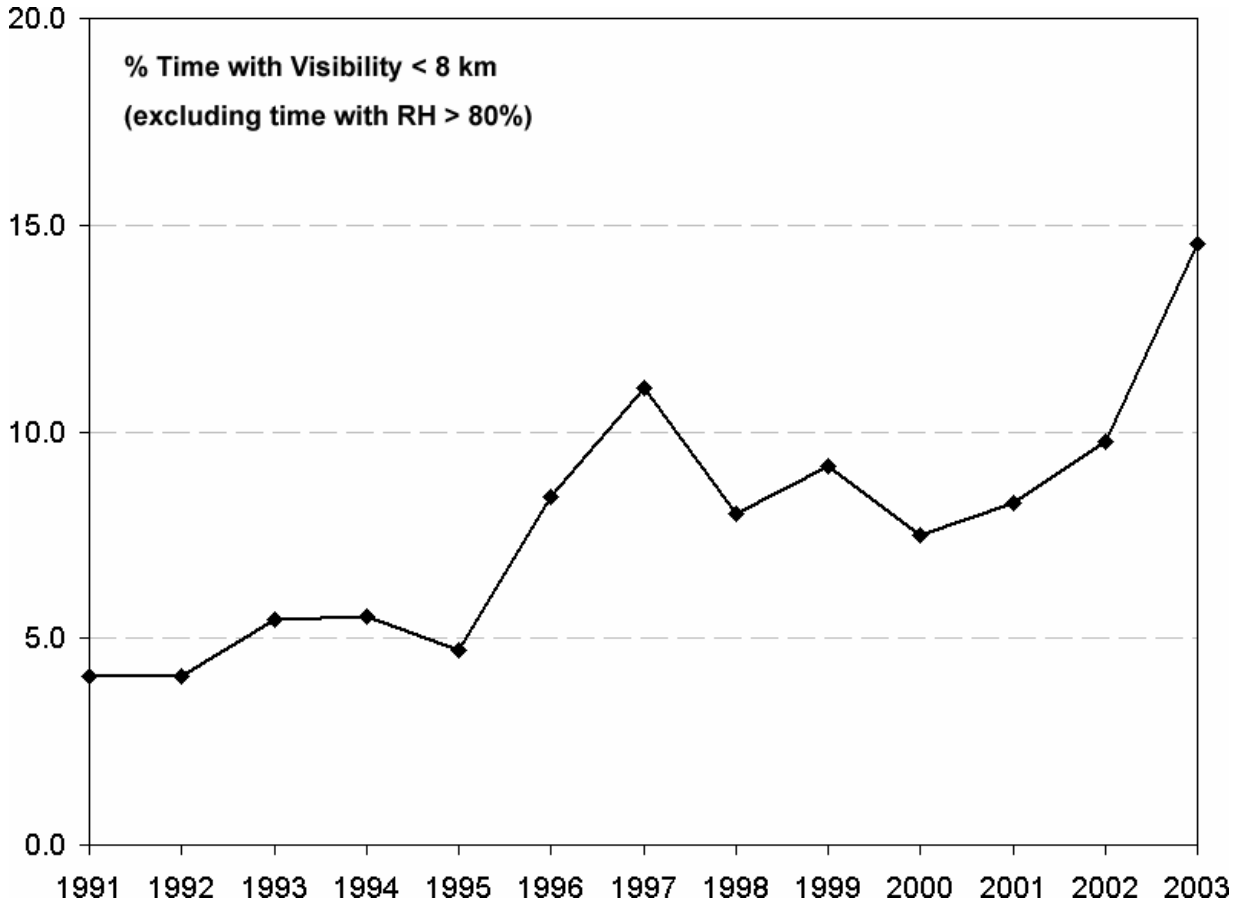

Figure 6-2: Trends of visibility impairment in Hong Kong.

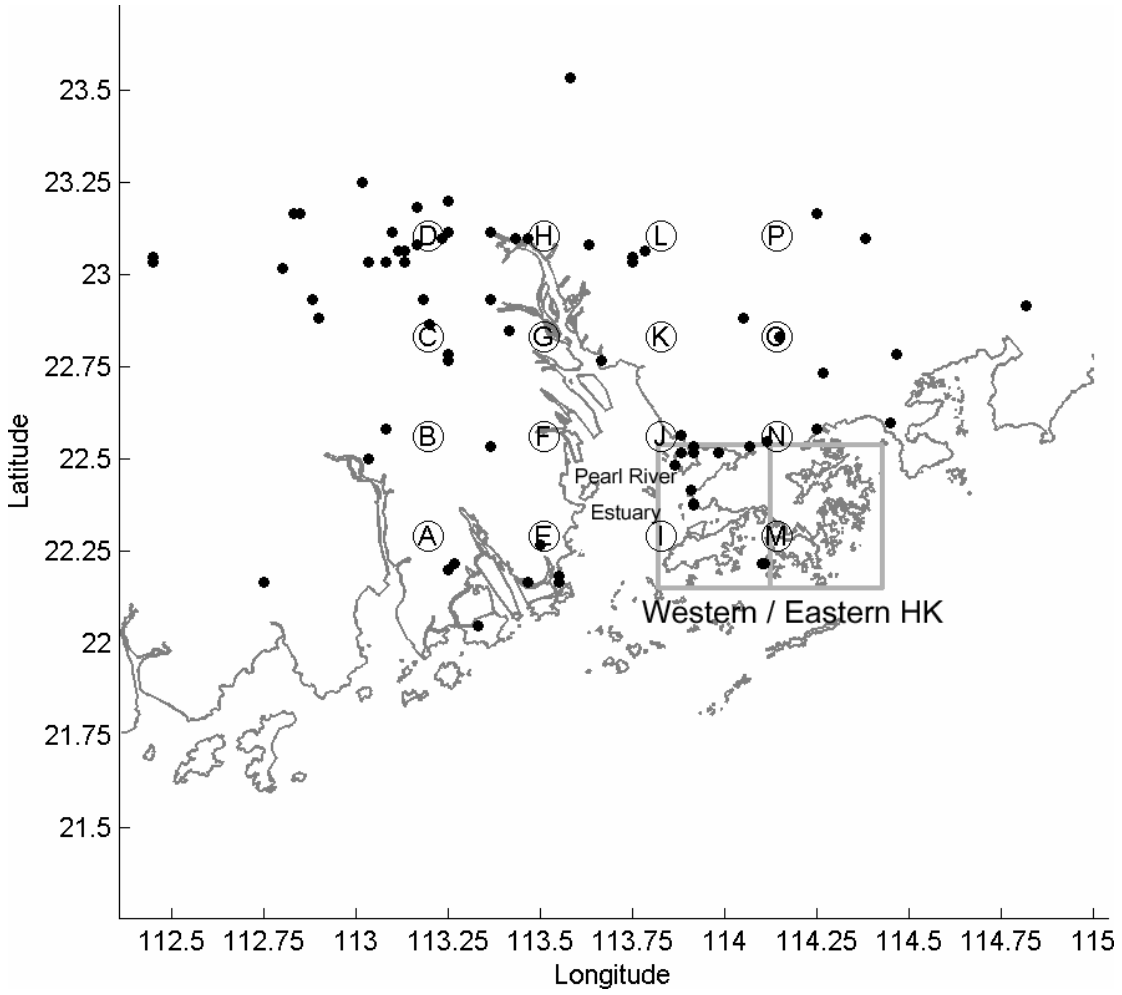

Figure 6-3: Map showing the 1-km MM5 domain, locations of the 4 x 4 emission sources (A-P), and extension of the two sampling zones in Hong Kong (grey boxes). Black dots indicate the location of power plants in PRD.

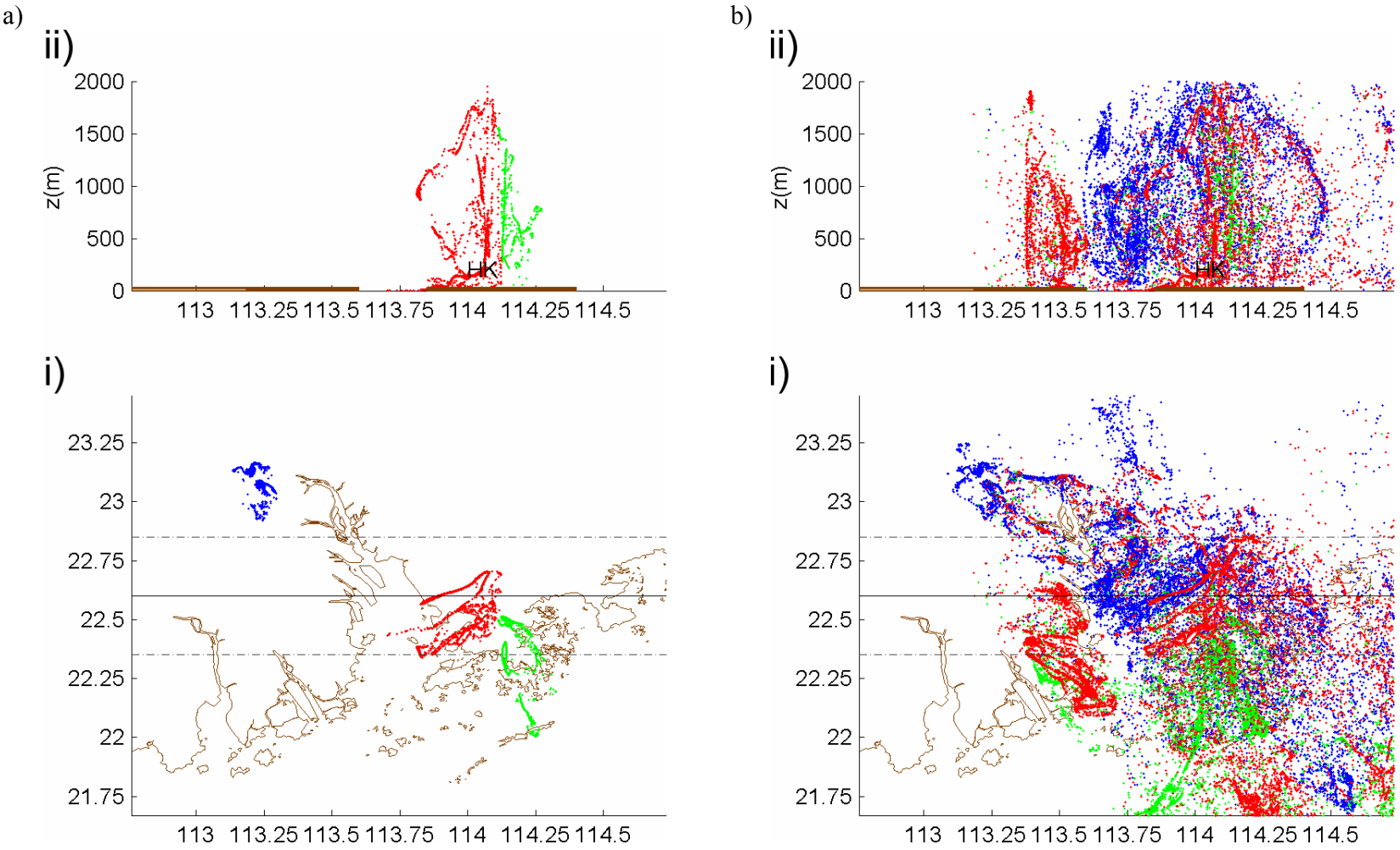

Figure 6-4: Particle-flow patterns at 1500 LST of a) first day, and b) third day simulation for the case of calm weather. Three ground level emission sources at 10 m AGL located at Guangzhou (sources D in Figure 6-3, blue color), Shenzhen (source J, red color), and Hong Kong (source M, green color) were used. Figure i) shows the horizontal cross section of the dispersion pattern. Figure ii) shows the west-east vertical projection on the black solid line with thickness 50 km as shown in the dashed line.

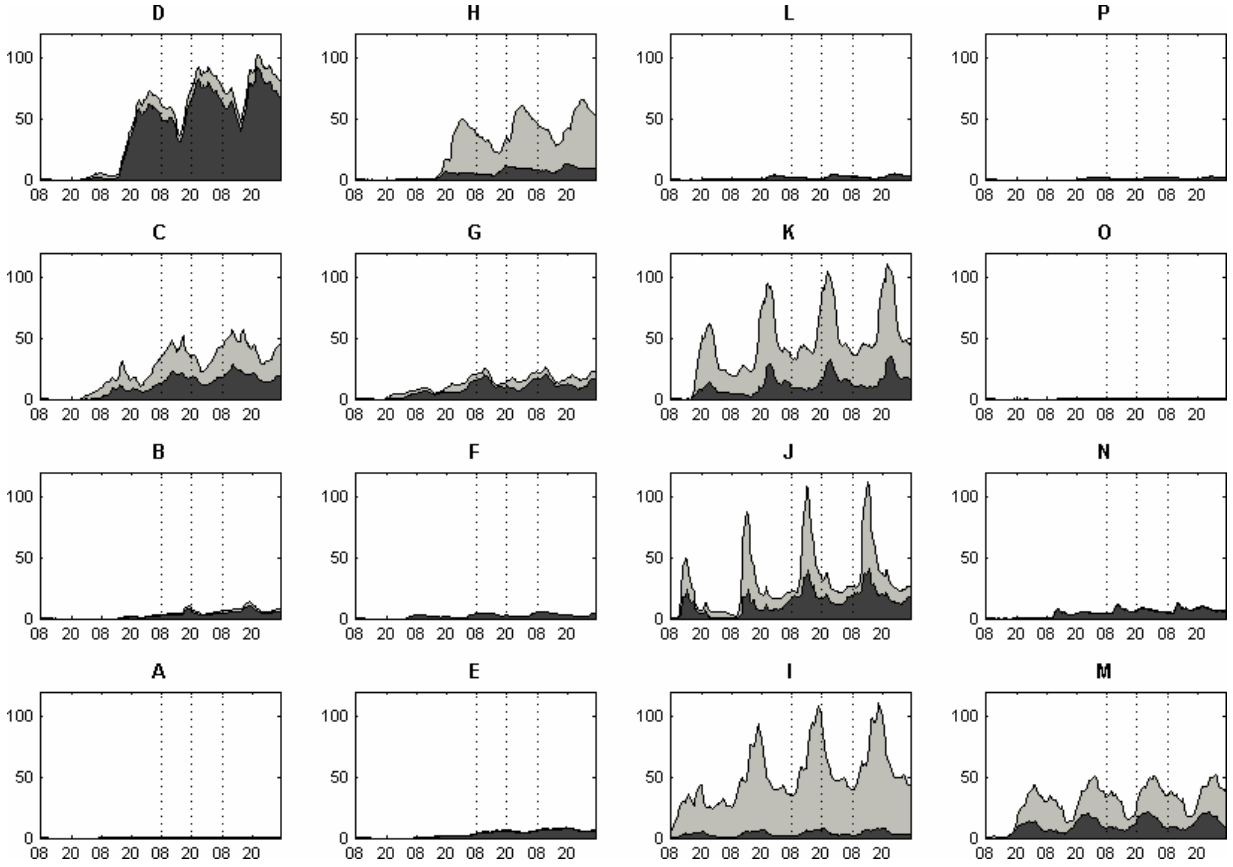

Figure 6-5: Time series of the contribution of surface emissions (dark grey) and power plant emissions (light grey) from the 16 sources to total RSP in the western Hong Kong during calm weather days. The title of each plot denotes the emission sources. x-axis is in LST. y-axis is the relative amount of RSP within the lower part of PBL (below 1 km MSL).

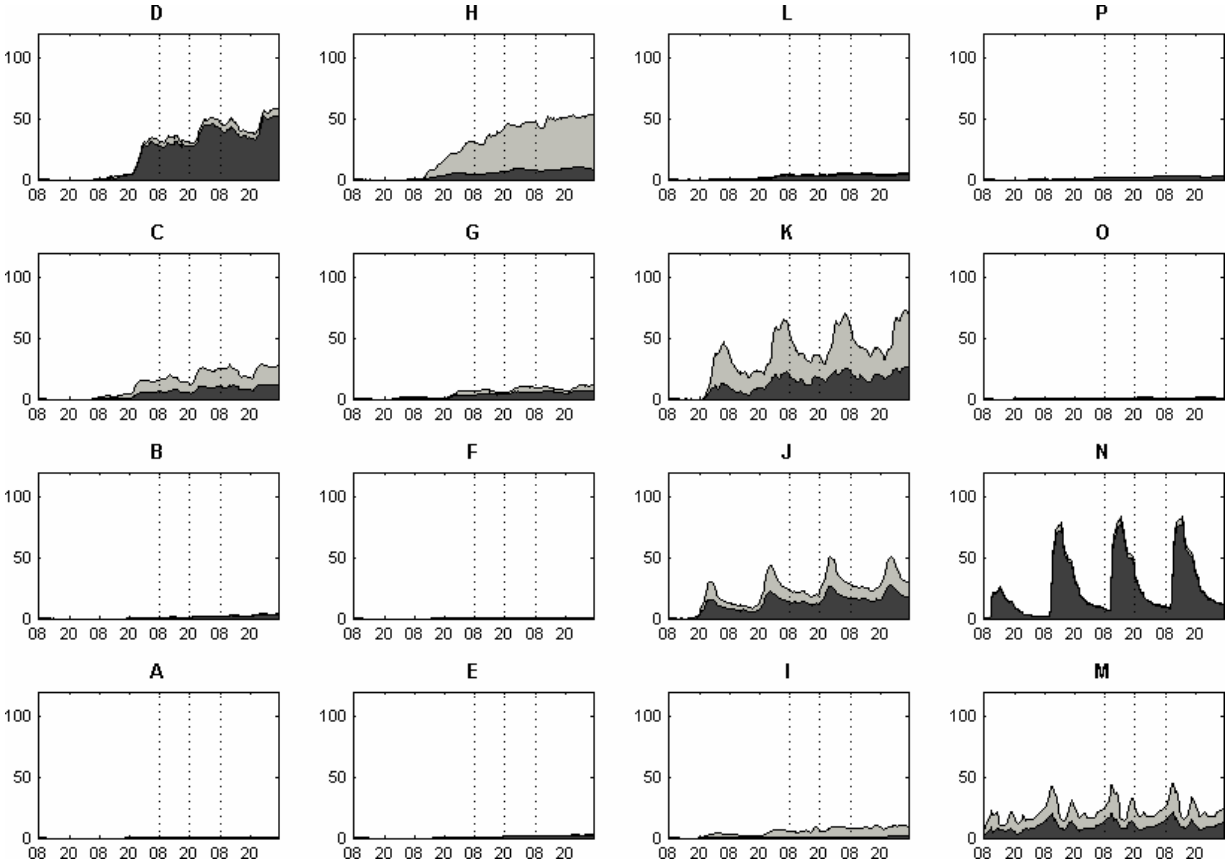

Figure 6-6: Same as Figure 6-5, but for eastern Hong Kong.

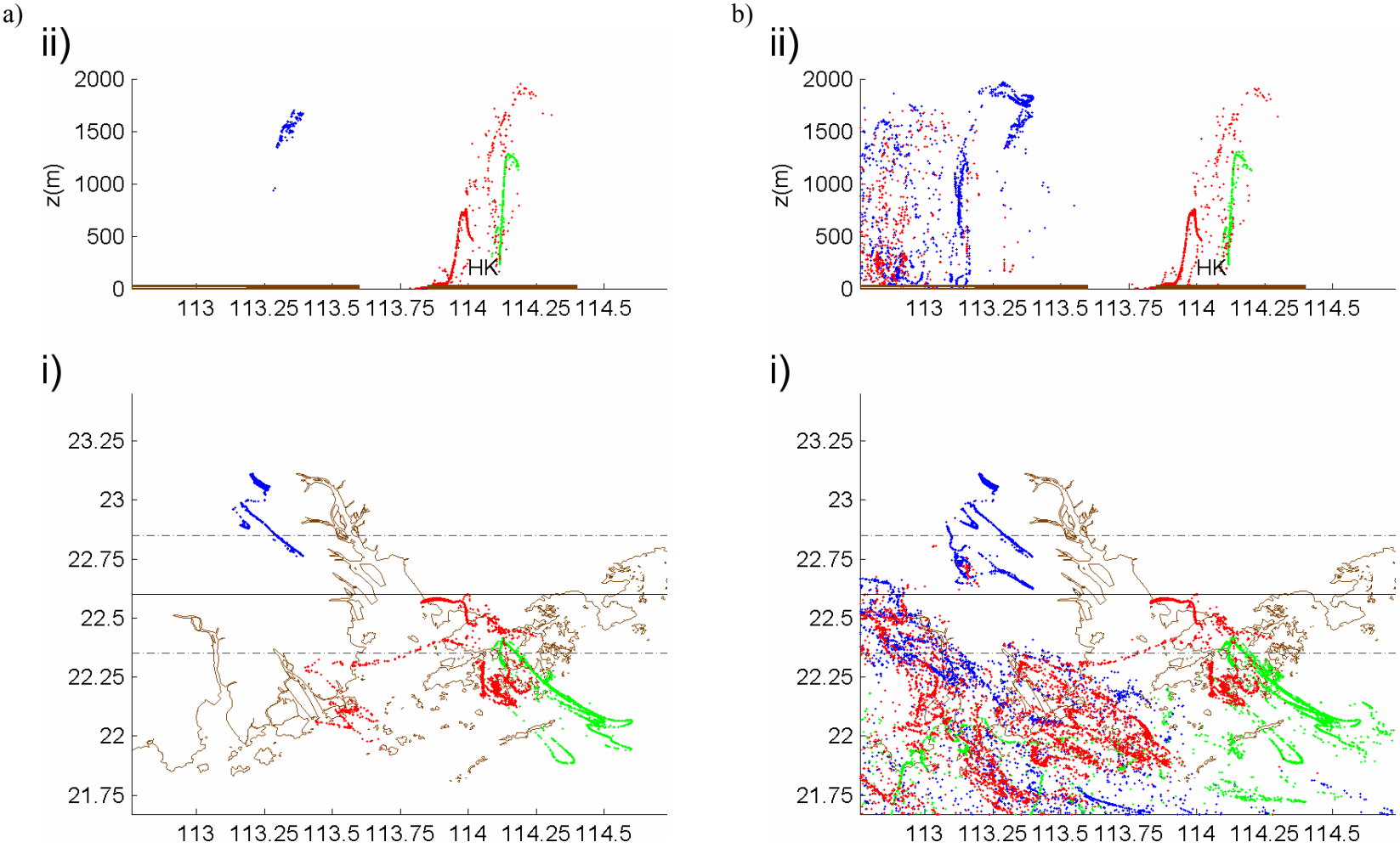

Figure 6-7: Same as Figure 6-4, but for the normal-day situation.

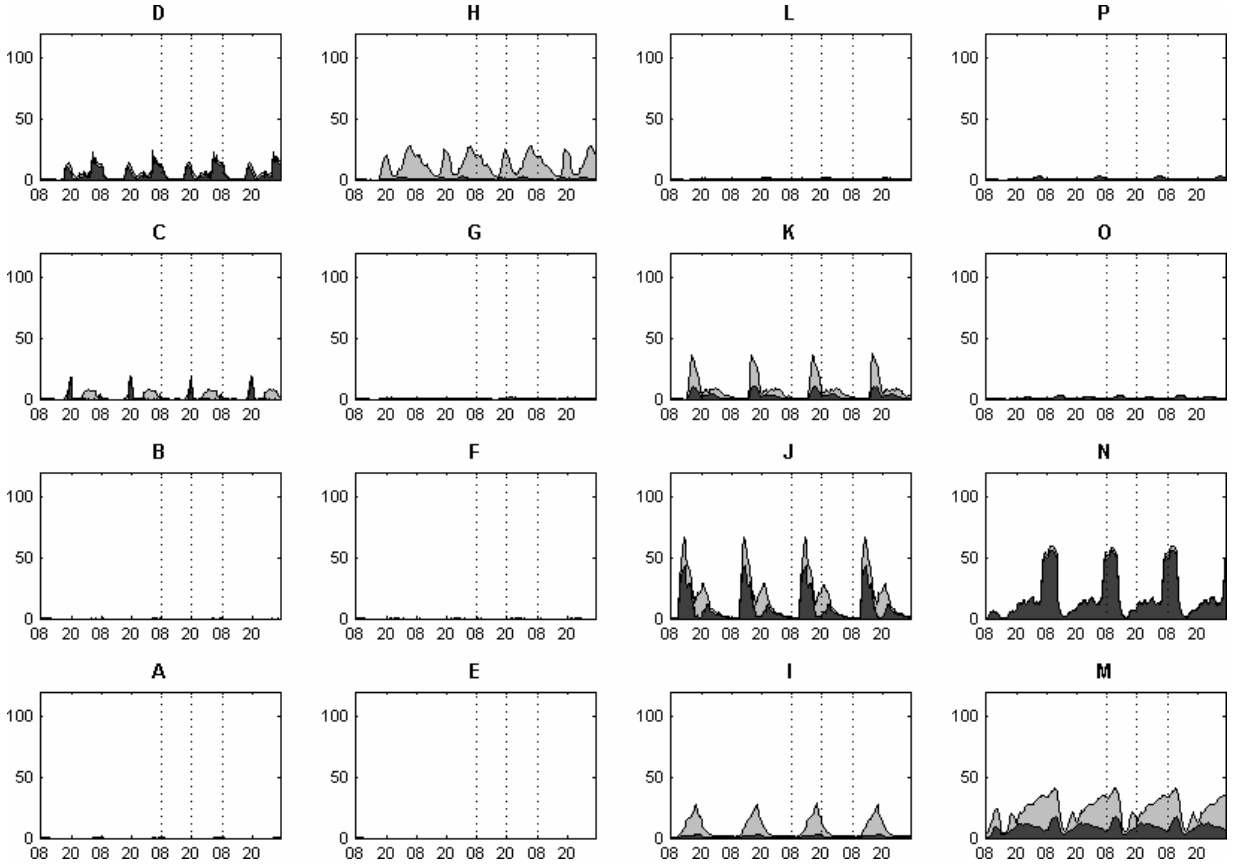

Figure 6-8: Same as Figure 6-5, but for the normal-day situation.

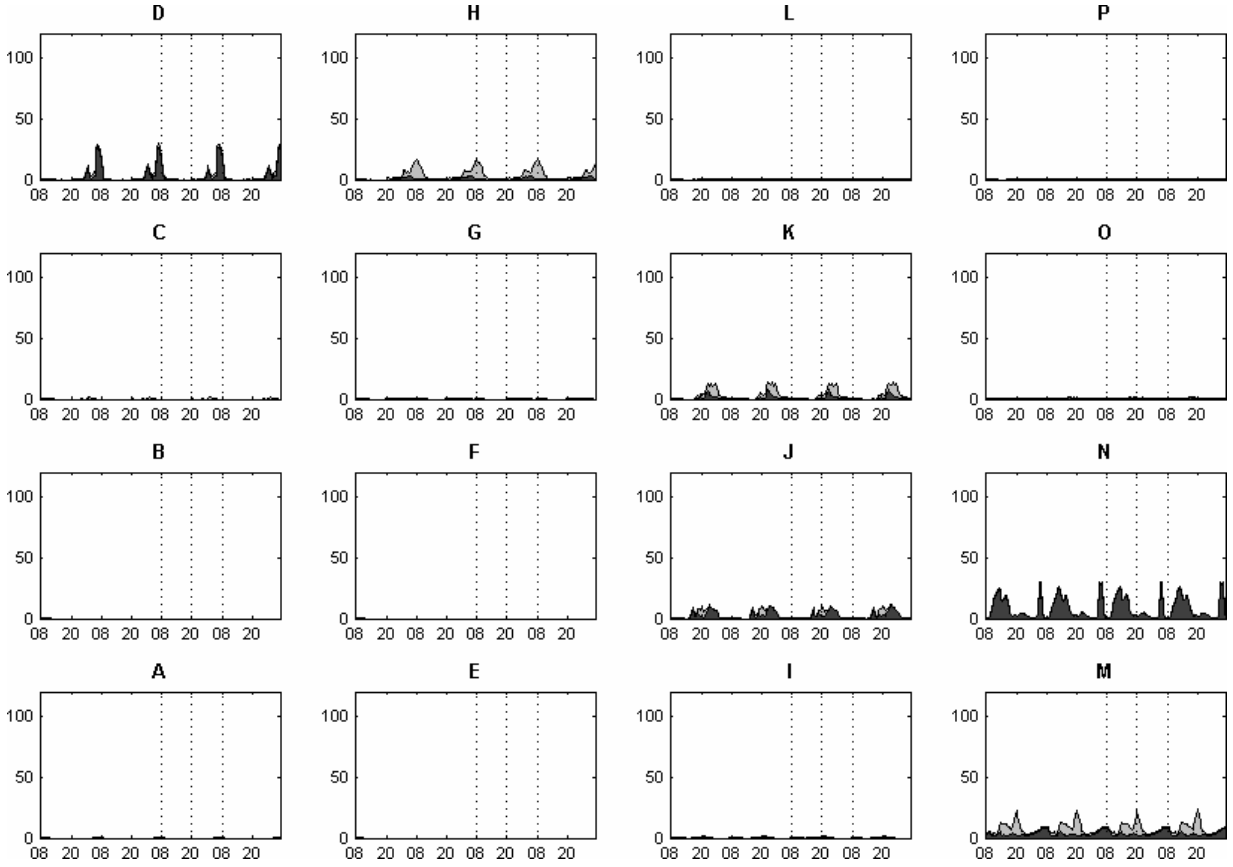

Figure 6-9: Same as Figure 6-5, but for eastern Hong Kong during the normal-day situation.

Table 6-1: MM5 domain configurations and physics options.

Domain dimensions	300 x 300
Grid size	1 km
Vertical layers	35 (about 12 layers below 1 km AGL)
Cumulus Scheme	None
Moisture scheme	Simple ice scheme
PBL scheme	MRF scheme
Radiation scheme	RRTM longwave scheme
Land surface scheme	Noah LSM

Table 6-2: Weighting factor (WF) of the 16 emission sources for surface and power plant (blanketed values) PM emission.

Source	WF	Source	WF	Source	WF	Source	WF
D	26.0 (0.75)	H	4.00 (4.38)	L	1.99 (0.21)	P	1.92 (0.02)
C	7.60 (1.03)	G	4.02 (0.10)	K	6.56 (1.51)	O	1.28 (0.03)
B	6.75 (0.59)	F	1.81 (0.00)	J	12.7 (1.65)	N	6.41 (0.13)
A	0.99 (0.36)	E	3.01 (0.05)	I	0.57 (0.89)	M	2.01 (0.64)
Total	87.7 (12.3)	M_{PM}	0.15				

Table 6-3: Same as Table 2 but for SO_2 emission.

Source	WF	Source	WF	Source	WF	Source	WF
D	10.54 (4.39)	H	1.39 (17.09)	L	0.44 (0.45)	P	0.75 (0.00)
C	2.53 (8.04)	G	1.19 (1.35)	K	2.26 (14.7)	O	0.28 (0.43)
B	2.40 (1.94)	F	0.55 (0.00)	J	5.37 (8.44)	N	2.59 (0.39)
A	0.23 (0.16)	E	1.09 (0.22)	I	0.12 (5.9)	M	0.03 (4.74)
Total	31.8 (68.2)	M_{SO}	0.53				

Table 6-4: Same as Table 2 but for NO_X emission.

Source	WF	Source	WF	Source	WF	Source	WF
D	12.37 (2.56)	H	2.63 (12.14)	L	1.25 (0.41)	P	0.57 (0.02)
C	3.78 (6.42)	G	1.86 (0.97)	K	3.5 (12.37)	O	0.87 (0.11)
B	2.47 (1.39)	F	0.74 (0.00)	J	7.53 (4.07)	N	4.25 (0.33)
A	0.68 (0.12)	E	1.91 (0.19)	I	1.25 (5.65)	M	4.58 (2.98)
Total	50.3 (49.7)	M_{NO}	0.32				

Table 6-5: Ratio of secondary sulfate and nitrate to primary pollutants in Hong Kong by observational measurements and the derived gas-to-particle conversion rates.

Measurements	Conversion Rates
SO_4/PM = 0.96	R_S = 0.29
NO_3/PM = 0.45	R_N = 0.24

Table 6-6: Total amount of RSP in western and eastern Hong Kong over the RSP in entire Hong Kong and pollution levels in entire Hong Kong during different meteorological conditions.

Synoptic Condition	Western HK	Eastern HK	Pollution Level
Calm	60.4%	39.6%	1
Normal-day	75.3%	24.7%	0.28

Table 6-7: Contribution of local and regional pollution sources of RSP totals to Hong Kong during calm meteorological condition.

Calm	Surface emissions	Power plant emissions	Total
Regional transport	45.6%	32.5%	78.1%
Local production	5.6%	16.3%	21.9%
Total	51.2%	48.8%	100%

Table 6-8: Same as Table 6-7 but for normal-day meteorological condition.

Normal-day	Surface emissions	Power plant emissions	Total
Regional transport	44.4%	26.2%	70.6%
Local production	11.0%	18.4%	29.4%
Total	55.4%	44.6%	100%

Chapter 7 A Cautionary Note on the Resolution of Meteorological Fields for Backward Trajectory Analysis in Hong Kong

7.1 Introduction

Trajectories are defined as the paths followed by air masses with time. It can be calculated from observed wind data or from simulated wind fields from numerical models. In air quality study, trajectories analyses are frequently used to determine the source regions of air pollutants over the world. Trajectories can be performed forward or backward in time. Forward trajectories are calculated by specifying initial locations and time and then tracing the air masses with increasing time and determine their final positions. Backward trajectories are calculated by final air mass locations and time then tracing the air masses with decreasing time to find out their origins.

Hong Kong, located in the southeast part of the Pearl River Delta (PRD) region, is a mega city of 1100 km^2 area containing 7 million people. In the past decades, because of the rapid economic and population growth, the air quality is deteriorating, both in Hong Kong and the entire PRD region. As a result of the raise of public concerns, air quality study has been becoming a hot research subject in the region. Among the air quality studies over Hong Kong, backward trajectories analyses are the most frequently used methodology to identify source regions of pollutants in Hong Kong both within the planetary boundary layer (PBL) (e.g. see Table 7-1), and the upper-level troposphere (e.g. Chan et al. 1998; Liu et al., 1999; Chan et al. 2001, 2002, 2003a, 2003b, 2004; Lee et al. 2004; Oltmans et al., 2004). In the previous studies, the model from the Climate

Monitoring and Diagnostics Laboratory (CMDL) of the US National Oceanic and Atmospheric Administration (NOAA) (Harris and Kahl, 1994) and the hybrid single-particle Lagrangian integrated trajectories (HYSPLIT) model (Draxler, 1988; Draxler and Rolph, 2003) were the most common models used to perform trajectories analyses. The spatial resolutions of meteorological fields used were relatively coarse, of which, wind fields from spatial resolution of 2.5° x 2.5° European Center for Medium Range Weather Forecast (ECMWF) reanalysis data, 2.5° x 2.5° National Center for Environmental Prediction (NCEP) global analyses, and 1° x 1° NCEP final analysis (FNL) data were most frequently used to calculate the trajectories.

Geographically, Hong Kong and the PRD is a highly urbanized region with mountainous terrain and complex coast. The local atmospheric circulations, such as land-sea breeze circulation (LSBC), mountain valley circulation (MVC) as well as urban heat island circulation (UHIC), have a significant influence on air flow pattern and affect the pollutants trajectories over the region (Fung et al. 2005; Huang et al. 2005; Lo et al. 2006a, 2006b, 2006c). Within the PBL where this chapter focuses on, the meteorological condition is highly depended on local land-surface characteristics, e.g. terrain, land-use and soil parameters. A question has been raised whether the coarse spatial wind fields can capture these local circulations and the accuracy of the corresponding trajectories analyses.

Utilizing the HYSPLIT model, 48-hr backward trajectories were calculated to find out the origins of the pollutants during a pollution episode over Hong Kong on 26-29 September 2004. In order to investigate the uncertainties of different spatial resolution wind fields on the trajectories calculations, the HYSPLIT was configured

with six sets of different wind fields. One set was provided by 1° x 1° NCEP FNL data. The other four sets were given by 27, 9, 3, and 1-km MM5 simulations coupled with the Noah land surface model (LSM), which has bulk urban land-use treatments along with a detailed PRD land-use map. The last set of wind fields was given by 1-km MM5 simulations with the default United States Geological Survey (USGS) land-use map to explore the sensitivity of uncertainty on the backward trajectories analyses.

7.2 Configurations of Meteorological Model MM5

The meteorological model used was the non-hydrostatic MM5 version 3.6.3 (Dudhia, 1993; Grell et al., 1994). Figure 7-1 shows the four two-way interactive nested domains with spatial resolutions of 27 (D1, mesh size of 175 x 130), 9 (D2, mesh size of 151 x 130), 3 (D3, mesh size of 154 x 145) and 1 km (D4, mesh size of 322 x 280). The outermost 27-km domain covers the East Asia and China is designed to capture the synoptic-scale features while the innermost 1-km domain covers Hong Kong and PRD is designed to resolve local scale circulation features. Thirty five full sigma-levels from surface to 100 hPa were used, of which the lowest twelve levels are below 1 km in order to have a finer resolution of the PBL. 60-hr simulation was set from 0800 LST 27 to 2000 LST 29 September 2004.

The MM5 runs were initialized using the 1° x 1° NCEP FNL data as first guess fields. The lateral boundary conditions of the outermost domain were obtained by linearly interpolating 6-hourly FNL data. Upper air and surface observations available on the Global Telecommunication System (GTS) were used to enhance MM5 initial and boundary conditions. Analysis nudging of wind fields was employed in the upper levels

of the two outer domains (D1 and D2) to improve the accuracy of the simulations. Detailed physics schemes used in the simulations are listed in Table 7-2.

Two sets of MM5 experiments were conducted. The first experiment used the new PRD land-use dataset provided by Hong Kong Planning Department (HKPD) in 2003 (see Lo et al 2005a, Figure 3b). The second experiment was carried out by using the default 30-second-resolution USGS land-use map (see Lo et al 2006a, Figure 3a). All these two experiments are conducted identically except the land-use map.

7.3 Spatial Variations of Wind Fields

In trajectories calculations, it is no doubt that wind fields are the fundamental parameters to control the analysis result. However, within the PBL, where the air flow is significantly influenced by the local surface characteristics, the wind fields given from different spatial resolution simulations can be quite large. Figure 7-2 shows the surface wind fields over PRD region at 1500 LST 29 September 2004 given by 1° x 1° NCEP FNL reanalysis and five sets of MM5 simulated wind fields.

From the FNL data (Figure 7-2a), the prevailing wind is northeasterly with a very smooth air stream over the PRD. The air flow in the 27-km MM5 simulation (Figure 7-2b) was similar to FNL except the southerly wind in the western PRD. The afternoon sea-breeze circulation (SBC) was generated along the southern China seashore (Figure 7-2c) until the domain resolution came down to 9 km. From the 3-km D3 simulation (Figure 7-2d), the feature of the sea breeze circulation was more clearly displayed. The sea breeze was not just occurred along the southern China seashore, but also generated along the Pearl River coast. From the ultimate 1-km D4 (Figure 7-2e), the

SBC structure was much more prominent. The SBC interacted with MVC as well as UHIC forming some complex local circulations. The air stream in the inland domain became much more convective and turbulent. These fine structures local circulations certainly cannot be captured by the synoptic-scale (FNL or 27-km D1) wind fields. Comparing Figure 7-2e and 7-2f, the 1-km-resolution wind fields given by the two different land-use maps seem have not many differences in this time slot.

7.4 Uncertainties of Trajectories Calculations

We have just seen in last section that the variants of wind fields can be quite large for different spatial resolutions simulations. In this section, 48-hr backward trajectories end at 1500 LST 29 September 2004 were calculated, using these six sets of wind fields, to find out the source regions of the air masses in the pollution episode in Hong Kong. The Hong Kong international airport (HKIA; 22.31°N, 113.92°E) was specified as the final location. Two altitudes were set in HKIA; one was set at 100 m, represented ground level receptor, the other was located at 1 km which represented upper-level PBL receptor. If the air masses run out the domain extension during the trajectories calculations, wind fields provided by the mother domain were used until the 48-hr calculations finished.

Figure 7-3 shows the 48-h backward trajectories calculated from the six sets of wind fields. From the trajectories calculated by the FNL data, the path of the air mass mainly followed the northeasterly continental air-stream. The vertical positions of the air mass did not change much because the flows of the synoptic-scale FNL wind fields are mainly geotropic; the vertical motion of the air mass was not well presented.

As mentioned earlier in the last section, the local circulations were more prominent when the domain resolution increased. These local circulations have a significant impact on the trajectories calculations both in horizontal and vertical direction and thus caused large uncertainties of the path as well as the origin of the air mass, as demonstrated in Figure 7-3.

Table 7-3 summarizes the uncertainties of the origins of the 48-hr trajectories calculations given by the six sets of wind fields. Comparing the trajectories origin given from the coarser resolution wind fields with that from the finest 1-km simulation, the differences ranged from 169 km to 238 km. By applying the wind fields given from the USGS land-use experiment, the difference can reach 150 km. This result indicates one disadvantage of the backward trajectories calculations: the calculation is very sensitive to the wind field, although the air flows are very similar at the initial (see Figure 7-2e and Figure 7-2f), these little variance accumulate in each time step of calculation, and finally caused a 150-km difference after the 48-hr calculation.

Figure 7-4 shows the 48-hr backward trajectories for the location at 1 km and the corresponding uncertainties of the origins is summarized in Table 7-4. At upper level of the PBL (1 km AGL), the trajectories were still very sensitive to the resolution of the wind fields. The differences of the air mass origins ranged from 135 km to 244 km.

7.5 Conclusions

Backward trajectories calculated from the high resolution MM5 simulated winds demonstrate large uncertainties in their behavior when comparing calculations using the coarse resolution wind fields. This result indicates that care must be taken on choosing

the suitable resolution of wind fields when calculating trajectories for diagnostic studies. For the situation over PRD or Hong Kong, local circulations play an important role on air flow and it cannot be neglected when calculating the trajectories. As pointed out by Lo et al. (2006a), the local circulation can affect the meteorological conditions up to 2-km AGL in the PRD. Thus, if the trajectory analyses are performed within this altitude, a fine resolution simulation domain (1 km to 3 km) as well as an accurate presentation of the local land-surface characteristics should be applied.

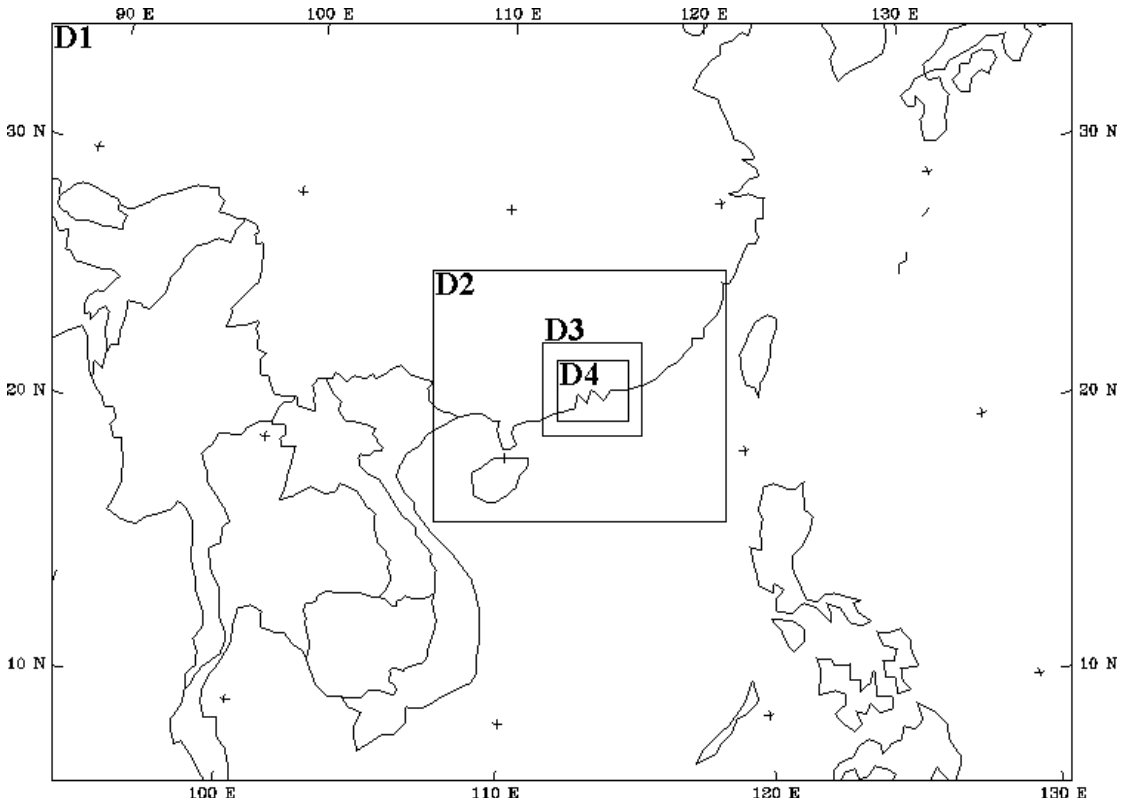

Figure 7-1: Configuration of the four two-way nested domains for MM5 simulations. Grid sizes of the domains are 27, 9, 3 and 1 km.

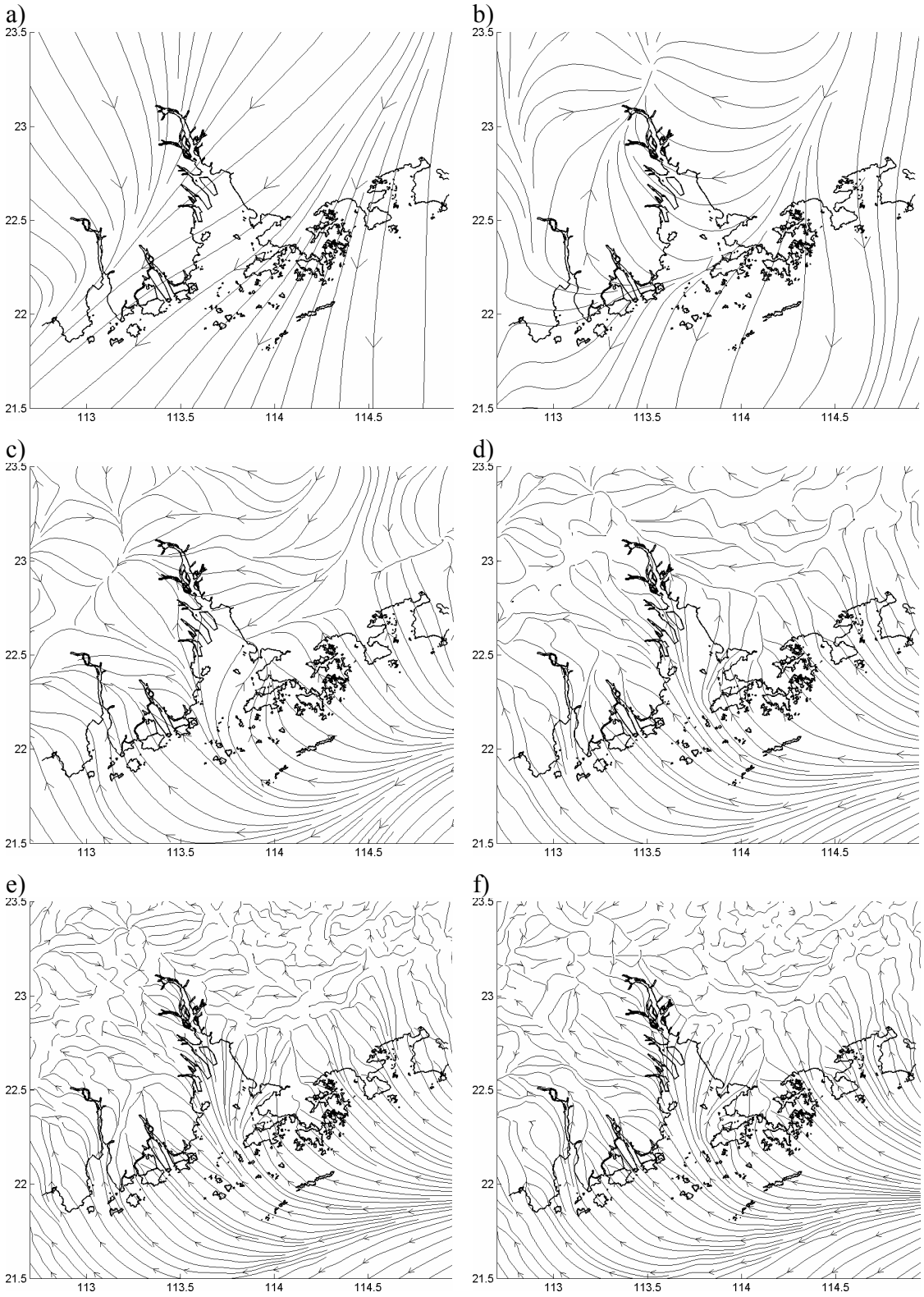

Figure 7-2: Surface wind stream over PRD valid at 1500 LST 29 September 2004 given by a) 1° FNL, MM5 simulations with the 2003 land-use map of spatial resolution b) 27, c) 9, d) 3, e) 1 km and f) 1-km MM5 simulation with the default USGS land-use map.

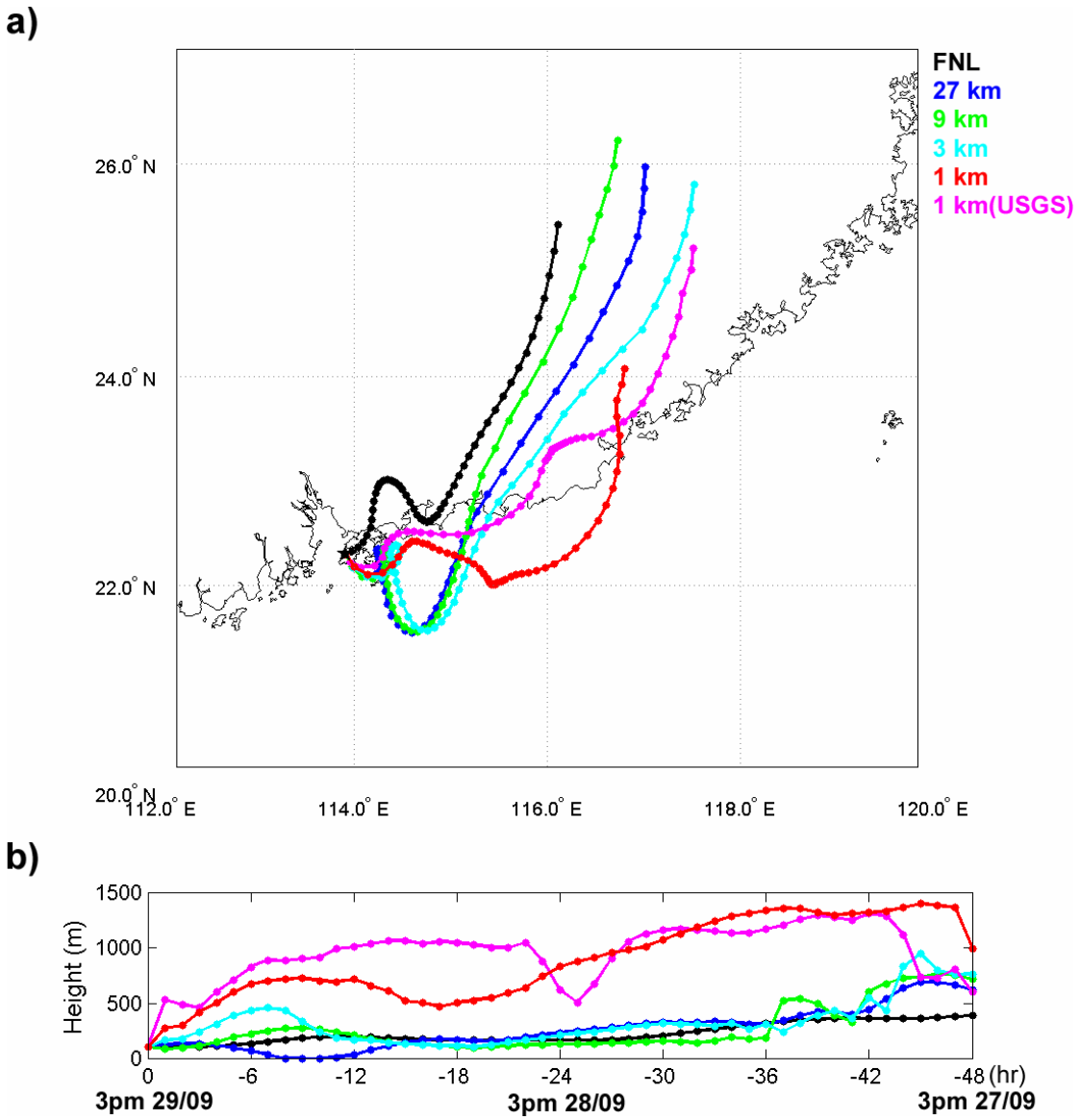

Figure 7-3: 48-hr backward trajectories (every 1h) calculated by the six sets of wind fields. a) Horizontal projection and b) vertical projection. The end point was set at 100 m AGL at HKIA.

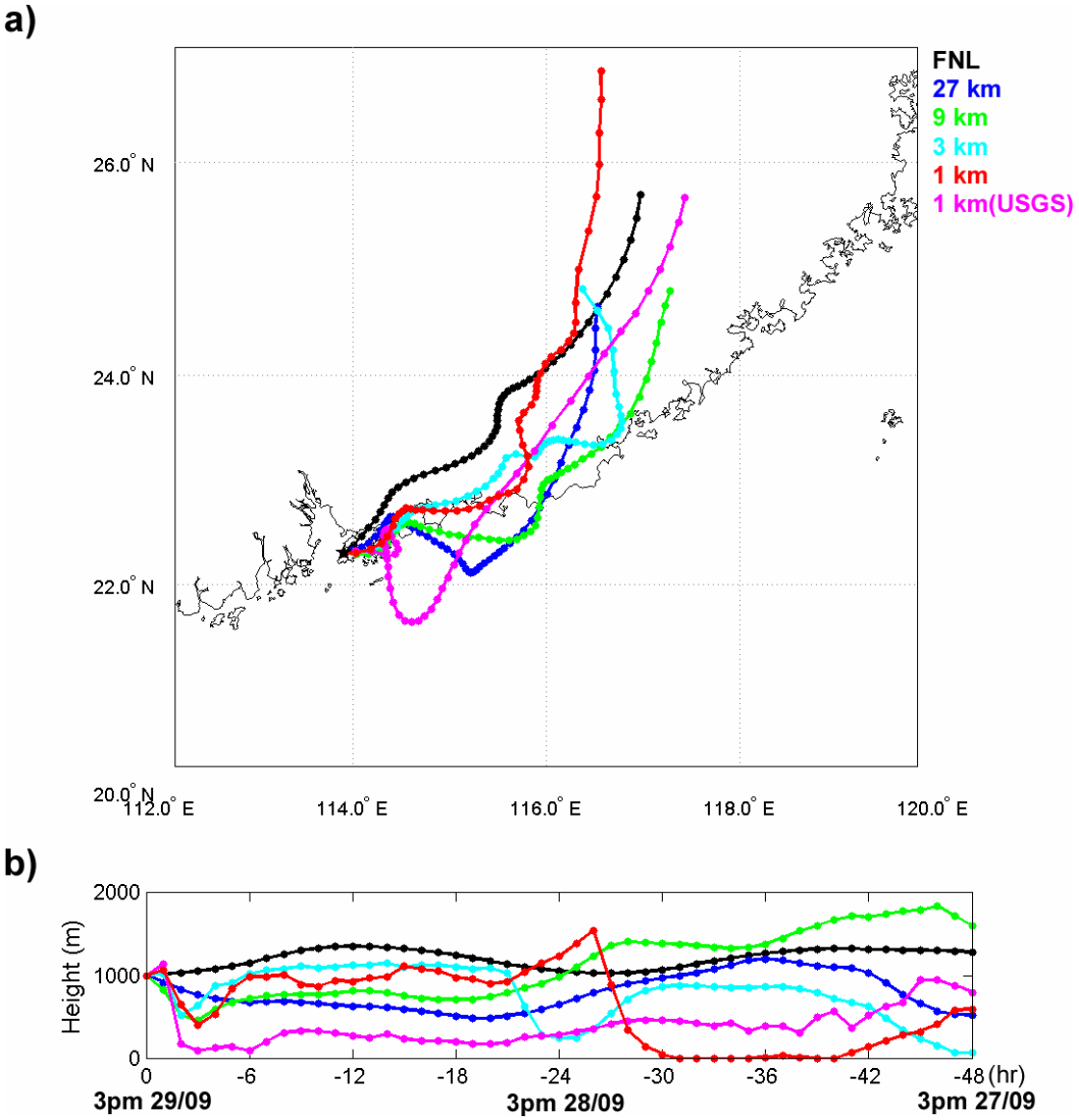

Figure 7-4: Same as Figure 7-3 but for the end point at 1 km AGL.

Table 7-1: Configurations of previous studies on backward trajectories analyses within the PBL in Hong Kong

Publication	**Model used**	**Duration**	**Final position height**	**Data used**
Fang et al. (1999)	Vis5D	72 hrs	Surface	54 km MM5
Lam et al. (2001)	NOAA-CMDL	10 days	1000 m	2.5° ECMWF
Wang et al. (2001)	NOAA-CMDL	10 days	500 m	2.5° ECMWF
Lee et al. (2002)	NOAA-CMDL	72 hrs	850 hPa	2.5° NCEP
Lee et al. (2003)	NOAA-CMDL	10 days	850, 900 and 950 hPa	2.5° ECMWF
Pathak et al. (2003)	HYSPLIT	72 hrs	500 m	1° FNL
Ding et al. (2004)	HYSPLIT	12 hrs	Surface	3 km MM5
Lam et al. (2005)	HYSPLIT	72 hrs	10, 100, 500 and 1000 m	2.5° NCEP
Louie et al. (2005)	HYSPLIT	72 hrs	1000 m	1° FNL

Table 7-2: Domain configurations and physics options used in the experiments.

	D1	**D2**	**D3**	**D4**
Domain dimensions (x, y)	175 x 130	151 x 130	154 x 145	322 x 280
Grid size	27 km	9 km	3 km	1 km
Vertical layers	35 (about 12 layers below 1 km AGL)			
Cumulus scheme	Grell scheme for D1 and D2, None for D3 and D4			
Moisture scheme	Simple ice scheme			
PBL scheme	MRF scheme			
Radiation scheme	RRTM longwave scheme			
Land surface scheme	Noah LSM			

Table 7-3: Inter-comparisons of uncertainties (km) of the 48-hr backward trajectories origins arrived Hong Kong at 100 m AGL at 1500 LST 29 September, 2004.

Differences (km)	FNL	27 km	9 km	3 km	1 km	1 km (USGS)
FNL	0	116	110	162	169	158
27 km	116	0	42	60	212	101
9 km	110	42	0	99	238	142
3 km	162	60	99	0	209	66
1 km	169	212	238	209	0	150
1 km (USGS)	158	101	142	66	150	0

Table 7-4: Same as Table 7-3 but for the location at 1 km AGL.

Differences (km)	FNL	27 km	9 km	3 km	1 km	1 km (USGS)
FNL	0	127	105	118	135	51
27 km	127	0	85	25	244	152
9 km	105	85	0	101	241	98
3 km	118	25	101	0	226	151
1 km	135	244	241	226	0	162
1 km (USGS)	51	152	98	151	162	0

Chapter 8 Conclusions and Recommendations

This study investigated the features and mechanisms of the local scale atmospheric circulations, and their influences on pollutant transport and air quality over the PRD region, which is one of the most rapid economic-developing, but environment-deteriorating regions in the southern China. Four numerical models were involved in this research, including: a fine-scale, advanced mesoscale meteorological model MM5 coupled, an advanced land surface model Noah LSM, a simple particle transportation model, and a simple air parcel trajectory model HYSPLIT.

In Chapter 4, a localized mesoscale meteorological land surface/urban modeling system for the PRD region has been developed and evaluated. Three approaches of land surface treatments were used to examine the evolution of local and regional land-sea breeze circulation in Hong Kong and PRD. In the current MM5, the 1993-based USGS land-use data underestimated the urban areas coverage in the rapidly developing PRD. Using this MM5 default land-use map and a simple slab land model, MM5 generated a weak sea breeze circulation due to insufficient land surface forcing over urban areas. Moreover, a large temperature cold bias is found because of unrealistic land-use distribution. By applying an up-to-date land-use map with slab model, MM5 performed better in capturing the afternoon sea breeze patterns. However, this set of experiment still cannot simulate the observed urban heat island in the region. By contrast, using the MM5/Noah LSM, along with the up-to-date land-use map and enhancements of urban land-use treatment, it was able to capture major features of the observed surface temperature and wind-flow patterns in the PRD.

The role of urbanization on the meteorological conditions was then investigated. It demonstrated that the stronger urban heat island in the PRD increased the differential temperature gradient between urbanized areas and the nearby ocean surface, and hence enhanced the mesoscale sea breeze circulation. Through the sensitivity studies, results showed that further urbanization, with higher sensible heat fluxes, the temperature in the lowest 2-km atmosphere over the PRD can increase by about 1.5°C.

There are two refinements recommended of the MM5/Noah LSM urban modeling system for further investigation, including, 1) addition of anthropogenic heat source in the model physics; 2) divide the one-category urban land-use into further finer categories and accompany with different sets of physical parameterization in the urban model. For the model initialization, a spinup of the land surface states, including, soil moisture/water content and soil temperature, can provide an alternative approach to initializing from the coarse resolution AGRMENT dataset. Also, the 1-km fine-resolution sea surface temperature from MODIS is recommended to replace the 1-degree FNL data from NCEP. In addition, the experiments conducted are for a single case (a single 36 hour period) only. It can only reflect the situation in a weak synoptic background winds but not be necessary reflect the general phenomenon. In order to make the conclusions more definitively, further study would need to conduct many more simulations, perhaps over seasons and years.

In Chapter 5, utilizing the localized MM5/Noah LSM urban modeling system coupled with a three-dimensional particle trajectory model, the pollutant transport mechanism influenced by the local and regional atmospheric circulations over the PRD

was studied. Numerical experiments were conducted to explore the structure of the Pearl River Delta Circulation Zone (PRDCZ).

A conceptual model has been established to explain the mechanism of pollutant trapping over the PRDCZ. Results suggested that pollutants emitted in the cities besides the PRDCZ were trapped by the sea breeze circulation and well-mixed within the lower part of the atmosphere. The research showed that the amount of pollutants accumulated when the sea breeze is dominant over the coastal zone and the land breeze generally helps to clean the pollutants away from the coastal cities.

The urbanization effects on the pollutant transport have also been examined. Urban sprawl hinders air pollution dispersion in the PRD. In the afternoon, urbanization strengthens the sea breeze circulation and more pollutants are trapped and brought to coastal zones. During the night and early morning, an urban heat island effect weakens the land breeze and creates circulation convergence zones causing the nocturnal pollutants trapping and early morning pollutants to accumulate. With the same weak wind speed frequency, the probability of pollutant trapping in the current PRD is much higher than two decades ago. For further investigation, the seasonal variation of the structure of the PRDCZ and its associated pollutant transport and trapping is an interesting subject to be addressed. Also, validation from observational measurement is an important step to confirm the conceptual model.

In Chapter 6, a new methodology was used to evaluate the contribution of source regions of RSP. The results demonstrated that major pollution sources over Hong Kong come from regional transport. A physical modeling approach was used to calculate two chemical gas-to-particle conversion rates for SO_2 to sulphate (R_S=0.29) and NO_X to

nitrate (R_N=0.24). It is noted that these values are derived under the assumption that the conversion rates remained constant throughout the transport from emitter to receptor, which is a very crude approximation that should be further refined. In addition, these values could be sensitive to the emission data for primary pollutants. Nevertheless, although these two parameters are only roughly estimated in the present study, our results demonstrate conceptually the usefulness of these two parameters in deriving the ambient levels of secondary pollutants in air quality study. For a more accurate investigation, detailed and sophisticated atmospheric chemistry modeling would be required to estimate these two parameters, including their spatial and temporal variations.

In Chapter 7, backward trajectories calculated from the high resolution MM5 simulated winds demonstrate large uncertainties in their behavior when comparing calculations using the coarse resolution wind fields. This result shows that caution must be taken on choosing the suitable resolution of wind fields when calculating trajectories in diagnostic studies. For the situation over PRD or Hong Kong, local circulations play an important role on air flow and it cannot be neglected when calculating the trajectories. As pointed out by Chapter 4, the local circulation can affect the meteorological conditions up to 2-km AGL in the PRD. Thus, if the trajectory analyses are performed within this altitude, a fine resolution simulation domain (1 km to 3 km) as well as an accurate presentation of the local land-surface characteristics must be used.

References

Angevine, W. M., and K. E., Mitchell, 2001: Evaluation of the NCEP mesoscale Eta model convective boundary layer for air quality applications, *Mon. Wea. Rev.*, **129**, 2761-2775.

Athens, R. A., 1978: The height of the planetary boundary layer and the production of circulation in a sea breeze model. *J. Atmos. Sci.*, **35**, 1231-1239.

Berbery, E. H., 2001: Mesoscale moisture analysis of the North American monsoon, *J. Clim.*, **14**, 121-137.

Berbery, E. H., E. M., Rasmusson, and K. E., Mitchell, 1996: Studies of North American continental-scale hydrology using Eta model forecast products, *J. Geophys. Res.*, **101**, 7305-7319.

Berbery, E. H., K. E., Mitchell, S., Benjamin, T., Smirnova, H., Ritchie, R., Hogue, and E., Radeva, 1999: Assessment of land surface energy budgets from regional and global models, *J. Geophys. Res.*, **104**, 19329-19348.

Betts, A. K., F., Chen, K. E., Mitchell, and Z., Janjic, 1997: Assessment of the land surface and boundary layer models in the two operational versions of the NCEP Eta model using FIFE data, *Mon. Wea. Rev.*, **125**, 2896-2916.

Bornstein, R. D., 1968: Observations of the Urban Heat Island Effect in New York City. *J. Appl. Meteor.*, **7**, 575-582.

Bornstein, R. D., 1975: The two-dimensional URBMET urban boundary layer model. *J. Appl. Meteor.*, **14**, 1459-1477.

Braham, R. R., 1979: Comments on "Urban, Topographic and Diurnal Effects on Rainfall in the St. Louis Region". *J. Appl. Meteor.*, **18**, 371-374.

CH2M Hill (China) Limited, 2002: Study of air quality in the Pearl River Delta region; Commissioned by the Hong Kong Environmental Protection Department, HHSAR Government, April 2002. [Report available at http://www.epd.gov.hk/epd/english/environmentinhk/air/studyrpts/files/final_rept.pdf]

Chan, C. Y., et al., 2004: Vertical profile and origin of wintertime tropospheric ozone over China during the PEACE-A period. *J. Geophys. Res.*, **109**, doi:10.1029/2004JD004581.

Chan, C. Y., L. Y., Chan, J. M., Harris, S. J., Oltmans, D. R., Blake, Y., Qin, Y. G., Zheng, and X. D., Zheng, 2003a: Characteristics of biomass burning emission sources, transport, and chemical speciation in enhanced springtime tropospheric ozone profile over Hong Kong. *J. Geophys. Res.*, **108**, 4015, doi:10.1029/2001JD001555.

Chan, C. Y., L. Y., Chan, K. S., Lam, Y. S., Li, J. M., Harris, and S. J., Oltmans, 2002: Effects of Asian air pollution transport and photochemistry on carbon monoxide variability and ozone production in subtropical coastal south China. *J. Geophys. Res.*, **107**, 4746, doi:10.1029/2002JD002131.

Chan, C. Y., L. Y., Chan, W. L., Chang, Y. G., Zheng, H., Cui, X. D., Zheng, Y., Qin, and Y. S., Li, 2003b: Characteristics of a tropospheric ozone profile and implications for the origin of ozone over subtropical China in the spring of 2001. *J. Geophys. Res.*, **108**, 8800, doi:10.1029/2003JD003427.

Chan, C. Y., L. Y., Chan, Y. G., Zheng, J. M., Harris, S. J., Oltmans, and S., Christopher, 2001: Effects of 1997 Indonesian forest fires on tropospheric ozone enhancement, radiative forcing, and temperature change over the Hong Kong region. *J. Geophys. Res.*, **106**, 14875-14886, doi:10.1029/2001JD900092.

Chan, L. Y., H. Y., Liu, K. S., Lam, T., Wang, S. J., Oltmans and J. M., Harris, 1998: Analysis of the seasonal behavior of tropospheric ozone at Hong Kong. *Atmos. Environ.*, **32**, 159-168.

Changnon, S. A., Semonin, R. G., and Huff, F. A, 1976: A Hypothesis for Urban Rainfall Anomalies. *J. Appl. Meteor.*, **15**, 544-560.

Chen, F., and Dudhia, J., 2001: Coupling and advanced land surface-hydrology model with the Penn State-NCAR MM5 modeling system. Part I: Model implementation and sensitivity. *Mon. Wea. Rev.*, **129**, 569-585.

Chen, F., K. E., Mitchell, J., Schaake, Y., Xue, H.-L., Pan, V., Koren, Q. Y., Duan, M., Ek, and A., Betts, 1996: Modeling of land-surface evaporation by four schemes and comparison with FIFE observations, *J. Geophys. Res.*, **101**, 7251-7268.

Chen, F., Z., Janjic, and K. E., Mitchell, 1997: Impact of atmospheric surface-layer parameterizations in the new land-surface scheme of the NCEP mesoscale Eta model, *Bound.-Layer Meteor.*, **85**, 391-421.

Cosby, B. J., G. M., Hornberger, R. B., Clapp, and T. R., Ginn, 1984: A statistical exploration of the relationships of soil moisture characteristics to the physical properties of soils. *Water Resour. Res.*, **20**, 682-690.

Cuenca, R. H., M., Ek, and L., Mahrt, 1996: Impact of soil water property parameterization on atmospheric boundary-layer simulation. *J. Geophys. Res.*, **101**, 7269-7277.

Dickinson, R. E., 1984: Modeling evapotranspiration for three-dimensional global climate models. Climate Processes and Climate Sensitivity: Maurice Ewing Volume **5**, *Geophys. Monogr.*, No. 29, Amer. Geophys. Union, 58-72.

Ding, A. J., T., Wang, M., Zhao, T. J., Wang and Z. K., Li, 2004: Simulation of sea-land breezes and a discussion of their implications on the transport of air pollution during a multi-day ozone episode in the Pearl River Delta of China. *Atmos. Environ.*, **38**, 6737-6750.

Draxler, R. R., 1988: Hybrid single-particle Lagrangian integrated trajectories (HY-SPLIT): Model description. Report No. NOAA Technical Memorandum ERL ARL-166. National Oceanic and Atmospheric Administration, Silver Spring, MD.

Draxler, R. R., and G. D., Rolph, 2003: HYSPLIT (Hybrid Single-Particle Lagrangian Integrated Trajectory) Model access via NOAA ARL READY Website [http://www.arl.noaa.gov/ready/hysplit4.html]. NOAA Air Resources Laboratory, Silver Spring, MD.

Dudhia, J., 1993: A nonhydrostatic version of the Penn State-NCAR Mesoscale Model: Validation tests and simulation of an Atlantic cyclone and cold front. *Mon. Wea. Rev.*, **121**, 1493-1513.

Dudhia, J., 1996: A multi-layer soil temperature model for MM5. Preprints, Sixth PSU/NCAR Mesoscale Model Users' Workshop, Boulder, CO, NCAR, 49-50.

Ek, M. B., K. E., Mitchell, Y., Lin, E., Rogers, P., Grunmann, V., Koren, G., Gayno, and J. D., Tarpley, 2003: Implementation of Noah land surface model advances in the National Centers for Environmental Prediction operational mesoscale Eta model, *J. Geophys. Res.*, **108**, doi:10.1029/2002JD003296.

Ek, M., and L., Mahrt, 1991: OSU 1-D PBL model user's guide. Version 1.04, 120 pp. [Available from Department of Atmospheric Sciences, Oregon State University, Corvallis, OR 97331-2209.]

Fang, M., M., Zheng, F., Wang, K. S., Chim, and S. C., Kot, 1999: The long-range transport of aerosols from northern China to Hong Kong–a multi-technique study. *Atmos. Environ.*, **33**, 1803-1817.

Fung, J. C. H., A. K. H., Lau, J. S. L., Lam, and Z., Yuan, 2005: Observational and modeling analysis of a severe air pollution episode in western Hong Kong. *J. Geophys. Res.*, **110**, D09105, doi:10.1029/2004JD005105.

Gou, Y. R., and Chen, S. 1994: Terrain and Land Use for the Fifth-Generation Penn State/NCAR Mesoscale Modeling System (MM5): Program TERRAIN. NCAR Tech. Note NCAR/TN-397+IA, 24 pp.

Grell, G. A., 1993: Prognostic evaluation of assumptions used by cumulus parameterizations. *Mon. Wea. Rev.*, **121**, 764-787.

Grell, G. A., Dudhia, J., and Stauffer, D. R., 1994: A description of the fifth generation Penn State-NCAR Mesoscale Model (MM5), 138 pp, NCAR Tech. Note NCAR/TN-398+STR.

Gruning, S. E., and E., Batchvarova, 1990: Analytical model for the growth of the coastal internal boundary layer during on shore flow. *Quart. J. Roy. Meteor. Sci.*, **116**, 187-203.

Guangdong Provincial Bureau of Statistics, 2003: Guangdong Statistical Yearbook 2003, 588 pp, China Statistics Press.

Hanks, R. J., and G. L., Ashcroft, 1986: Applied Soil Physics. Springer-Verlag, 159 pp.

Harris, J. M., and J. D. W., Kahl, 1994: An analysis of 10-day isentropic flow patterns for Barrow, Alaska: 1985-1992. *J. Geophys. Res.*, **99**, 25845-25855.

Hinkelman, L. M., T. P., Ackerman, and R. T., Marchand, 1999: An evaluation of NCEP Eta model predictions of surface energy budget and cloud properties by comparison with measured ARM data, *J. Geophys. Res.*, **104**, 19535-19549.

HKEPD, 2003: Air quality in Hong Kong 2003. Annual Report, Environmental Protection Department, The Government of the Hong Kong Special Administrative Region, 45 pp. [Report available at: http://www.epd.gov.hk/epd/english/environmentinhk/air/air_quality/files/aqr03e.pdf]

HKEPD, 2004: Air Quality Statistics of Hong Kong, 2004. [Report available at: http://www.epd.gov.hk/epd/english/environmentinhk/air/data/aq_stat.html]

HKPD, 2003: Hong Kong 2030: Planning vision and strategy consultancy study to analyse broad land use pattern of the Pearl River Delta Region. [Available online at http://www.info.gov.hk/hk2030/hk2030content/wpapers/cover_wg.htm]

Hong, S. Y., and Pan, H. L., 1996: Non-local boundary layer vertical diffusion in a medium range forecast model. *Mon. Wea. Rev.*, **124**, 2322-2339.

Huang, J. P., Fung, J. C. H., Lau, A. K. H., and Qin, Y., 2005: Numerical simulation and process analysis of typhoon-related ozone episodes in Hong Kong. *J. Geophys. Res.*, **110**, D05301, doi:10.1029/2004JD004914.

Jacquemin, B., and J., Noilhan, 1990: Sensitivity study and validation of a land surface parameterization using the HAPEX-MOBILHY data set. *Bound.-Layer Meteor.*, **52**, 93-134.

Keen, C. S., and Lyons, W. A., 1978: Lake/land breeze circulations on the western shore of lake Michigan. *J. Appl. Meteor.*, **17**, 1843-1855.

Khemani, L. T., and Murty, B. V. R., 1973: Rainfall Variations in an Urban Industrial Region. *J. Appl. Meteor*, **12**, 187-194.

Klemp, J. B., and Durran, D. R., 1983: An upper boundary condition permitting internal gravity wave radiation in numerical mesoscale models. *Mon. Wea. Rev.*, **111**, 430-444.

Kok, G. L., Lind, J. A., and Fang, M., 1997: An airborne study of air quality around the Hong Kong territory. *J. Geophys. Res.*, **102**, 19043-19057.

Lam, J. S. L., A. K. H., Lau and J. C. H., Fung, 2006: Application of refined land-use categories for high resolution meso-scale atmospheric modelling. *Bound.-Layer Meteor.*, in press.

Lam, K. S, T. J., Wang, C. L., Wu and Y. S., Li, 2005: Study on an ozone episode in hot season in Hong Kong and transboundary air pollution over Pearl River Delta region of China. *Atmos. Environ.*, **39**, 1967-1977.

Lam, K. S., T. J., Wang, L. Y., Chan, T., Wang and J., Harris, 2001: Flow patterns influencing the seasonal behavior of surface ozone and carbon monoxide at a coastal site near Hong Kong. *Atmos. Environ.*, **35**, 3121-3135.

Lee, L. Y. L., R. C. W., Kwok, Y. P., Cheung, and K. N., Yu, 2004: Analyses of airborne 7Be concentrations in Hong Kong using back-trajectories. *Atmos. Environ.*, **38**, 7033-7040.

Lee, Y. C., and P. R. Hills, 2003: Cool season pollution episodes in Hong Kong, 1996-1002. *Atmos. Environ.*, **37**, 2927-2939.

Lee, Y. C., G. Calori, P., Hills, and G. R., Carmichael, 2002: Ozone episodes in urban Hong Kong 1994-1999. *Atmos. Environ.*, **36**, 1957-1968.

Leung, Y. K., and S. K., Ng, 1997: Regional temperature variations in winter of Hong Kong. Hong Kong Observatory Technical Note, No. 72.

Leung, Y. K., Yeung, K. H., Ginn, E. W. L., and Leung, W. M., 2004: Climate change in Hong Kong. Hong Kong Observatory Technical Note, No. 107.

Liu, H. P., and J. C. L., Chan, 2002: An investigation of air-pollutant patterns under sea-land breezes during a severe air-pollution episode in Hong Kong, *Atmos. Environ*, **36**, 591-601.

Liu, H. Y., W. L., Chang, S. J., Oltmans, L. Y., Chan, and J. M., Harr, 1999: On springtime high ozone events in the lower troposphere from Southeast Asian biomass burning. *Atmos. Environ.*, **33**, 2403-2410.

Liu, Y., F., Chen, T., Warner, and J., Basara, 2006: Verification of a mesoscale data-assimilation and forecasting system for the Oklahoma City area during the joint urban 2003 field project. *J. Appl. Meteor.*, in press.

Lo, J. C. F, A. K. H., Lau, F., Chen, and J. C. H., Fung, 2006a: Implication of rapid urban growth on the meteorological conditions in the Pearl River Delta region. *J. Appl. Meteor.*, in revision.

Lo, J. C. F, A. K. H., Lau, J. C. H., Fung, and F., Chen, 2006b: Role of land-sea-breeze circulations modified by urbanization on air pollution in Pearl River Delta region. *J. Geophys. Res.*, in revision.

Lo, J. C. F, A. K. H., Lau, Z. B., Yuan, F., Chen, and J. C. H., Fung, 2006c: A physical modeling approach for identification of source regions of air pollutants. *J. Geophys. Res.*, submitted.

Louie, P. K. K., J. G., Watson, J. C., Chow, A., Chen, D. W. M., Sin, and A. K. H., Lau, 2005: Seasonal characteristics and regional transport of PM2.5 in Hong Kong. *Atmos. Environ.*, **39**, 1695-1710.

Lu, R., and Turco, R. P., 1994: Air pollutant transport in a coastal environment. Part I: Two-dimensional simulations of sea-breeze and mountain effects. *J. Atmos. Sci.*, **51**, 2285-2308.

Mahrt, L., and H.-L., Pan, 1984: A two-layer model of soil hydrology. *Bound.-Layer Meteor.*, **29**, 1-20.

Mahrt, L., and M., Ek, 1984: The influence of atmospheric stability on potential evaporation. *J. Climate Appl. Meteor.*, **23**, 222-234.

Marshall, C. H., K. C., Crawford, K. E., Mitchell, and D. J., Stensrud, 2003: The impact of the land surface physics in the operational NCEP Eta model on simulating the diurnal cycle: Evaluation and testing using Oklahoma Mesonet data, *Wea. Forecasting*, **18**, 748-768.

Martilli, A., 2002: A two-dimensional numerical study of the impact of a city on atmospheric circulation and pollutant dispersion in a coastal environment. *Bound.-Layer Meteor.*, **108**, 91-119.

Mass, C. F., and Y. H., Kuo, 1998: Regional real-time numerical weather prediction: Current status and future potential. *Bull. Amer. Meteor. Soc.*, **79**, 253-263.

McCumber, M. C., and R. A., Pielke, 1981: Simulation of the effects of surface fluxes of heat and moisture in a mesoscale numerical model soil layer. *J. Geophys. Res.*, **86**, 9929-9938.

Mlawer, E. J., Taubman, S. J., Brown, P. D., Iacono, M. J., and Clough, S. A., 1997: Radiative transfer for inhomogeneous atmosphere: RRTM, a validated correlated-k model for the longwave. *J. Geophys. Res.*, **102**, 16663-16682.

Noilhan, J., and S., Planton, 1989: A simple parameterization of land surface processes for meteorological models. *Mon. Wea. Rev.*, **117**, 536-549.

Oltmans S. J., et al., 2004: Tropospheric ozone over the North Pacific from ozonesonde observations. *J. Geophys. Res.*, **109**, doi:10.1029/2003JD003466.

Pan, H.-L., and L., Mahrt, 1987: Interaction between soil hydrology and boundary-layer development. *Bound.-Layer Meteor.*, **38**, 185-202.

Pathak, R. K., X. H., Yao, A. K. H., Lau, and C. K., Chan, 2003: Acidity and concentrations of ionic species of PM2.5 in Hong Kong. *Atmos. Environ.*, **37**, 1113-1124.

Peters-Lidard, C. D., E., Blackburn, X., Liang, and E. F., Wood, 1998: The effect of soil thermal conductivity parameterization on surface energy fluxes and temperatures. *J. Atmos. Sci.*, **55**, 1209-1224.

Reynolds, R. W., Smith, T. M., 1994: Improved global sea surface temperature analyses. *J. Clim.*, **7**, 929-948.

Sawai T., 1978: Formation of the urban air mass and the associated local circulation. *J. Meteor. Soc. Japan*, **56**, 159-174.

Schaake, J. C., V. I., Koren, Q. Y., Duan, K., Mitchell, and F., Chen, 1996: A simple water balance model (SWB) for estimating runoff at different spatial and temporal scales. *J. Geophys. Res.*, **101**, 7461-7475.

Seinfeld, J. H., and Pandis, S. N., 1998: Atmospheric chemistry and physics: from air pollution to climate change, John Wiley and Sons, New York.

Singal, S. P., S. K., Aggarwal, and D. R., Pahwa, 1986: Studies of the marine boundary layer at Tarapur. *Bound.-Layer Meteor.*, **37**, 371-384.

Ueda H., Mitsumoto, S., and Kurita, H., 1988: Flow Mechanism for the Long-Range Transport of Air Pollutants by the Sea Breeze Causing Inland Night-time High Oxidants. *J. Appl. Meteor.*, **27**, 182-187.

Vaughan, J., Lamb, B., Frei, C., Wilson, R., Bowman, C., Kaminsky, C. F., Otterson, S., Boyer, M., Mass, C., Albright, M., Koenig, J., Collingwood, A., Gilroy, M., and

Maykut, N., 2004: A Numerical Daily Air Quality Forecast System for The Pacific Northwest. *Bull. Amer. Meteor. Soc.*, **85**, 549-561.

Venkatram, A., 1977: A model for internal boundary layer development. *Bound.-Layer Meteor.*, **11**, 419-437.

Viterbo, P., and A. C., Beljaars, 1995: An improved land surface parameterization scheme in the ECMWF model and its validation. *J. Climate*, **8**, 2716-2748

Vukovich, F. M., 1971: Theoretical analysis of the effect of mean wind and stability on a heat island circulation characteristic of an urban complex. *Mon. Wea. Rev.*, **99**, 919-926.

Wang, T., Vincent T. F., Cheung, K. S., Lam, G. L., Kok, and J. M., Harris, 2001: The characteristics of ozone and related compounds in the boundary layer of the South China coast: temporal and vertical variations during autumn season. *Atmos. Environ.*, **35**, 2735-2746.

Warner, T. T., D. F., Kibler, and R. L., Steinhart, 1991: Separate and coupled testing of meteorological and hydrological forecast models for the Susquehanna River Basin in Pennsylvania. *J. Appl. Meteor.*, **30**, 1521-1533.

Weil, A., and et al., 1988: A mesoscale shear convective cell observed during the C.O.A.S.T. experiment: Acoustic sounder measurement. *Bound.-Layer Meteor.*, **44**, 359-371.

Wong, M. S., and Kwan, W. K, 2002: Wind statistics in Hong Kong in relation to wind power, Hong Kong Observatory Technical Note, No. 77.

Woolum, C. A., 1964: Notes from a study of the microclimatology of the Washington, DC area for the winter and spring seasons. *Weatherwise*, **17**, 263-271.

World Meteorological Organization, 1984: Urban climatology and its applications with special regard to tropical areas. Proceedings of the technical conference organized by the WMO, Mexico, 26-30 November 1984 (WMO-No. 652): 534.

Wu, D., X., Tie, C., Li, A. K. H., Lau, J., Huang, X., Deng, and X., Bi, 2005: An extremely low visibility event over the Guangzhou region: A case study. *Atmos. Environ.*, **39**, 6568-6577.

Yuan, Z. B., A. K. H., Lau, H. Y., Zhang, J. Z., Yu, P. K. K., Louie, and J. C. H., Fung, 2006a: Identification and spatiotemporal variations of dominant PM_{10} sources over Hong Kong. *Atmos. Environ.*, in press.

Yuan, Z. B., J. Z., Yu, A. K. H., Lau, P. K. K., Louie, and J. C. H., Fung, 2006b: Application of positive matrix factorization in estimating aerosol secondary organic carbon in Hong Kong and its relationship with secondary sulfate. *Atmos. Chem. Phys.*, **6**, 25-34.

Yucel, I., W. J., Shuttleworth, J., Washburne, and F., Chen, 1998: Evaluating NCEP Eta model derived data against observations, *Mon. Wea. Rev.*, **126**, 1977-1991.

Zhang, D. L, Chang, H. R., Seaman, N. L., Warner, T. T., and Fritsch, J. M, 1986: A two-way interactive nesting procedure with variable terrain resolution. *Mon. Wea. Rev.*, **114**, 1330-1339.